Manipulating the Hydrogenated Amorpous Silicon Growing Surface

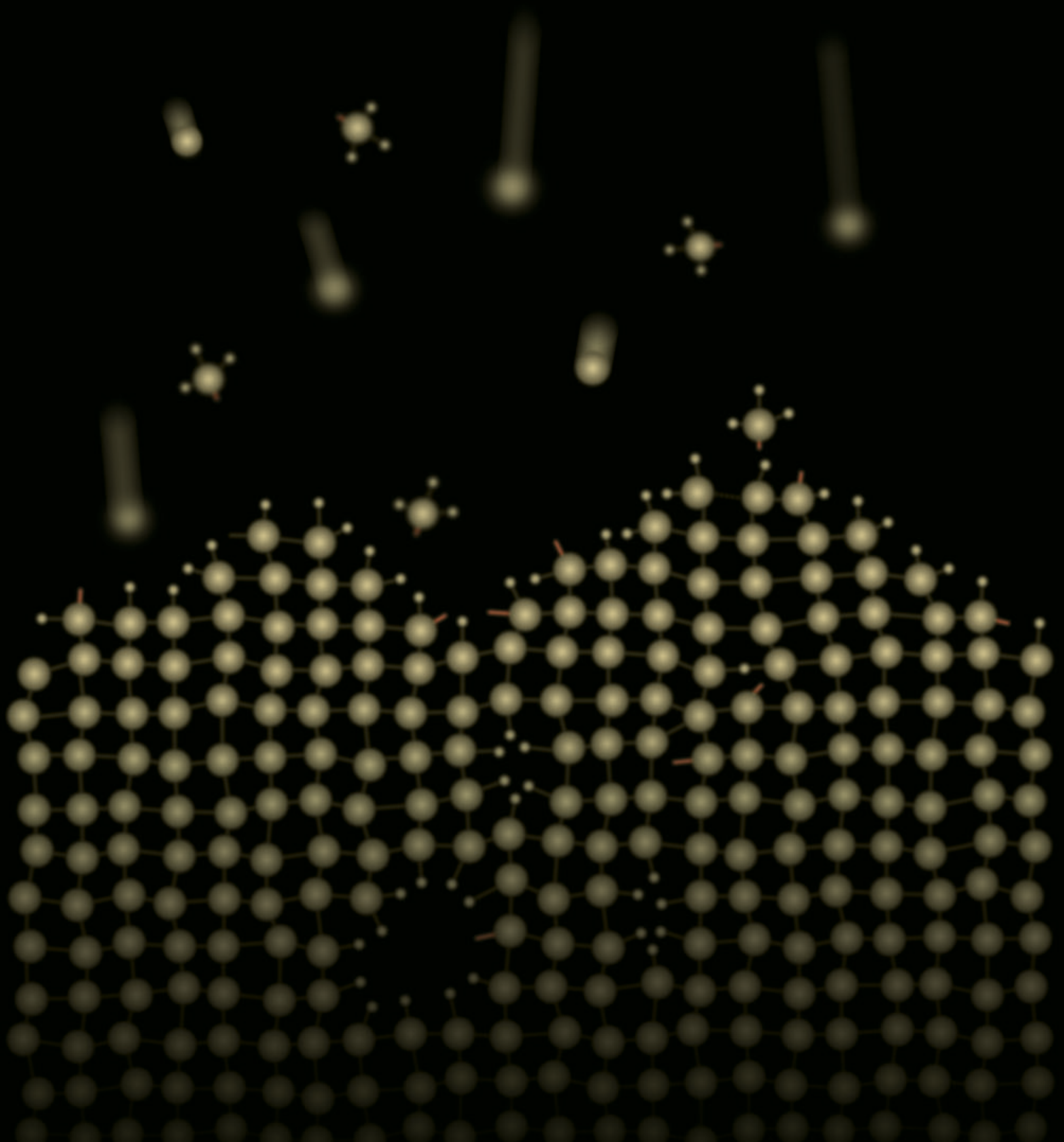

Michael A. Wank

Manipulating the Hydrogenated Amorphous Silicon Growing Surface

M. A. Wank

Manipulating the Hydrogenated Amorphous Silicon Growing Surface

Proefschrift

ter verkrijging van de graad van doctor
aan de Technische Universiteit Delft,
op gezag van de Rector Magnificus prof. ir. K.C.A.M. Luyben,
voorzitter van het College voor Promoties,
in het openbaar te verdedigen op
maandag 14 maart 2011 om 10:00 uur

door

Michael Alexander WANK

Master of Science, Chalmers University of Technology
geboren te Frankfurt/Main, Duitsland

Dit proefschrift is goedgekeurd door de promotoren:
Prof. dr. ir. M. Zeman
Prof. dr. ir. M.C.M. van de Sanden

Copromotor:
Dr. R.A.C.M.M. van Swaaij

Samenstelling promotiecommissie:

Rector Magnificus	voorzitter
Prof. dr. ir. M. Zeman	Technische Universiteit Delft, promotor
Prof. dr. ir. M.C.M. van de Sanden	Technische Universiteit Eindhoven, promotor
Dr. R.A.C.M.M. van Swaaij	Technische Universiteit Delft, copromotor
Prof. dr. P.M. Sarro	Technische Universiteit Delft
Prof. dr. W. J. Goedheer,	FOM Institute for Plasma Physics Rijnhuizen
Prof. dr. P. Roca I Cabarrocas	École Polytechnique
Dr. E. A.G. Hamers	Nuon Helianthos
Prof. ir. L. van der Sluis,	Technische Universiteit Delft, reservelid

The project was financially supported by the Ministry of Economic Affairs, Agriculture and Innovation, within the framework of the EOS-LT program of NL Agency.

M.A. Wank
Manipulating the Hydrogenated Amorphous Silicon Growing Surface
Ph.D. thesis, Delft University of Technology, with summary in Dutch, 2011

Published and distributed by CPI, Wöhrmann PrintService, Zutphen, the Netherlands

ISBN: 978-90-8570-725-7

Copyright © 2011 M.A. Wank.

All rights reserved.
No part of this publication may be reproduced, stored in a retrieval system, or transmitted in any form or by any means without the prior written permission of the copyright owner.

Contents

Contents **2**

1 Introduction **1**
1.1 Renewable Energy & the Photovoltaic Industry 1
1.2 Thin Film Solar Cells 6
1.3 Hydrogenated Amorphous Silicon 8
1.4 Aim of this work 13

2 Experimental **17**
2.1 Deposition of a-Si:H with Expanding Thermal Plasma Chemical Vapour Deposition (ETP-CVD) 17
2.1.1 Experimental Deposition Setup CASCADE 17
2.1.2 Substrate Biasing Techniques 20
2.2 Thin Film Characterization 27
2.2.1 Real-Time Spectroscopic Ellipsometry (RTSE) 27
2.2.2 Fourier Transform Infrared Absorption Spectroscopy (FTIR) 33
2.2.3 Reflection-Transmission (RT) Spectroscopy 35
2.2.4 Dual Beam Photoconductivity (DBP) and Fourier Transform Photocurrent Spectroscopy (FTPS) 36
2.2.5 Dark Conductivity and Activation Energy 39
2.2.6 Photoconductivity 40
2.2.7 Atomic Force Microscopy (AFM) 40
2.3 Solar Cell Characterization 40
2.3.1 Current-Voltage Characterization 40
2.3.2 Quantum Efficiency 41

3 RF Biasing of ETP-CVD a-Si:H 45
3.1 Effect of RF Biasing on a-Si:H Thin Films Deposited at Different Reactor Pressures . . . 45
3.1.1 Introduction . . . 45
3.1.2 Experimental Details . . . 46
3.1.3 Results&Discussion . . . 47
3.1.4 Conclusions . . . 51

4 Pulse-Shaped Biasing as a New Tool to Control the Ion Energy Distribution Function in a-Si:H Film Growth in ETP-CVD 53
4.1 Introduction . . . 53
4.2 Analysis of Pulse-Shaped Biasing as a Tool to Control the Ion Energy Distribution . . . 55
4.2.1 Experimental Details . . . 55
4.2.2 Results & Discussion . . . 58
4.3 Effect of Ion Bombardment with a Narrow Ion Energy Distribution on a-Si:H Film Growth and Material Properties . . . 64
4.3.1 Experimental Details . . . 64
4.3.2 Results & Discussion . . . 65
4.4 Conclusions . . . 73

5 Implementation of Intrinsic a-Si:H Layers Deposited with Pulse-Shaped Biasing in p-i-n Solar Cells 75
5.1 Introduction . . . 75
5.2 Experimental Details . . . 77
5.3 Results & Discussion . . . 81
5.3.1 Intrinsic a-Si:H Analysis . . . 82
5.3.2 Solar Cell Analysis . . . 88
5.4 Conclusions . . . 93

6 On the Surface Roughness Evolution of a-Si:H films 95
6.1 Influence of RF Substrate Biasing on the Surface Roughness Evolution . . . 95
6.1.1 Introduction . . . 95
6.1.2 Experimental Details . . . 96
6.1.3 Results . . . 97
6.1.4 Conclusions . . . 101
6.2 Influence of Hydrogen Dilution on the Surface Roughness Evolution . . . 101
6.2.1 Introduction . . . 101
6.2.2 Experimental Details . . . 102
6.2.3 Results & Discussion . . . 103

6.2.4 Conclusions 114

7 General Conclusions **117**

Bibliography **129**

Summary **131**

Samenvatting **135**

Publications **139**

Acknowledgements **141**

About the Author **143**

Chapter 1

Introduction

1.1 Renewable Energy & the Photovoltaic Industry

Modern lifestyle in first world countries is currently fueled by two billion years of accumulated energy reserves. Estimations of the world power consumption and shares of power technologies are subject to speculation and uncertainty, but here they only serve as a guide to illustrate the big picture. In 2007 the world energy consumption was around 145 million GWh, with about 18 million GWh of electricity consumption [1,2]. The dominant energy source is fossil fuel with $\sim$90%, which is the result of anaerobic decomposition of organic material, usually under high pressure and temperature, and comes in the shape of gas ($\sim$25%), oil ($\sim$ 35%) or coal ($\sim$30%) [1,3].

In recent years, there has been a strong rise in not only research interest but more importantly implementation of renewable energy sources in the European Union (EU). In 2008, of the 24 GW new power capacity installed in the EU, a 57 % share is from renewable energy sources (wind power $\sim$35%, photovoltaics $\sim$19%, hydro $\sim$2%, biomass $\sim$0.7%), making it for the first time the dominant contributor to new power installations [4]. This increasing market implementation of renewable energy sources is a direct result of new policies that have been implemented across the EU, with the aim to increase the contribution of renewable energy sources. Many countries now actively promote the implementation of renewable energy sources into their energy markets through renewable energy promotion policies. These policies can affect (i) price or quantity, (ii) investment cost, or (iii) come as public investments and market facilitation activities, or a combination of these three activities. The EU has adopted renewable energy targets, aiming at $\sim$20% of total electricity generation from renewables by 2020 [5].

There are several motivations for these new energy policies:

- Global Warming
- Limited Fossil Resources
- Energy Security & Independence
- Business and Technology Development

Global Warming: Since the onset of the industrial revolution in 1750 the concentration of greenhouse gases, especially carbon dioxide (CO_2), methane (CH_4) and nitrous oxide (N_2O, has increased markedly as a result of human activities. Of these three greenhouse gases related to human activity, CO_2, is the most important one and results from burning fossil fuel, while the other two are primarily products from agricultural processes. In is stated clearly in the 2007 report of the United NationsŠ Intergovernmental Panel on Climate Change (IPCC) that due to improved understanding of anthropogenic warming and cooling influences on the climate in recent years, there is now a very high confidence that "the global average net effect of human activities since 1750 has been one of warming with a radiative forcing of +1.6 W/m^2" [6]. Radiative forcing is a mearsure for the influence of atmospheric alterations on the balance of incoming and outgoing energy in the earth atmosphere system. The positive value of +1.6 W/m^2 means that more radiative energy is absorbed by the atmosphere than is emitted into space compared to preindustrial conditions defined at 1750 in the IPCC report [6], resulting in an increase of the average global temperature. This warming of the globe is not a distant possibility, but currently happening as evident from observations of increasing average and ocean temperatures, widespread melting of snow and ice and rising global average sea levels, summarized in Fig. 1.1. As a result numerous long-term changes in climate at continental and regional scales have been reported [6]. Significantly increased precipitation in eastern parts of North and South America, northern Europe and Asia as well as drying in the Sahel, the Mediteranean, southern Afrika and southern Asia have been observed. Also changes in extreme weather phenomena like heavy precipitation, heat waves and intense tropical cyclones have been reported. For the next two decades an increase in average global temperature by 0.2°C per decade is projected [6]. Climate change is expected to continue even if green house gas concentration in the atmosphere could be kept at the levels of the year 2000, due to the slow feedback of the climate system. A reduction especially of CO_2 concentration in the atmosphere is necessary in order to limit the changes in climate to a minimum. Renewable energy sources like wind power and photovoltaics do not directly emit greenhouse gases during operation and can thus make an important contribution to this necessary shift in power production.

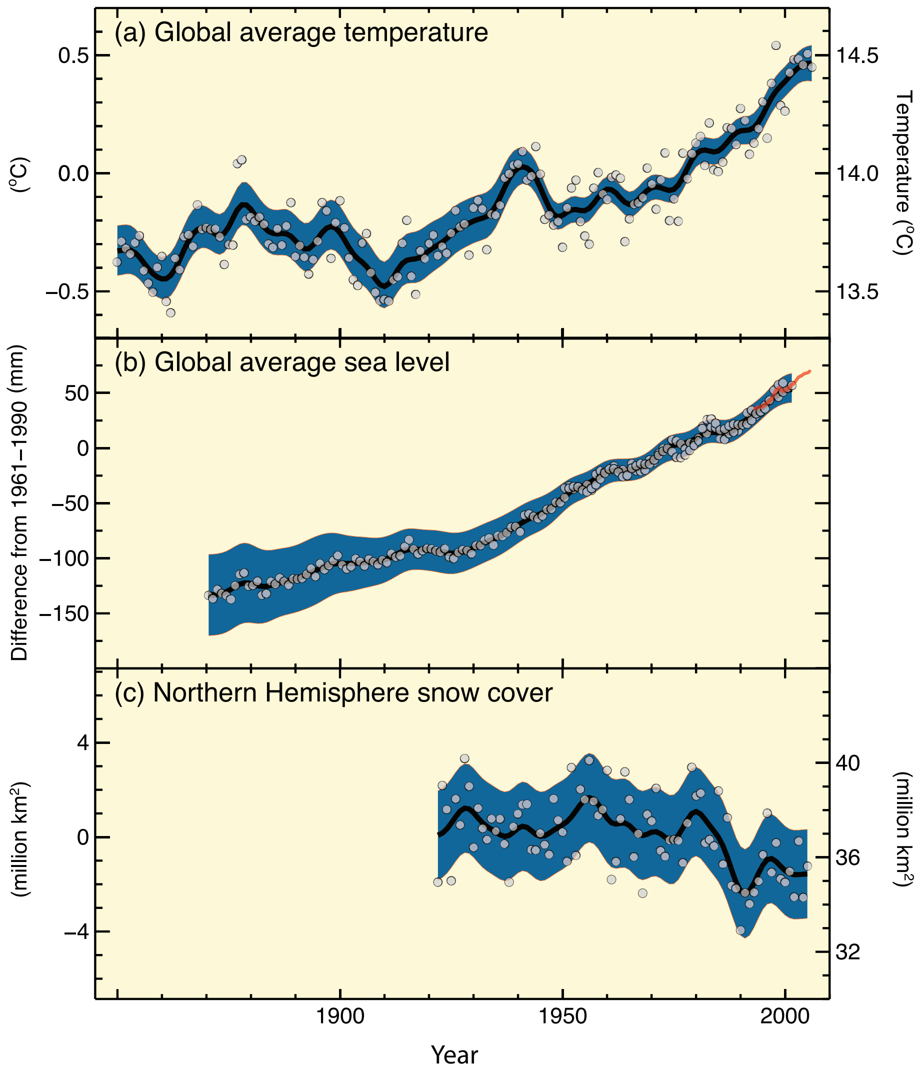

Figure 1.1 Observed changes in (a) global average surface temperature, (b) global average sea level and (c) snow cover in the northern Hemisphere between March-April. All data are shown relative to averages for the period 1961 Ű- 1990 [6].

Limited Fossil Resources: Although there are still vast amounts of fossil fuel available, they are still *limited*. At some point fossil fuel will inevitably run out, despite continuous efforts to discover more reservoirs of oil, coal and gas. Additionally, long before these resources will run out, it will become increasingly more difficult to extract these resources, which will inevitably increase

their cost. How long it will take until this increase in price will be noticeable can currently not be predicted. However, keeping in mind that the currently proven reserves for oil and gas will be depleted within a matter of decades and coal about 1-2 century (e. g. [7], the time frame is set in which an increase in mining cost and ultimately also in cost of derived forms of energy will occur. Renewable energy sources on the other hand are a sustainable form of energy supply since they rely on the energy provided by solar radiation reaching the earth. Additionally, renewable energy sources are currently the only technology with a continuous *decrease* in cost per kWh for the consumer.

Energy Security & Independence: Currently the EU imports 50% if its required energy resources and this dependency is expected to increase further to 70% by 2030 [8]. The dependence on external supplies makes the European power supply very vulnerable to disruptions in the energy resource supply chain [5, 8, 9]. Additional strain is provided by the increasing demand in the same limited energy resources by emerging economies in the developing world and therefore increasingly high and fluctuating energy prices are expected. As described above, the independence of renewable energy from a resource that is concentrated in just a few countries worldwide is an important benefit of renewable energy technologies, which would enable to become independent from external suppliers outside of the EU. Additionally, renewable power systems are usually very distributed systems and not as localized as classical power plants based on fossil fuel or radiactive material. This makes the European power supply less sensitive to attacks on a fundamental part of the infrastructure.

Business and Technology Development: The competitiveness of the European economy strongly depends on cheap electricity [5,9]. In order to guarantee low electricity prices in the future, research and development of advanced, renewable power generation technology is regarded necessary. Promoting local industry in this field will also maintain and enhance the role of Europe as a global leader in advanced power generation technology and can help to establish the future "big players" of this industry at least partly in the EU.

There are essentially three sources of renewable energy: solar radiation, the gravitational force between earth and moon and geothermal heat. Solar radiation is the most important source, its energy can be collected either directly through solar panels, or indirectly through "byproducts" of solar radiation, like wind or biomass. The gravitational force between earth and moon leads to the tides on the oceans, from which energy can be extracted in the form of tidal energy. Geothermal heat is the result of both residual heat from the earth's creation as well as radioactive decay of isotopes like U_{235}, U_{238} or K_{40}. Geothermal heat can be extracted directly in the form of heat and be either used directly as heat source or indirectly by transforming heat into electricity.

In the remainder of this thesis we will focus on the conversion of solar

radiation directly into electricity through photovoltaics. In photovoltaics, direct current (DC) electrical power is generated from solar cells when illuminated with electromagnetic radiation from the sun. The effect of European energy policies on the growth of the European photovoltaic industry is discussed in detail annually in the status report of the Institute for Energy of the EU [10]. In 2008 the cumulative installed photovoltaic system capacity in Europe has doubled to 9.5 GW. This is three times more than what was expected for 2010. Due to this rapid PV grid implementation, a new target was defined which now aims at 12% PV generated electricity by 2020. At these expected quantities in PV generated electricity, the new challenge becomes the implementation of this electricity into the grid. Not only implementation but also production capacities have increased significantly in recent years. In 2008 the production capacity in Europe was 1.9 GW, a 7% increase compared to 2007, surpassed only by China at 2.4 GW, which has seen an even more impressive PV growth in recent years. If the currently planned worldwide production capacities are implemented as planned, $>$ 60 GW annualy will be available in 2015. However, it is important to keep in mind that the capacity utilisation rate, i. e. the percentage of production capacity that is actually used, is currently only about 54%.

The dominant solar-cell technology today with about 90% market share is based on crystalline silicon (c-Si). Crystalline silicon cells, first demonstrated in 1954, benefited from the thorough research carried out on crystalline silicon from the 1960's to understand fundamental physical properties of this material with the aim to develop and improve integrated circuits. This also lead to development of technology for high quality crystalline silicon fabrication for the electronics and high-tech industry. Both the development of c-Si fabrication facilities and a thorough fundamental understanding of the material helped to start up the crystalline silicon solar cell development. The abundance of Si in the form of SiO_2 in the earth's crust is another important factor. While the fabrication of c-Si solar cells is quite costly, the obtained modules have so far the highest efficiencies on the market with $\sim 17 – 22\%$ [11].

One important milestone of PV module manufacturers is to reach grid parity for solar electricity. Grid parity means that electricity generated from a solar cell has the same cost/kWh as conventional electricity from the grid. To this end, factors like module life-time, power conversion efficiency and fabrication costs are crucial and thus subject of continuous research. Depending on the development in the near future, grid parity of PV generated electricity in central Europe could be achieved between 2013-2030 according to different projections [12, 13], e. g. by 2020 in most of Europe if the goals of the European Photovoltaic Industry Association are realized [10]. Already now, in many countries PV generated electricity can be cheaper than peak prices in the electricity exchange market [10].

1.2 Thin Film Solar Cells

Despite the current dominance of crystalline silicon solar cells on the market, they are not expected to reach the ultimate goal of the photovoltaic industry, namely to reach grid parity, currently between 0.10 - 0.25 €/kWh depending on the domestic market. The high cost of crystalline silicon fabrication and its slow fabrication are in conflict with the need for relatively thick solar cells required to absorb most sunlight in c-Si cells. Thick cells not only mean more material consumption but also the need for a high material quality with low defect concentrations to enable charge carriers to be collected at the contacts before they can recombine.

Thin film solar cells have the potential to deliver electricity at grid parity due to their need for less thick films as well as cheaper fabrication of modules compared to crystalline silicon modules [11]. Thin film modules are expected to reach significant industrial production volumes in the near future - of the 60 GW total production capacity planned for 2015, more than one third will be thin film solar cells. Although there are many thin film solar cell technologies discussed in literature, currently only three technologies have been developed to a commercially interesting level:

- Cadmium Telluride (CdTe) cells
- Copper-Indium-Gallium-Selenide (CIGS) cells
- Silicon-based cells

CdTe cells offer power conversion efficiencies around 16% on laboratory scale. Problematic, however, is the very limited supply of tellurium, which makes mass production difficult. There are also environmental issues concerning the cadmium in the cells, which is a toxic material and thus reliable recycling schemes must be developed before CdTe can be commercialized in significant numbers.

Polycrystalline **CIGS** cells with promising efficiencies around 20% have been demonstrated and with 13 - 16% efficiency they belong to the thin film technologies which have offered the highest efficiencies on module scale. Problems with CIGS cells are the deposition of the stochiometrically complex material under industrial conditions, the cadmium-containing CdS layer, which is still required as junction layer and the low availability of indium.

Silicon-based technologies are expected to be dominant thin film solar cell type in terms of production capacity [10], as can be seen in Fig. 1.2. They can be split into two categories, amorphous and crystalline silicon solar cells, with the amorphous cells being the better developed and implemented technology. The efficiency for amorphous cells is lower compared to other thin film

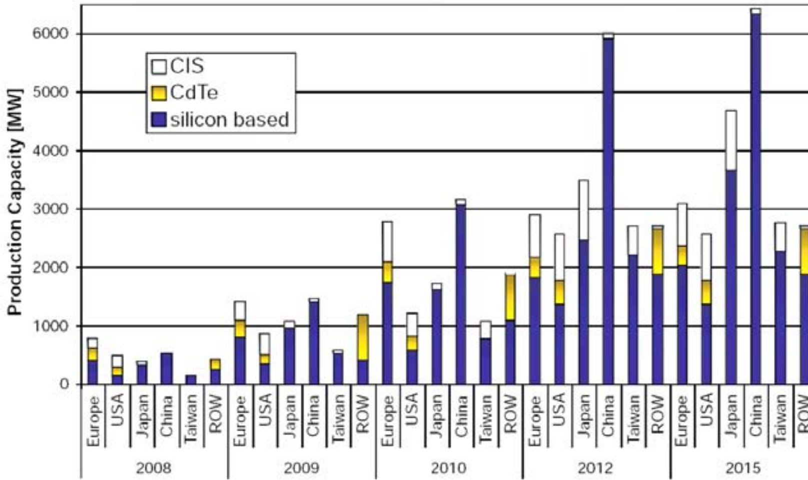

Figure 1.2 Overview of current and future thin film production capacities by geographical region [10].

technologies and modules have efficiencies around $7-8\%$ [11]. Additionaly, solar cell efficiencies degrade under illumination, the so-called Staebler-Wronski effect. Despite these drawbacks, the reasons for the success of amorphous silicon-based solar cells can be found in its processing: amorphous silicon is commonly deposited by plasma-enhanced chemical vapour deposition, which allows deposition of homogeneous films on relatively large substrates and at substrate temperatures below 200°C. This is the lowest deposition temperature of all above mentioned thin film technologies and enables deposition on flexible substrates like stainless steel or plastic foil, allowing low-cost roll-to-roll processing. Amorphous silicon has a higher absorption coefficient compared to crystalline silicon over a wide range of the visible spectrum, reducing the film thickness required to absorb most of the visible light down to $\sim$ 300 nm for amorphous silicon cells. Development of amorphous silicon thin film production technology also benefited from increasing interest in this material for other potential applications in transistors or flat-panel displays [14]. All these factors as well as the abundance of silicon in the earth's crust make amorphous silicon the potentially cheapest of the above mentioned thin film solar cell technologies. For the rest of this thesis we will focus on amorphous silicon solar cells.

1.3 Hydrogenated Amorphous Silicon

It was discovered early on that pure amorphous silicon has a very high defect concentration $\sim 10^{19}$ cm^{-3}, which reduces the electronic conductivity dramatically [11]. Due to the disorder in the amorphous silicon, many unsaturated danging bonds remain in the material, energetically located in the band gap of the material and thus acting as defect states. However, amorphous silicon prepared from *silane gas* (SiH_4) using a glow discharge shows good electronic conductivity [15]. In this case, most of the dangling bonds are passivated by hydrogen atoms and the defect density significantly reduces to $\sim 10^{15}$ cm^{-3}. This hydrogenated amorphous silicon (a-Si:H) is the base material for all amorphous silicon based solar cells.

As mentioned above, a-Si:H has a much higher absorption coefficient over a wide range of the solar spectrum. This is related to the direct band gap as a result of absence of long-range order in a-Si:H. This lack of long range order means that selection rules for the indirect band gap of crystalline silicon do not apply.

The atomic arrangement and the microstructure of hydrogenated amorphous silicon is schematically shown in Fig. 1.3. The atomic structure of amorphous silicon is characterized by the same local order as crystalline silicon and each Si atom bonded to on average four neighbouring Si atoms. But the material is lacking the long-range order that is present in crystalline materials that allows to know the presence of all atoms in the material once one unit cell in the material is defined (assuming defect-free material). The amorphous distribution of atoms also means that the distance between the atoms and therefore the bond lengths vary. Si-Si bonds can be stretched or compressed, or the angle between Si atoms can be affected by the amorphous matrix. Both angular variation and bond length variation affect the electronic structure and give rise to tail states of the conduction and valence band, as will also be discussed in the experimental section in more detail. Not all Si atoms are able to bond to four neighboring Si atoms, which can result in the formation of either unsaturated dangling bonds or Si-H bonds if a H atom saturated the dangling bond, as shown schematically in Fig. 1.3. As will be discussed in the experimental section, in this work we assume that hydrogen in a-Si:H is predominantly present in the form of mono- or dihydrides, located in either vacancies or in clustered form in nanovoids, as can also be seen in Fig. 1.3.

As a result of the structurally relaxed amorphous arrangement of Si atoms also the electronic structure a-Si:H is different from c-Si. In c-Si the periodic arrangement of Si atoms leads to sharply defined valence and conduction band edges as can be seen in Fig. 1.4(a). The gap between these two edges is defined as the band gap. In a-Si:H the amorphous arrangement of Si atoms leads to continuous distribution of electronic states with tail states and defect states

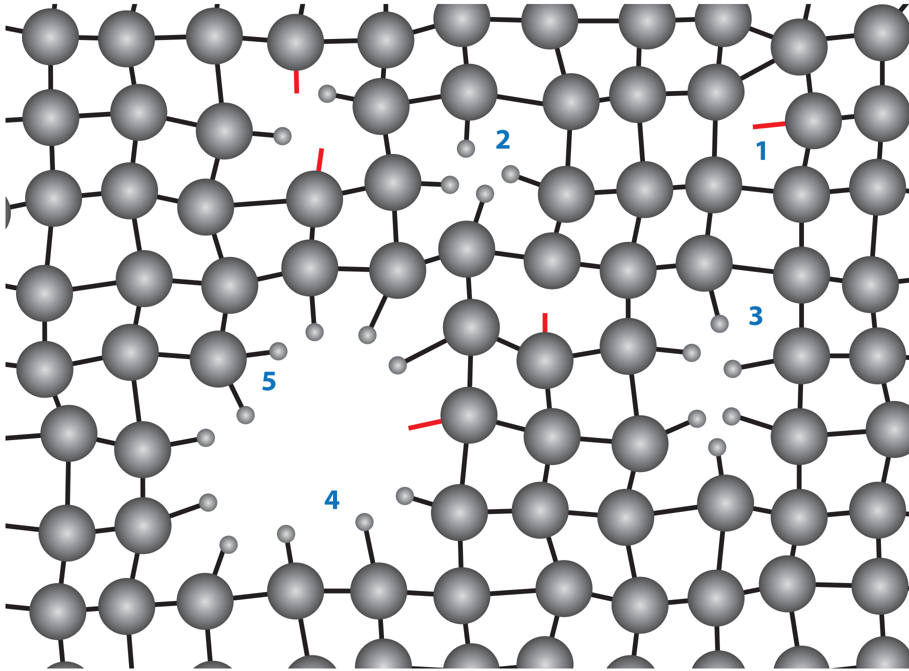

Figure 1.3 Schematic drawing of the atomic structure and microstructure of hydrogenated amorphous silicon. Indicated in figure are (1) dangling bond (in red), (2) monovacancy with monohidrides (-Si_3-SiH) (3) divacancy, (4) nanovoid and (5) dihydride (-Si_2-SiH_2).

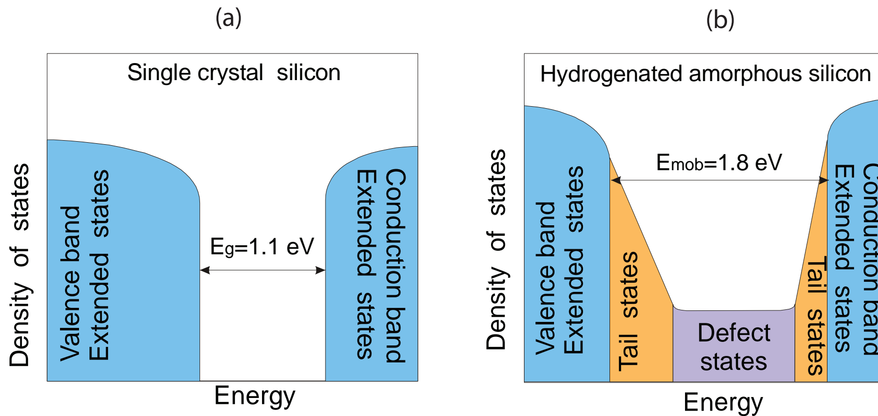

Figure 1.4 Schematic densities of states for (a) crystalline silicon and (b) hydrogenated amorphous silicon

located energetically in between the extended band states, as can be seen in Fig. 1.4(b). The mobility gap is indicated in the figure, which represents the energy gap which must be overcome by electrons to get from one delocalized extended state in the valence band to another delocalized state in the conduction band. Electronic states in the band tails are considered to be localized states.

The Staebler-Wronski effect [16] mentioned above, reduction of the photoconductivity and dark conductivity in a-Si:H films under prolonged illumination, is suspected to be related to the presence of hydrogen in the film. It is assumed that metastable defects are formed under illumination, and charge carrier recombination as well as hydrogen are expected to play a role in this process, but the exact nature of the mechanism is still unknown.

Due to extensive interest in a-Si:H thin film research over many years, a large number of deposition techniques have been utilized to deposit a-Si:H thin films. The most widespread technology is parallel-plate radio frequency plasma enhanced chemical vapor deposition (RF-PECVD), which dominates both research and commercial production. There are however numerous other deposition techniques available today, like very high-frequency (VHF) PECVD, hot-wire CVD (HW-CVD), Electron Cyclotron Resonance CVD (ECR-CVD) or the expanding thermal plasma CVD (ETP-CVD) which was used in this work.

Whichever deposition method is used to grow the film, it is commonly accepted that in order to obtain material suitable for solar cell application the growth flux should be dominated by silyl radicals (SiH_3) [11]. However, even after decades of research on a-Si:H thin film growth the exact growth mechanism is still not entirely understood due to the very complex surface chemistry during deposition involving a number of surface processes.

An early model to describe a-Si:H film growth by Winer [17] and Street [18, 19] is based on a thermodynamic approach. In this model hydrogen configuration and defect formation is explained in terms of substrate temperature and growth rate. Although this model can successfully explain experimental observations of bulk film properties, it does not go into the details of the actual surface processes leading to film growth.

Surface processes play an important role in the kinetic growth model developed by Gallagher [20], Matsuda [21, 22] and Perrin [23]. This model assumes SiH_3 to be the dominant growth precursor and suggests possible surface reactions. Main assumption is that SiH_3 radicals can be physisorbed on the surface and in this weakly bound state are able to diffuse along the substrate surface. The physisorbed SiH_3 can either abstract a H atom from the surface and leave the surface as SiH_4, leaving a dangling bond on the surface, or form a covalent bond with a preexistent dangling bond on the surface and be incorporated into the film. The chance for incorporation in the film is macroscopically described by the reaction probability β and is typically observed to be

temperature-independent for $SiH_3 \sim 0.3$.β is composed of two components, the probability that SiH_3 is sticking on the substrate surface (s) and the probability that it recombines on the surface to form e g. SiH_4 or Si_2H_6 (γ). Experimentally only $\beta = s + \gamma$ can be determined experimentally. In the kinetic growth model surface temperature provides the activation energy for physisorbed surface diffusion of SiH_3 on the surface. At substrate temperatures $> 400°C$ thermal hydrogen desorption is possible resulting in the formation of an H_2 molecule and two dangling bonds, but at substrate temperatures typical for a-Si:H deposition ($\sim 200°C$) two SiH_3 radicals are necessary per incorporated Si atom. The surface diffusion of SiH_3 can account for very smooth surfaces typically obtained in a-Si:H films, with an average height difference between surface valleys and surface hills of as little as 20 Å. Also reactions of atomic hydrogen with the surface has been included, which are assumed to have a significant effect on film growth only at high hydrogen dilution at the transition to microcrystalline silicon (μc-Si) film growth.

In-situ surface dangling bond density measurements have shown that the dangling bond density is relatively low and not strongly correlated to substrate temperature $< 200°C$, in contrast to the bulk defect density [24–26]. This suggests that the surface dangling bond density and defect density are not directly related and that defects instead are created from weak bonds in a so-called defect-pool process. A new perspective was provided by Von Keudell et al. [27], who suggested surface hydrogen is not abstracted by SiH_3 to form dangling bonds. Instead they suggest that SiH_3 directly inserts into strained Si-Si bonds on the surface and thus dangling bonds are not the only insertion point for SiH_3 radicals [27]. This is in agreement with the relatively low dangling bond concentration mentioned above. Insertion into strained bonds would require either a preferred formation of strained bonds in surface valleys or surface diffusion of chemisorbed SiH_x groups to explain the typically very smooth a-Si:H surfaces.

Any suggested growth mechanisms must account for the very smooth surfaces of a-Si:H. Both the distribution of growth sites, dangling bonds or strained Si-Si bonds, as well as the mobility of the growth precursor play an important role. First of all, a mobile precursor is required. Most commonly surface diffusion of SiH_3 is assumed to result in smooth surfaces, but a mobile SiH_3 radical is not sufficient to explain the very smooth a-Si:H surfaces if growth sites are randomly distributed over the substrate surface and absorbed silyl radicals are rendered immobile. Therefore the diffusion of dangling bonds or whole Si-H surface groups is worth considering. Dangling bond diffusion could explain how smooth films are obtained under conditions where dangling bond creation is dominant and randomly distributed on the surface, by diffusion of dangling bonds preferably into surface valleys. Both dangling bond or even chemisorbed SiH_3 diffusion would be compatible with the high activation

energy for diffusion of ~ 1 eV obtained by Smets et al. [28].

Ceriotti et al. [29] utilized ab-initio calculations to investigate surface diffusion of SiH_3 radicals on fully hydrogenated H:Si (100) surfaces and obtained maximum diffusion lengths in the order of only a few lattice spacings in the range of 300-1000K for a fully hydrogenated surface, due to quick desorption of physisorbed SiH_3 radicals. Other mass transport mechanisms like the re-emission mechanism might explain transport of SiH_3 radicals on the substrate surface over distances larger than the short diffusion length of SiH_3 radicals. Re-emission is a non-local, temperature-independent mass transport mechanisms that can explain smoothening on large length scales. It was suggested by Cale et al. [30] for trench-filling depositions, and further elaborated on by Cheng et al. [31] and Singh et al. [32]. In the re-emission model a particle with a sticking coefficient < 1 can be re-emitted from surface features upon impact and transported deeper into the surface valley, thus transporting mass into surface valleys.

Another mechanism that could be responsible for the hydrogen abstraction by SiH_3 from the surface is via an Elay-Rideal mechanism [33]. In this mechanism the SiH_3 radical does not physisorb to the surface but instead the hydrogen abstraction happens with the SiH_3 radical remaining in the gas phase . This abstraction is a fast process and surface hydrogen abstraction happens instantaneous, such that the created dangling bonds are still distributed randomly across the surface. Due to the random distribution of created dangling bonds across the surface it still requires additional mechanisms like dangling bond diffusion or chemisorbed -SiH_x diffusion to explain the smooth a-Si:H surfaces.

In plasma-based deposition techniques, also ion bombardment can be present and ion-surface interactions need to be considered. At very low ion energies only local thermal spikes provide the surface with energy. With increasing ion energy first surface atom and then bulk atom displacement become increasingly important, with respective threshold energies around 18 eV and 40 eV for these two mechanisms [34]. At even higher ion energies sputtering also becomes important, the exact energy depends on the relative mass of the surface atoms and the bombarding ion [35].

As is evident from the discussion above, so far no clear picture has emerged that can explain growth of a-Si:H thin films under all conditions, due to the number of complex surface processes involved. Despite all research effort put into this topic, obtaining a-Si:H thin films with the right property for solar cells still strongly relies on empirical processing experience rather than fundamental understanding of the growth mechanism.

1.4 Aim of this work

The deposition setup used for most experiments reported in this thesis is the above mentioned expanding thermal plasma chemical vapor deposition (ETP-CVD). The technique will be described in detail in the experimental section. Main benefit of ETP-CVD are the high growth rates that can be achieved, with ~ 1 nm/s for depositions carried out in this work, but up to ~ 10 nm/s has been achieved in the past [36]. These high growth rates are especially beneficial for growth of the intrinsic layer, which is the thickest layer in a p-i-n solar cells. For a-Si:H of 300 nm film thickness it will take an rf-PECVD reactor about 25 minutes at 0.2 nm/s to grow the film, whereas with ETP-CVD at 1 nm/s it only takes ~ 5 minutes. If this difference in growth rate can be upscaled to industrial production it would result in a higher throughput of the deposition setup, leading ultimately to a drop in €/kWh for the generated electricity, with the aim to approach grid parity.

Amorphous silicon based solar cells were demonstrated for the first time as p-i-n devices in 1976 by Carlson and Wronski [37]. These p-i-n devices are still the standard device structure for single junction amorphous silicon cells today. A p-i-n cell consists of a thin p-doped layer $\sim 10-15$ nm thick, an undoped, intrinsic amorphous silicon layer of ~ 300 nm thickness, also called absorber layer, and a thin n-doped layer, again ~ 20 nm thick. A drawing of such a p-i-n structure can also be seen in Fig. 1.5(a) schematically and in Fig. 1.5(b) with the layer thickness to scale. The doped layers need to remain as thin as possible due to the high defect concentration in doped amorphous silicon, which leads to charge carrier recombination in these layers. The cell is typically deposited in the sequence given above on glass substrates coated with a transparent conductive oxide (TCO) material with low absorption coefficients in the range of the solar spectrum.

In the p- and n-doped layers we have high concentrations of excess holes and electrons, respectively. These excess concentrations of charge carriers lead to their diffusion into the intrinsic layer where they recombine. The immobile dopant atoms are left behind in the doped layers, with the donor atoms having a net positive charge and the acceptor atoms having a net negative charge. As a result of these immobile charges a built-in electric field is formed across the intrinsic layer, typically around 10^4 V/cm. Under illumination, photons enter the solar cell through the p-layer, which acts as a nearly transparent window layer, and are absorbed predominantly in the intrinsic absorber layer, resulting in the formation of electron-hole pairs. Due to the built-in electric field, these charge carriers are now separated and drift across the intrinsic layer towards the doped contact layers where they are collected, resulting in an electric DC current.

In order to deposit dense a-Si:H films with the right properties for solar-

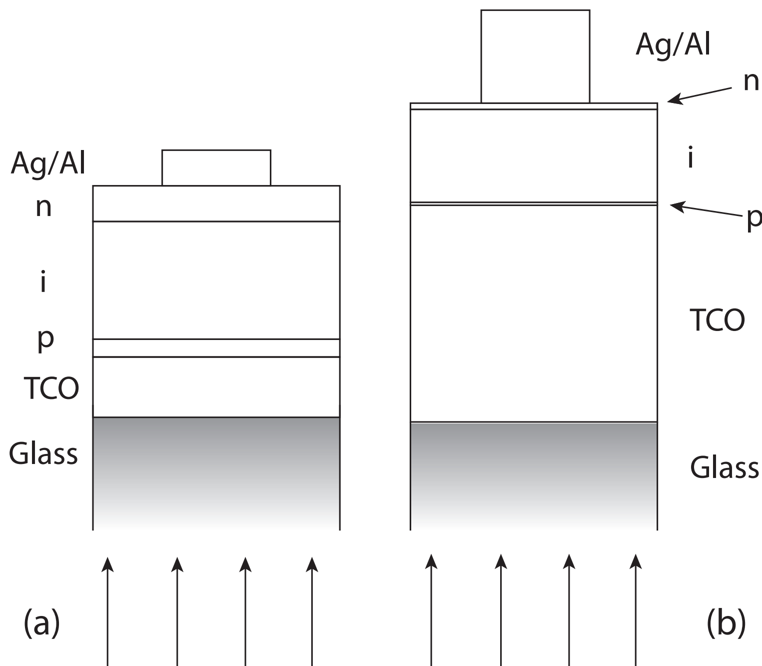

Figure 1.5 (a) Schematic drawing of an amorphous silicon p-i-n solar cell, (b) the same p-i-n solar cell drawn with the layer thickness to scale.

cell application with ETP-CVD at growth rates > 1 nm/s the substrate temperature needs to be > 300°C [**?**] However, for p-i-n solar cell deposition this temperature load for the previously deposited p-layer leads to a reduction of the power conversion efficiency. This is demonstrated by the data in Table 1.1, for solar cells with an intrinsic layer deposited at different temperatures and growth rates of ~ 1 nm/s. The efficiency drops from 5.8% at 200°C to 3.7% at 400°C. Also both open circuit voltage and short circuit current density show a substantial decrease.

It is evident that for deposition of solar cells with > 7% efficiency at ~ 1 nm/s by ETP-CVD, the deposition temperature must be lowered while maintaining the material quality. It is not yet understood why higher substrate temperatures in ETP-CVD are required, but some ideas were suggested. Surface diffusion of growth precursors as well as other mobile surface groups is a thermally activated process. At low substrate temperatures the surface mobility might be too low compared to the growth flux arriving on the substrate surface, which is assumed to result in the implementation of voids in the material. Secondly, positively charged cluster ions are expected to make a contribution of up to 10% to the total growth flux [38]. These ionic clusters could have an adverse

Table 1.1 Overview of solar cells deposited at different substrate temperatures with ETP-CVD.

Temperature °C	Efficiency %	Short Circuit Current mA/cm^2	Open Circuit Voltage V	Fill Factor a. u.
200	5.8	133.0	0.81	0.53
300	4.0	123.9	0.65	0.5
400	3.7	123.1	0.63	0.47

effect on the material properties of a-Si:H films, which might be compensated for at higher substrate temperatures.

Both effects described above could be circumvented by ion bombardment on the substrate surface. Ions are inherently present in a plasma, typically positively charged ions, which are balanced by free electrons to achieve quasineutrality in the plasma [39]. By applying a substrate bias to the substrate surface, these positively charged ions are accelerated towards the substrate at negative potential where they bombard the surface, transforming the potential difference between plasma and substrate first into kinetic energy and then ideally into thermal energy on the substrate surface. In this way energy is provided only to the substrate surface and would not affect the p-i interface, thus avoiding the temperature load on the p-layer that causes the decrease in solar-cell efficiency. As will be discussed in this thesis, the idea is to replace substrate temperature with kinetic energy due to ion bombardment. The type of interaction between bombarding ions and surface atoms depends on the kinetic energy of the ion bombarding the surface and will become important during the discussion in this work.

During a-Si:H thin film growth the surface layer continuously transforms into bulk film - understanding processes on the film surface means gaining insight into how the film grows. Therefore studying the surface of a-Si:H in situ during film growth is essential to ultimately understand the effect ion bombardment on the surface. An interesting technique that was developed in the last decades to monitor film growth non-destructively and in situ is Spectroscopic Ellipsometry (SE), which will be discussed in detail in the experimental section. It allows to determine properties like film thickness, dielectric function and, most importantly for this work, the surface roughness in situ during the deposition of the film and at a quick measurement speed to obtain a high resolution in the time domain. Especially the surface roughness will be an important parameter, as it can be used as a measure for the mobility of mobile species on the substrate surface: rough surfaces can be the result of low mobility precursors, whereas smooth films indicate a good mobility of precursors, enabling them to reach surface valleys before being implemented in the film. Due to its relative

novelty in ETP-CVD, we will use SE not only to investigate the effect of ion bombardment on the substrate surface. A part of this work will be devoted to study the effect of other deposition parameters on the film growth and surface roughness development.

In chapter 2 experimental details will be discussed, with a focus on substrate biasing techniques and in-situ spectroscopic ellipsometry. Chapter 3 discusses the effect of RF substrate biasing on a-Si:H films grown at different reactor pressures, focusing on the effect both reactor pressure and RF biasing have on the critical hydrogen concentration at which the microstructure changes from void dominated to vacancy dominated material. Chapter 4 discusses pulse-shaped biasing and its effect on material properties in detail. In the first section ion energy distributions obtained from pulse-shaped biasing are presented and the quality of control over the ion energy is discussed. In the second section the effect of different ion energies on material properties of a-Si:H in the range from unbiased deposition up to ion energies of 200 eV are discussed and related to interactions that occur between bombarding ions and surface Si atoms. This section also highlights the unique experimental observation of a decreasing band gap at increasing hydrogen concentration, from which new insight of band gap dependence on microstructure is gained. In chapter 5 pulse-shaped biasing is applied during intrinsic a-Si:H deposition in p-i-n solar cells. Knowledge gained on pulse-shaped biasing in chapter 4 is applied to explain how solar cell properties are affected as a result of changes in the the intrinsic layer. Chapter 6 focuses on the surface roughness development during deposition of a-Si:H films as observed with in-situ spectroscopic ellipsometry. In the first section the influence of substrate temperature and RF substrate biasing on the surface roughness development is discussed and the presence of a hydrogen-rich subsurface layer is suggested. In the second section the influence of hydrogen dilution on the surface roughness development is discussed and further insight into the hydrogen-rich layer is gained. A general conclusion of this thesis will be given in chapter 7.

Chapter 2

Experimental

2.1 Deposition of a-Si:H with Expanding Thermal Plasma Chemical Vapour Deposition (ETP-CVD)

2.1.1 Experimental Deposition Setup CASCADE

Most depositions reported in this work were carried out in the CASCADE setup, the **C**ascaded **A**rc **S**olar **C**ell **A**pparatus **D**elft **E**indhoven. It consists of three vacuum chambers, two for material deposition and one for sample transfer and loading. One deposition chamber in the CASCADE setup utilizes the expanding thermal plasma chemical vapor deposition technique (ETP-CVD) for the deposition of intrinsic a-Si:H. The second deposition chamber employs radio-frequency plasma-enhanced chemical vapor deposition (rf-PECVD) for deposition of both p- and n-doped a-Si:H layers. The setup has been specifically designed to allow deposition of p-i-n solar cells without exposing the sample to atmospheric conditions during sample transfer.

At the core of the CASCADE setup is the expanding thermal plasma CVD (ETP-CVD) reactor, short ETP. This reactor is used for the deposition of intrinsic a-Si:H. The method was developed at the Plasma & Materials Processing group of Eindhoven University of Technology (TU/e) with the aim to deposit a variety of materials at high growth rates, like a-C:H [40, 41], SiN [42, 43], or diamond-like films [44]. It is a so-called remote plasma technique where plasma creation, plasma transport and film deposition occur in separate regions of the reactor. Due to the spatial separation and the large pressure difference between the plasma source and the deposition region, processes in the deposition area do not influence the plasma source. In a direct plasma like rf-PECVD the substrate itself acts as one of the electrodes sustaining the plasma, which results

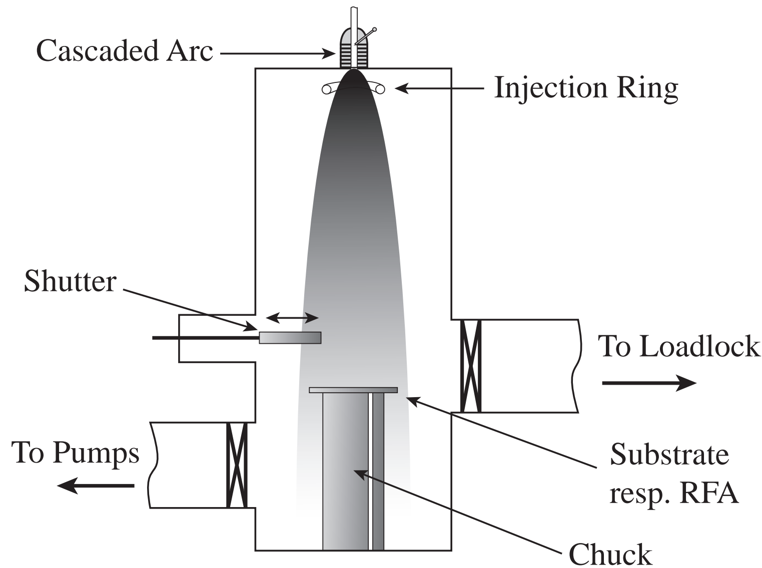

Figure 2.1 Schematic drawing of the ETP-CVD reactor.

in considerable ion bombardment on the substrate surface with a broad ion energy distribution [45]. Due to the remote nature of the ETP, ions that arrive on the substrate surface have a much lower energy < 2 eV [46]. The advantages are that growth of a-Si:H films can either be studied without the influence of ion bombardment where all energy is provided by the substrate temperature, or ions can be accelerated towards the substrate surface in a controlled way, allowing to study the influence of ion bombardment schematically as will be discussed in the next section.

The ETP-CVD setup can be seen schematically in Fig. 2.1. The cascaded arc at the top of the reactor consists of six electrically insulated copper plates, with the bottom plate serving as the anode. Three cathode tips are placed at the top of the arc, with the tip placed in the center of the copper plates. Each plate has a circular open space in the middle with a diameter of 2.5 mm. Together these circular holes form the plasma channel into which Ar and H_2 gas is injected. All gas flows in this setup are controlled by separate mass flow controllers. Under sufficiently high voltages between the cathode tips and the anode plate an Ar-H_2 plasma is ignited and sustained at pressures typically in the 0.5 bar range. Power is dissipated exclusively in the arc between 5 - 8 kW. The plasma is injected into the deposition chamber with a volume of 70 l through a nozzle directly below the arc. The nozzle also serves as additional injection point for H_2. The deposition chamber is kept at pressures much lower

than the arc, typically around 0.2 mbar. This pressure difference is achieved by two stacked root blowers with pumping capacities of 1200 and 500 m^3/h (Edwards Mechanical Booster EH 1200 and EH500A, respectively) backed by an 80 m^3/h rotary pump (Edwards Super 80), resulting in an effective pumping speed of $\sim$ 500 m^3/h. Residence time of stable particles in this reactor is of the order of 0.5 - 0.6 s. The pressure difference leads to a supersonic expansion of the plasma into the deposition chamber, and a subsonic expansion after a stationary shock. At about 4.5 cm below the nozzle a stainless steel injection ring is located which serves as injection point for silane (SiH_4) which reacts with the plasma to form predominantly silyl radicals, SiH_3. The temperature controlled substrate holder is located about 43 cm below the injection ring, with a maximum temperature of 450°C. Silyl radicals deposit on the substrate surface placed on the substrate holder and form an a-Si:H thin film.

At sufficiently high H_2 flows the cascaded arc acts as an efficient atomic hydrogen source [46]. Under these conditions SiH_4 dissociation is governed by hydrogen abstraction following:

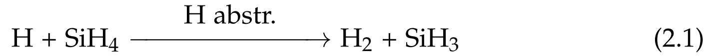

$$H + SiH_4 \xrightarrow{\text{H abstr.}} H_2 + SiH_3 \tag{2.1}$$

In ETP-CVD, the growth flux consists predominantly of SiH_3 with a contribution of about 90% to the total growth flux [47]. SiH_3 dominated growth flux typically results in solar grade a-Si:H suitable for solar cell application. However, even at sufficienctly high H_2 flows there is still a small contributions of H^+ ions from the arc. These ions can lead to the formation of polysilane radicals following the reaction scheme below:

$$H^+ + SiH_4 \xrightarrow{\text{Charge transf.}} SiH_n^+ + ... \ (n \leq 3) \tag{2.2}$$

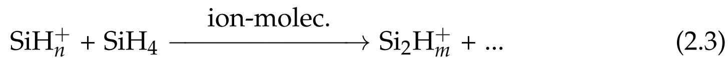

$$SiH_n^+ + SiH_4 \xrightarrow{\text{ion-molec.}} Si_2H_m^+ + ... \tag{2.3}$$

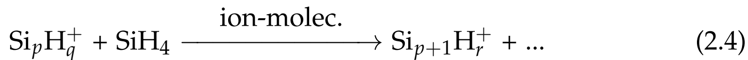

$$Si_pH_q^+ + SiH_4 \xrightarrow{\text{ion-molec.}} Si_{p+1}H_r^+ + ... \tag{2.4}$$

Polysilane molecules can contribute up to 10% to the growth flux [47]. They have a high surface reaction probability with the substrate surface and a detrimental effect on a-Si:H properties. Negatively charged ions in the plasma could not be detected so far, but their detection is known to be difficult due to their confinement within the plasma by the plasma sheath. However, biasing experiments that will be discussed in Chapter 4 indirectly suggest the presence of significant negative ion concentrations in the plasma. Dust particles have so

far not been experimentally observed either in an ETP reactor, but for similar reasons their presence can not be excluded either.

Doped p- and n-layers can be deposited in the rf-PECVD reactor. In this reactor the top electrode also serves as a temperature controlled substrate holder. The top electrode is typically used as substrate holder in rf-PECVD reactors to avoid dust that can potentially be generated in the plasma to fall on the substrate surface. While in principle both p- and n-doped layers can be deposited, for the solar cells reported in this thesis only the n-layer was deposited in this reactor. For the fabrication of solar cells reported in this work, p-layers as well as a thin intrinsic buffer layer were deposited in a separate rf-PECVD reactor for which optimized deposition procedures have been developed, and afterwards the substrates were transfered into the CASCADE setup.

2.1.2 Substrate Biasing Techniques

As mentioned above, due to the low self-bias in ETP-CVD the average ion energy is < 2 eV [46]. This makes the ETP an ideal system to study the effect of external substrate biasing as a tool to obtain controlled ion bombardment on the substrate surface. The chuck on which the substrate holder is placed is electrically isolated from the reactor walls or any other grounded component of the setup. It is therefore at floating potential during depositions. In this work, two different types of substrate biasing have been used, sinusiondal rf biasing and pulse-shaped biasing (PSB). Both sinusoidal rf and pulse-shaped biasing setups are connected to the same coaxial connection at the bottom side of the substrate holder. Martin et al. [48] determined for ETP-CVD deposition conditions similar to ours that the mean free path of the ions in the plasma sheath is comparable to the sheath thickness. Therefore collisions in the sheath can occur, which could lead to broadening of the ion energy distribution.

Sinusoidal RF Substrate Biasing

Under RF substrate biasing one understands the application of a sinusoidal AC voltage signal at a frequency of 13.56 MHz to the substrate holder. The signal is alternating between negative potential and a potential slightly above floating potential, and in turn also positive and negative charge carriers, respectively, will be accelerated towards the substrate. A schematic version of an RF voltage profile on the substrate surface can be seen in Fig. 2.2. Ideally these two currents consist of positively charged ions and negatively charged electrons. The two currents will automatically balance each other out as a result of a blocking capacitor that is present between the rf power source and the substrate holder. In a system where positive and negative charge carriers have the same mobility this would lead to a symmetric distribution of the AC signal around the

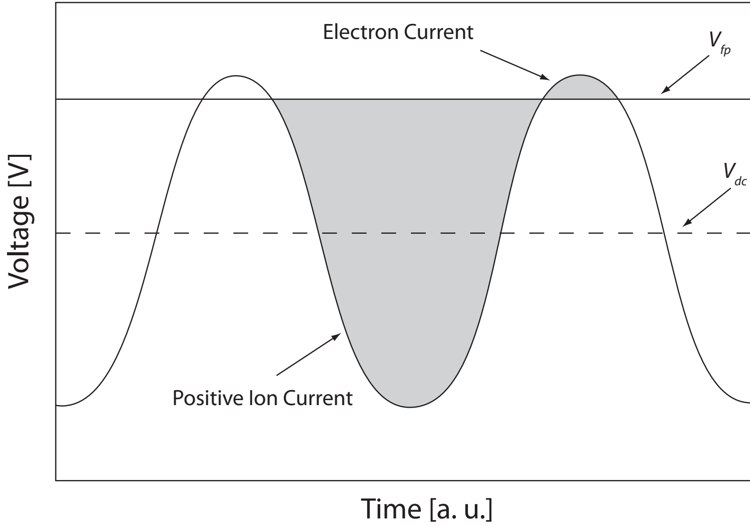

Figure 2.2 Schematic version of an RF voltage profile on a substrate surface during 13.56 MHz RF substrate biasing. Shown in the figure are also the DC voltage shift V_{dc} as well as the floating potential V_{fp}.

floating potential V_{fp}. However, electrons have a significantly higher mobility in the plasma compared to the heavy, positively charged ions. If the AC signal was symmetric around V_{fp}, this would lead to a much higher electron current compared to the positive ion current. Consequently the AC signal shifts towards negative voltages to re-establish the balance between the two currents. This shift increases the voltage shift V_{dc} that results from the difference in area size of powered electrode (substrate holder) and and grounded electrode (reactor walls). Typically the fraction of positive voltage on the substrate surface is much shorter than the duration of one sinusoidal cycle. The remaining part of the cycle is in the voltage range below V_{fp}.

RF substrate biasing results in a broad ion energy distribution (IED). The exact shape of the IED depends on the ratio between the ion transit time of the sheath region, τ_{ion}, and the rf period, τ_{rf}, and is a function of the frequency of the applied waveform. For $\tau_{ion}/\tau_{rf} \ll 1$, ions can pass through the sheath within one period. The energy of the ion is determined by the phase of the waveform in which the ion enters the sheath. Since the voltage change is slowest close to the minimum and maximum voltages, more ions cross the sheath during these phases of the biasing which explains the two peaks in the IED spectrum with a dominant energy peak at low ion energies [50]. Such an IED can be seen in Fig. 2.3(a) for different peak-to-peak voltages. The center of the bimodal distribution is located at the mean sheath voltage, V_s. For $\tau_{ion}/\tau_{rf} \gg 1$

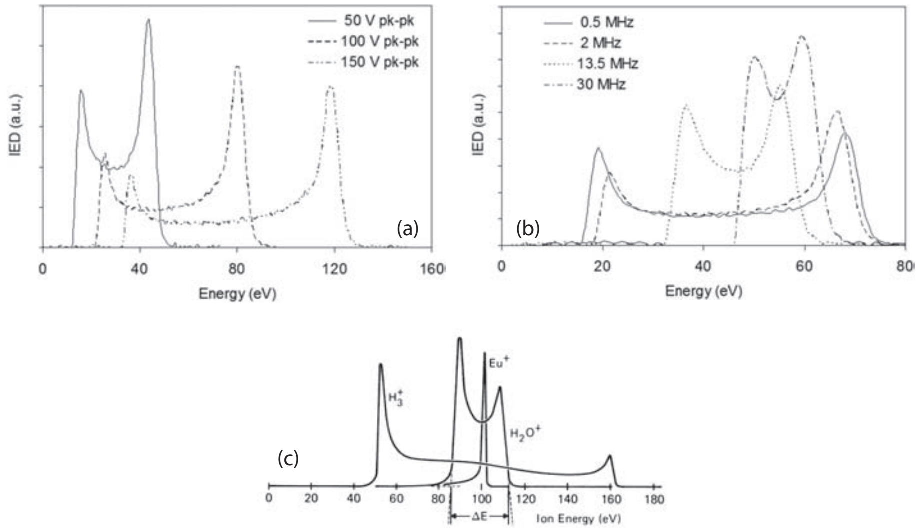

Figure 2.3 IED measurements for sinusiodal rf substrate biasing. The IED as a function of peak-to-peak voltage can be seen in (a) and as a function of frequency in (b) (both taken from [49]). For frequencies of 13.56 MHz the exhibits mass dependence which can be seen in (c) (taken from [50]).

ions can not directly transit through the sheath region anymore within one period and charge exchange collisions become important. The number of periods it takes an ion on average to pass through the sheath region is reflected in the IED, where an additional number of peaks roughly equal to these numbers of periods appears at lower energies compared to the low-energy peak of the bimodal distribution [50, 51]. In the transition region between the two extreme cases of $\tau_{ion}/\tau_{rf} \ll 1$ and $\tau_{ion}/\tau_{rf} \gg 1$, the distance between the two peaks of the bimodal IED decreases with increasing biasing frequency and the height of the high-energy peak increases [50]. Examples of IEDs at different frequencies can be seen in Fig. 2.3(b). This narrowing of the IED with increasing frequencies can in principle be used as a method to obtain a narrow IED with rf biasing, but the method suffers from two problems: (i) at very high frequencies the IED becomes mass dependent and remains bimodal for for low mass ions, as can be seen in Fig. 2.3(c), and (ii) non-uniformities in the substrate voltage occur once the rf wavelength approaches the dimensions of the substrate, leading to non-uniform ion bombardment.

τ_{ion} can be calculated (see e. g. reference [39]) following:

$$\tau_{ion} = 3 \cdot \left(\frac{m_i}{2 \cdot e \cdot V_s} \right)^{\frac{1}{2}} \cdot d_{sheath} \tag{2.5}$$

with m_i the positive ion mass, V_s the plasma sheath potential and d_{sheath} the plasma sheath thickness following:

$$d_{sheath} = \frac{4}{3} \cdot \lambda_D \cdot \left(\frac{e \cdot V_s}{2k_B T_e} \right)^{\frac{3}{4}} \tag{2.6}$$

with T_e the electron temperature and λ_D the Debye length [39]. At rf frequencies of 13.56 MHz applied in this work, $\tau_{rf} = 0.074$ μs and $\tau_{ion} \sim 0.4$ μs [48], leading to $\tau_{ion}/\tau_{rf} \sim 5.4$. In this range of τ_{ion}/τ_{rf} we expect a broad, bimodal distribution that already exhibits notable mass dependence.

RF biasing has already been used in ETP-CVD in the past for SiN deposition [43] and for a-Si:H deposition [48,52,53]. For SiN deposition at growth rates of 3 nm/s and substrate temperatures of < 150°C Assche et al. observed an increase in density with increasing ion energy [43]. Petit et al. [53] prepared a-Si:H films and reported an optimum V_{dc} of 24 V with a maximum for the refractive index at 2 eV as well as a reduction in Urbach energy and defect density. For the same material Smets et al. [52] suggests three separate phases based on experimental observations: at low $V_{dc} < 50$ V densification of the films, reduction of nanovoid concentration and defect concentration is observed. At medium voltages < 150 V an increase in vacancy concentration is reported, and at high energies > 150 V an increase in nanovoid concentration is observed. Comparable results are obtained by Martin et al. [48], additionally they investigated the secondary plasma formed around the substrate holder during rf biasing and observed a so-called 'α to γ' transition of the plasma at high rf powers, which is correlated to formation of large, negatively charged particles and a decrease in electron density.

The power supply used to induce 13.56 MHz RF biasing on the substrate surface was a AMN100C 100W power supply from Coaxial Power Systems. The power supply was connected to an automated L-type matching network (AMN 100N, Coaxial Power Systems) for impedance matching. The output of the matching network was connected to the substrate holder with a copper strip. The ground connection of the matching network was connected to the same ground as the reactor walls. The average substrate voltage V_{dc} has been measured via a voltage probe connected to the substrate holder. The dependence of V_{dc} on the power output of the rf power supply has been investigated by Martin et al. [48] for pure Ar, Ar/H_2 and $Ar/H_2/SiH_4$ plasmas and can be seen in Fig. 2.4. Although the exact currents will be different under the deposition conditions used in this work the observed trends will be similar.

Pulse-Shaped Biasing(PSB)

The pulse-shaped biasing (PSB) technique is a biasing technique developed by Wang et al. [54] with the aim to control the IED. They developed a setup to con-

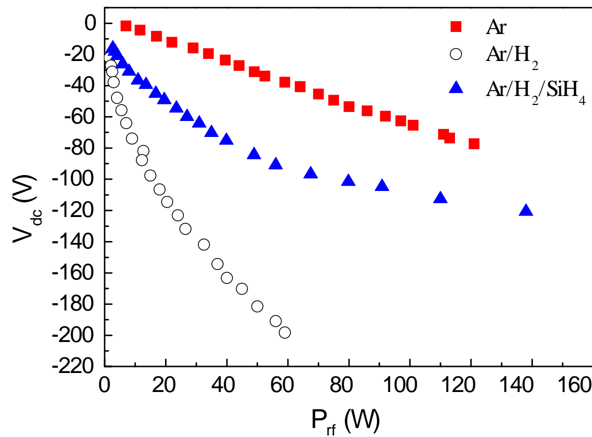

Figure 2.4 Average substrate bias voltage V_{DC} measured during RF biasing for pure Ar, Ar/H_2 and Ar/H_2/SiH_4 plasmas at different applied sinusoidal rf power (taken from [48]).

trol the ion energy in ion etching processes and to increase the aspect ratio of etched features in a remote plasma setup (helicon plasma etch tool). Although our intended application of thin-film deposition with controlled ion bombardment is very different from etching, the principle of controlling the IED remains the same for all remote plasmas with self-bias.

Glass or other insulating substrate materials do not allow applying a constant DC substrate voltage due to charge build-up on the substrate which would lead to a change in voltage on the substrate surface. Therefore the applied waveform must fulfill two criteria:

1. The substrate must be discharged regularly
2. The charge buildup in the substrate must be counteracted

These requirements lead to the waveform shown by the solid line in Fig. 2.5(a). It consists of a ramp and a pulse. During the ramp the voltage output of the applied signal is constantly reduced to balance exactly for the buildup of charge on the substrate surface. Discharging of the substrate occurs during the short positive peak, allowing electrons in the plasma to neutralize the positive charge on the substrate. As explained in the previous section, the mobility of the electrons in the plasma is much larger than the mobility of the positive ions. Therefore the pulse can be much shorter than the ramp to obtain a current balance. The resulting, flat potential at the substrate holder in between the discharge pulses is schematically shown in Fig. 2.5(b). This flat potential on the substrate results in a very narrow IED of bombarding ions, broadened only

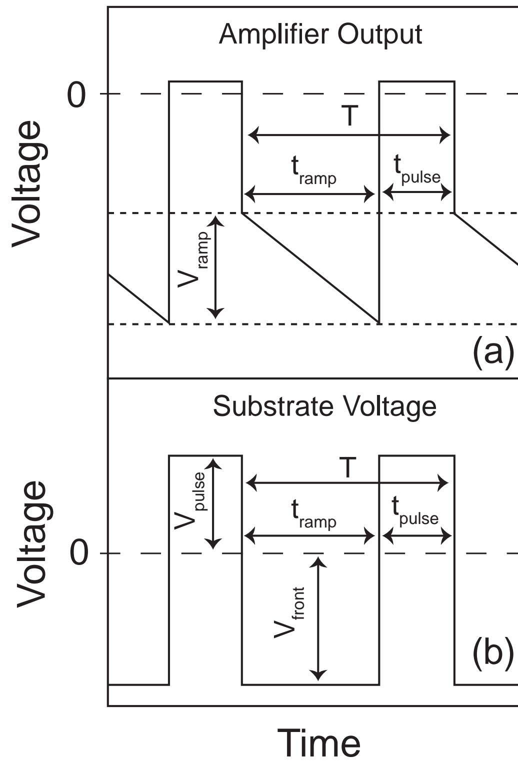

Figure 2.5 Schematic versions of the applied pulse-shaped waveform (a) at the broadband amplifier output and (b) on the substrate surface. Important characteristics of the waveforms are indicated in the figure.

due to slight voltage variations of the output signal of the amplifier as well as ion-collisions in the plasma sheath. There will also be no mass dependence as discussed for high frequency rf biasing.

The setup used to create this waveform can be seen in Fig. 2.6. The non-sinusoidal wave is created by an arbitrary waveform generator (Agilent 33250A). A broadband amplifier (Amplifier Research 150A250) with an amplification range from 10 kHz up to 250 MHz is used to control the signal amplitude. In principle, this setup enables us to operate in a frequency range for the non-sinusoidal wave from 10 kHz up to 8 MHz (the limit of the arbitrary waveform generator).

In between the amplifier and the substrate holder, a coupling capacitor is installed, which serves two purposes:

1. It serves as a measurement device. On the amplifier side, the output of

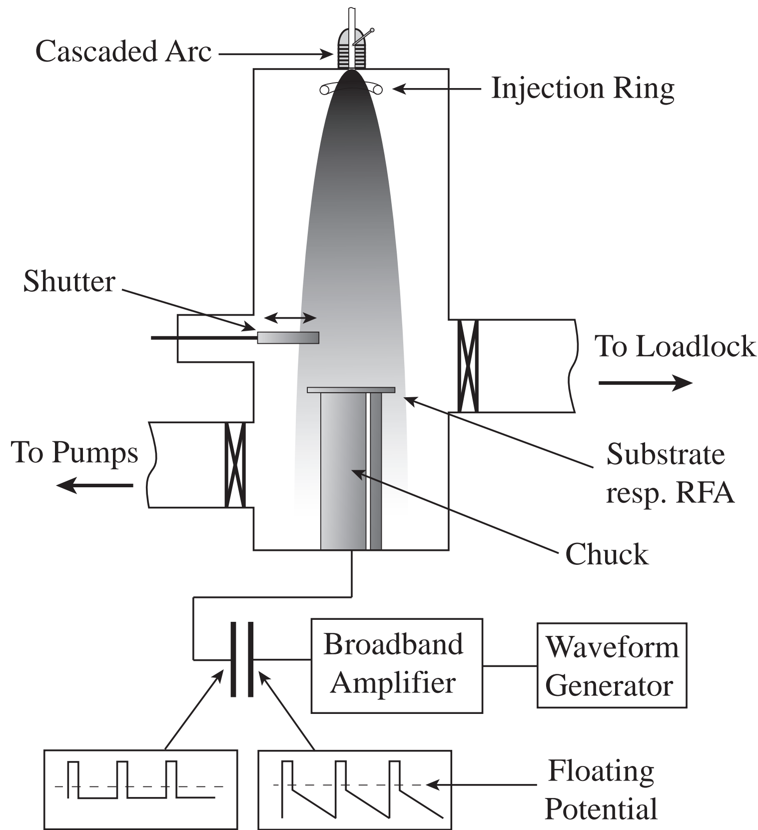

Figure 2.6 Schematic representation of the pulse bias setup connected to the ETP setup. Also shown is the applied signal to the bottom right and the response on the substrate holder during deposition on the bottom left.

the amplifier can be measured, whereas on the substrate side the voltage on the substrate can be measured [54].

2. It ensures that there is no DC offset in the signal. Therefore the same amount of charge discharges the substrate that has previously charged it.

When the pulse-shaped bias is applied, the response of the system to the signal can contain oscillations due to resonances in the electronic circuit formed by the reactor and all components in it. Most of these resonances have a low amplitude or are located in a frequency range not utilized for this application, except one oscillation located at around 400 kHz. This oscillation is the result of a capacitive coupling between the biased substrate holder and the heating

elements located in the chuck with a capacitance of 0.2 nF. The heating elements are connected via the power line in series to an RF-filter with an inductance of around 1 mH. This series connection of capacitor and inductance leads to a resonance frequency of 400 kHz. The resonance can be damped by shunting the power line with a large capacitance (in our case 5 nF), creating a low impedance path for oscillations to ground.

In addition to substrate biasing with controlled ion energy discussed above, the pulse bias setup can also be used to measure the ion flux arriving at the substrate, from which the ion density in the plasma can be deduced. The ion flux can be calculated from the slope of the waveform and the capacitance of the coupling capacitor. The ion flux is an important parameter when analyzing ion bombardment experiments. Not only the ion energy is important to analyze the effect of PSB on deposited material, also the ion-to-radical ratio impinging on the substrate is important.

2.2 Thin Film Characterization

2.2.1 Real-Time Spectroscopic Ellipsometry (RTSE)

Spectroscopic Ellipsometry is based on the principle that polarized light changes its polarization when it is reflected from a thin film. This change in polarization can be measured and analyzed to obtain information about the film. Linearly polarized light which was initially used in ellipsometry measurements usually becomes elliptically polarized after reflection from a thin film, which explains the origin of the term *ellispometry*. In recent years Spectroscopic Ellipsometry (SE) has become a very popular method for thin-film analysis. Main advantage of SE is its non-destructive and non-invasive nature with remarkable precision an very high thickness sensitivity ($\sim$ 0.1 Å); hence the sample is not affected by the measurement in any way and can be reused for further studies. Furthermore it can be used in-situ, e.g., during fabrication or manipulation of the sample, and modifications of physical properties can be monitored in real-time. The most difficult task with SE analysis is the development of the optical model that is necessary for data interpretation, which can become very complicated. Samples can be analyzed very accurately, providing information on [55]:

- the thickness, dielectric function and refractive index,
- the thickness of bulk layers or surface roughness layer,
- the presence of contaminant overlayers, like oxidized surface layers,
- from visible light absorption: band gap, temperature, alloy composition, phase structure (amorphous, crystalline, void), grain size,

- from infrared light absorption: free carrier concentration, mobility, conductivity, phonon absorption, and
- the depth profile of a single- and multilayer structures,

A good overview of the development of spectroscopic ellipsometry was published by Vedam [56]. The first to apply simple ellipsometry as a tool to analyze thin films was Paul Drude in 1888 [57], who also derived the equations still in use today for the analysis of SE data. In 1975 Aspnes and Studna [58] were able to reduce the measurement time of a set of ellipsometric data for one wavelength by automating the previously manual process. Thus ellipsometric measurement could now be conveniently applied to a whole range of the electromagnetic spectrum, leading to *spectroscopic* ellipsometry. While their method still required consecutive measurements for each wavelength, parallel measurement of all wavelengths was the next breakthrough in SE development and was the starting point of spectroscopic ellipsometry as a broadly applied method. Spectroscopic measurement with polarized light was first introduced by Mueller and Farmer [59] and later refined by Kim, Collins and Vedam [60] in the early 1990s. The measurement time for a full spectrum was eventually reduced to a few seconds, which was fast enough to allow real-time measurements in situ during film processing and lead to the development of modern *Real-Time* Spectroscopic Ellipsometry (RTSE). Nowadays RTSE can perform scans of the full visible electromagnetic spectrum; additionally, it can be extended into the IR or UV wavelengths, with measurement times in the millisecond range for a full scan.

Our RTSE measurements were performed using a J. A. Woollam Co., Inc M-2000F rotating compensator spectroscopic ellipsometer. A schematic version of the setup can be seen in Fig. 2.7. The measurement setup and data acquisition were controlled using WVASE 3.486 from J. A. Woollam Co., Inc. Spectra were collected from 250 nm to 1000 nm in 470 separate channels. The angle of incidence was about 68°and the light beam passed through non-strain free windows, so a window effect had to be included in the data analysis. For all in-situ experiments 8 measurements were averaged, resulting in a time resolution of about 1.8 s. For the fitting of our experimental data we used EASE 2.3 or Complete EASE 3.55 by J. A. Woollam Co., Inc. All RTSE measurements were carried out on crystalline silicon wafer substrates (prime wafer, 500-550 μm).

The actual data obtained in an RTSE measurement is the change of the polarization state of the incident light beam, defined by the ellipsometric angles Ψ and Δ as a function of wavelength. Absolute values of Ψ and Δ contain no directly useful physical information about the sample. A fitting procedure with an optical model is required to deduce information like layer thickness or surface roughness. Depending on the sample structure, a single or multilayer model

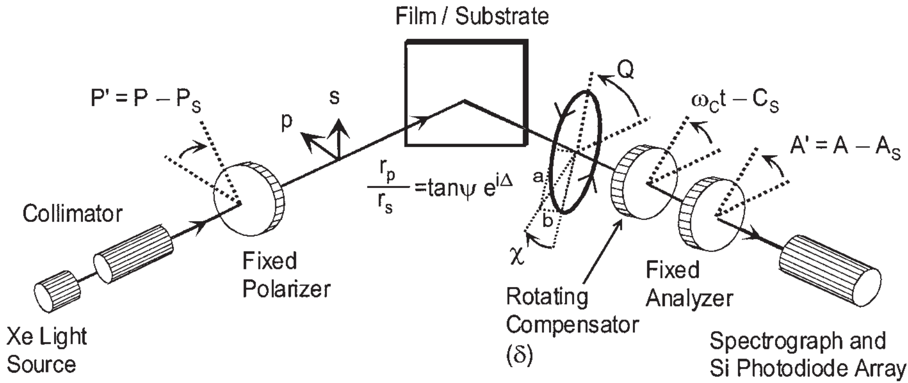

Figure 2.7 Schematic overview of a multichannel rotating compensator spectroscopic ellipsometry setup (taken from [61]).

must be created, in our case consisting of a substrate (crystalline silicon wafer) with a thin bulk film (a-Si:H) and a roughness layer, modeled by a mixture of 50% film / 50% voids, following the Bruggeman effective medium approach (EMA) [62]. In all final fits in this work, the only fitted parameters were usually the bulk film thickness, d_b, and the thickness of the surface roughness layer, d_s, unless specified otherwise.

In our RTSE data analysis we follow a procedure similar to the one established by Van den Oever et al. [63]. The first step is to determine the dielectric function of the substrate. We follow the pseudo-substrate approach and directly determine the dielectric function numerically from the RTSE data by mathematical inversion [64]. This direct approach is possible due to the virtually atomically flat surface of the used c-Si substrates, as the influence of a surface roughness layer can be excluded. In order to allow mathematical inversion of the substrate dielectric function, for every deposition the RTSE measurement was started a few minutes prior to the start of the a-Si:H deposition. The dielectric function of the substrate is thus obtained at the same temperature at which the deposition is carried out, thereby excluding analysis problems due to the temperature dependence of the dielectric function of the substrate.

The dielectric function of the deposited film can be modeled by parameterized models [65]. However, this requires initial assumptions for the starting values of the parameters, so one must already have a good idea of the dielectric function of the material. Additionally, it introduces additional fitting parameters. The approach taken in this work does not require any parameterization of the dielectric function and gives a first estimate for the a-Si:H dielectric function that can be further refined using a parameterized model afterwards. For math-

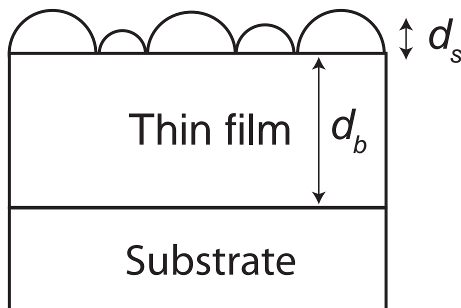

Figure 2.8 A schematic version of the optical model used for most of our analysis.

ematical inversion of the film dielectric function we need to know the dielectric function of the substrate (as determined in the previous step), of vacuum and the incident angle of the polarized light which is obtained from calibration measurements. In this approach, a tabulated, Kramers-Kronig consistent version of the dielectric function is fitted via a global regression analysis using $\sim 8-10$ spectra of the in-situ measurement equally distributed over the deposition time, excluding only the initial 200 Å where the dielectric function is different from the bulk dielectric function [63]. In a regressive fit the dielectric function is repeatedly determined until a minimum in the mean square error (MSE) is reached. Utilizing many spectra stretched over the whole deposition time ensures a good representation of the bulk dielectric function. For this procedure an initial, tabulated version is required as a starting point for the fitting procedure. Surface roughness needs to be implemented in this procedure to obtain an accurate dielectric function of the film.

Once the dielectric functions have been extracted, the dynamic fit of the in-situ data can be carried out. The only parameters in this final, dynamic fit are usually d_b and d_s. A schematic version of our optical model can be seen in Fig. 2.8. The surface roughness d_s can be related to the roughness found by AFM measurements (d_{rms}) via a linear correlation suggested by Koh et al. [66]:

$$d_s = 1.5 \times d_{rms} + 4 \text{ Å} \tag{2.7}$$

Additionally, the dielectric function of the bulk thin film can be fitted separately with parameterized models. An appropriate model must be chosen according to the optical properties of the material. For modelling of the dielectric function in a transparent region of the spectrum, Sellmeier or Cauchy model is used, while for free carrier absorption the Drude model is used [55]. In order to account for absorption in the visible/UV region, various models like the Lorentz, Tauc-Lorentz, Cody-Lorentz or the harmonic oscillator approximation have been used. For amorphous materials the Tauc-Lorentz model has

been used with most success. It can be used for further analysis with additional fitting parameters in the model, as will be demonstrated in Chapter 6.

For amorphous silicon RTSE was used for the first time to study the growth of sputtered amorphous silicon (a-Si) by An et al. [67] . They successfully demonstrated that RTSE is capable of quantitatively analyzing the initial growth phase of thin films. A transition from nucleation to bulk film growth could be observed at a film thickness of 13 Å. Shortly afterwards, RTSE was also applied in studies of hydrogenated amorphous silicon (a-Si:H) grown by PECVD [68].

Collins et al. used RTSE to optimize [69] rf-PECVD grown a-Si:H thin films for solar-cell application. They developed phase diagrams for the transition from the amorphous to the microcrystalline phase as a function of hydrogen dilution. In their work RTSE was used to monitor the roughness development of the films in situ and allowed to determine the transition from pure amorphous film growth to a parallel amorphous and microcrystalline Si:H growth (mixed-phase growth). A strong increase in roughness indicates the start of this transition, whereas a subsequent smoothening indicates the transition from mixed-phase growth to pure microcrystalline growth. An important result was that a-Si:H with the best opto-electronic properties can be obtained at the highest hydrogen dilution that still yields amorphous Si:H with the necessary thickness ($\sim$ 500 nm for the intrinsic layer thickness in a solar cell).

Recently, also thin a-Si:H films grown by Hot-Wire (HW) CVD are being investigated by RTSE. Levi et al. [70] were able to reveal a 100-200 Å thick zone at the substrate interface with a constant hydrogen concentration independent of deposition temperature which could not be resolved by SIMS, thus demonstrating the sensitivity of RTSE for very thin layers. In another article [71] they developed a phase diagram similar to Collins et al. [69] to determine the transition from a-Si:H to μc-Si:H as a function of hydrogen dilution for HW-CVD. Kessels at al. [72] applied RTSE to study surface processes and especially thermally activated surface diffusion of a-Si:H deposited by HW-CVD a-Si:H, focusing on the initial growth phase. Additionally they observed similar smoothening and roughening trends like Collins et al. [69] for PECVD a-Si:H.

So far RTSE has not been used for in-situ studies of a-Si:H films grown by ETP-CVD. However, single-wavelength ellipsometry has been applied by Smets et al. [73, 74]. They confirmed the common observation that thin a-Si:H films grown by ETP-CVD show the same decrease in surface roughness with increasing deposition temperature typically observed for a-Si:H growth. Furthermore, rougher surfaces are obtained compared to films grown by rf-PECVD or HW-CVD at similar deposition temperatures. The presence of a thermally activated smoothening process was suggested, based on analysis of the dynamic scaling exponent, β [74]. However, due to the high growth rates of $>$ 3 nm/s used in

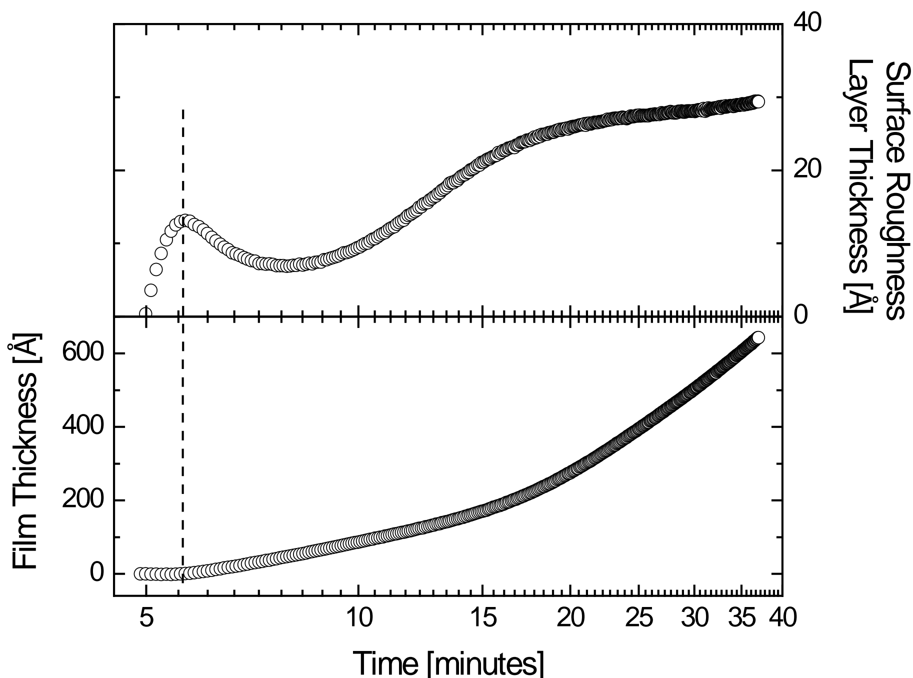

Figure 2.9 An example for a-Si:H surface roughness layer thickness development (a) and bulk film thickness (b) obtained with RTSE.

their work even the fast single-wavelength ellipsometry was not able to resolve the initial growth phase of the films where smoothening was observed for other deposition methods.

An example of surface roughness layer thickness and bulk film thickness development can be seen in Fig. 2.9(a) and (b), respectively. The surface roughness shows commonly observed trends [72,75]. In the beginning of the deposition the roughness increases strongly. It is commonly interpreted that in this phase the film nucleates on the substrate surface on randomly distributed nucleation sites and subsequently nuclei grow presumably semi-spherically on the surface. Sticking of growth precursors in between the nuclei is negligible. In this phase no closed film exist on the surface, which is in agreement with the fact that the bulk film thickness in this phase is around 0 Å as can be seen in Fig. 2.9(b). At the roughness maximum the nuclei coalesce and a closed film is formed. From the roughness maximum of $\sim$ 15 Å and assuming semi-spherical nuclei we determine a nucleation site density of $\sim 1.4 \times 10^{13}$ cm^{-2}. At this first roughness maximum the bulk film thickness begins to increase while the roughness starts to decrease due to smoothening of the roughness features at

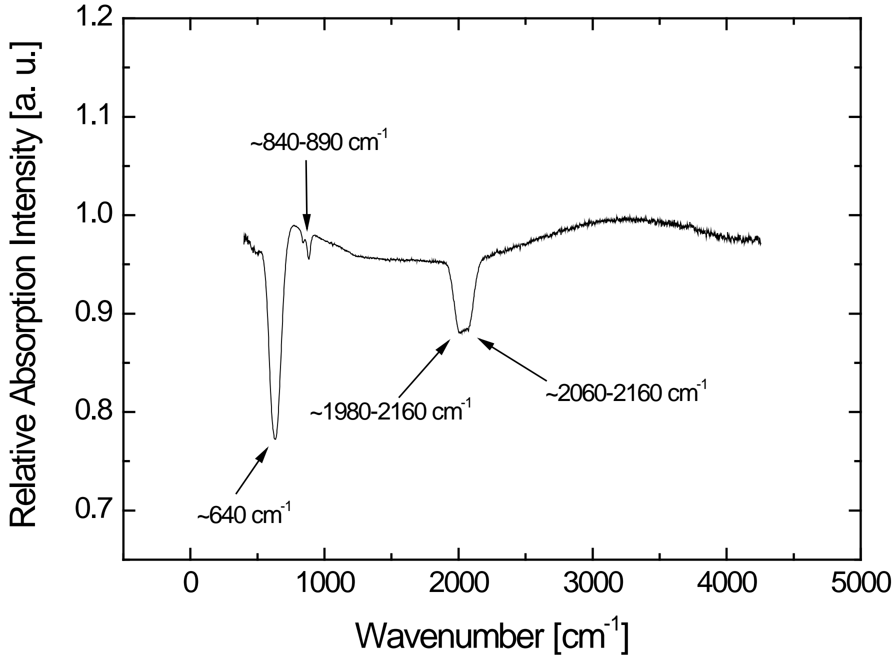

Figure 2.10 An example of an FTIR measurement, including the main absorption modes and the interference fringes.

short lateral length scale. After a minimum in surface roughness it increases again, this time presumably on a much longer lateral length scale that can not be smoothened efficiently anymore by the surface mass transport mechanisms on the a-Si:H surface [72].

2.2.2 Fourier Transform Infrared Absorption Spectroscopy (FTIR)

In a-Si:H the microstructure, i. e. the way hydrogen is incorporated into the amorphous silicon matrix, is known to have a significant effect on important material properties, e. g. electrical conductivity, band gap and density. The most common technique to study this microstructure is Fourier Transform Infrared absorption spectroscopy (FTIR). The FTIR setup used in this work is the Nicolet 5700 from Thermo Electron Corporation. It has a measurement range from 350 - 7000 cm^{-1}. All measurements were carried out on crystalline silicon wafers (prime wafer, 500-550 μm), since glass has a high absorption coefficient in the wavenumber range interesting for a-Si:H analysis (500 - 2200 cm^{-1}).

The Si-H bonds absorb infrared light in three distinct ranges of wavenum-

bers which are related to certain bonding configurations, each associated to specific modes. All absorption modes are indicated in a sample measurement shown in Fig. 2.10. A wagging mode can be seen at 640 cm^{-1}, bending modes in the 840-890 cm^{-1} range and stretching modes in the 1980 - 2160 cm^{-1} range. All Si-H_x bonds contribute to the wagging mode, which can therefore be used to determine the total hydrogen concentration in the film. The stretching mode consists of two separate modes, one mode around 1980-2030 cm^{-1}, hereafter called the low stretching mode (LSM) and a second mode around 2060-2160 cm^{-1}, hereafter called high stretching mode (HSM). The difference between these modes will be discussed below. The microstructure parameter R^* is defined as:

$$R^* = \frac{I_{HSM}}{I_{LSM} + I_{HSM}} \tag{2.8}$$

with I_{HSM} and I_{LSM} the integrated absorption strength of low stretching mode and high stretching mode, respectively. It is commonly observed that a-Si:H with low conductivity, low density and a higher defect density typically has a high R^*, while device quality a-Si:H with high conductivity, high density and low defect density generally exhibits $R^* < 0.1$ [76].

For the data analysis of FTIR measurements, we first fit the interference fringes of the sample background to determine the refractive index for infrared light and the film thickness. From the integrated absorption strength for each separate absorption mode we can determine the density of bonds in the associated mode following:

$$N_x = A_x I_x = A_x \int \frac{\alpha(\omega)}{\omega} d\omega \tag{2.9}$$

with A_x the proportionality constant and $\alpha(\omega)$ the absorption coefficient as function of wavenumber. Different proportionality constants have been published in literature for each absorption mode, determined e. g. by nuclear techniques or hydrogen effusion experiments. In our analysis we used proportionality constants for $A_{640} = 1.6 \times 10^{19}$ cm^{-2} determined from Kessels et al. [77] by means of elastic recoil detection analysis, and $A_{LSM} = A_{HSM} = 9.1 \times 10^{19}$ cm^{-2} determined by Smets et al. [76].

As described above, all hydrogen bonds contribute to the wagging mode at 640 cm^{-1}. We can therefore determine the total hydrogen concentration c_H by means of the wagging mode bond density N_H and the silicon density N_{Si} as follows:

$$c_H = \frac{N_H}{N_{Si} + N_H} \tag{2.10}$$

For our analysis we assumed $N_H + N_{Si}$ around 5×10^{22} cm^{-3} as suggested by Kessels et al. [77].

The stretching mode of Si-H bonds is affected by both the surrounding environment of the H atom as well as the number of H atoms bonded to one silicon atom, i. e. either one (monohydride) or two (dihydride) H atoms per Si atom. The hydrogen atom can reside in vacancies which are the result of one or more missing Si atoms in the amorphous matrix. If one Si atom is missing we speak of an monovacancy, for two missing atoms of a divacancy and for more than two atoms missing we speak of a polyvacancy. A monovacancy is occupied by four H atoms, a divacancy holds 6 H atoms and a polyvacancy with m atoms missing holds $2m + 2$ H atoms [76]. For large m we do not speak of vacancies anymore and instead refer to a nanovoid, where the internal surface of the void is saturated with H atoms. How exactly the bonding configuration and the surrounding environment affect the stretching modes is topic of ongoing debate. In our data analysis we follow Smets et al. [76]: monohydrides in vacancies are predominantly associated to the LSM at 1980-2030 cm^{-1}, hydrides on void surfaces contribute predominantly to the HSM at 2060-2160 cm^{-1}. Following this interpretation, the R^* value is a measure for the amount of nanovoids in the material. Nanovoids typically result in material with optoelectronic properties unsuitable for solar cell application.

From the refractive index in the infrared, n_∞ as well as the total hydrogen concentration c_H, it is possible to determine the mass density of the a-Si:H film. Following the Clausius-Mossotti equation [78], we obtain:

$$\rho = \frac{n_\infty^2 - 1}{n_\infty^2 + 2} \cdot \frac{3m_{Si}}{4\pi(2\alpha_{Si-Si} + \frac{c_H}{1-c_H}(\alpha_{Si-H} - \frac{1}{2}\alpha_{Si-Si}))} \tag{2.11}$$

with the α_{Si-Si} the bond polarizability of the Si-Si bond, α_{Si-H} the polarizability of the Si-H bond and m_{Si} the mass of the Si atom. In our analysis we used $\alpha_{Si-Si} = 1.96 \times 10^{-24}$ cm^{-3} and $\alpha_{Si-H} = 1.36 \times 10^{-24}$ cm^{-3} as suggested by [78].

2.2.3 Reflection-Transmission (RT) Spectroscopy

For an opto-electronic device like a solar cell, knowledge of the optical properties of the involved layers is essential to understand the behaviour of the solar cell. In order to determine the reflection, transmission and absorption of the a-Si:H thin films as function of wavelength, we carried out reflection-transmission (RT) spectroscopy measurements. With this technique we obtain, the refractive index $n(\lambda)$, the extinction coefficient $k(\lambda)$ and the absorption coefficient $\alpha(\lambda)$ as a function of wavelength. Furthermore the band gap E_g can be determined, an important parameter for any solar cell.

Our RT measurements were carried out with a home-built RT setup on samples deposited on Corning 7059 glass with the light entering the sample from the film side. It consists of a 50 W halogene lamp, a SPEX 1680B monochromator and filters for suppression of higher orders from the monochromator. Both reflected (R) and transmitted (T) light are directly measured by separate silicon photodiodes, while the absorption (A) is determined from the relationship $A = 1 - R - T$. The measurement range was from 1.17 - 2.95 eV.

Data analysis was carried out with the the Opta 3.0 software. From interference fringes in the spectra the film thickness is determined. Several methods exist to determine the band gap in a-Si:H from RT spectra. The band gap is generally defined as the energetic difference between valence band and conduction band. In crystalline materials the bandgap is usually well defined. For amorphous material however, due to tail states in the band edge, it is difficult to determine the band gap and the tail states must be considered in the analysis. Charge carriers located in tail states are usually localized, while those in extended states are mobile, which lead to an alternative definition of the band gap as mobility gap, with the conduction and valence band mobility edges defining the band gap.

A measure for the band gap is obtained from the E_{04} band gap which is simply the photon energy at which the absorption coefficient $\alpha = 10^4$ cm^{-1}. A less ambiguous method was suggested by Tauc et al. [79] and is based on the following relation between band gap and absorption coefficient:

$$(\alpha h\nu)^{1/(p+q+1)} \sim (h\nu - E_g) \tag{2.12}$$

where p and q are parameters that determine the shape of the band edges. Tauc et al. [79] assumed parabolic band edges which gives $p = q = \frac{1}{2}$. Following this relation, the Tauc band gap can be determined by plotting $(\alpha h\nu)^{1/2}$ vs. $h\nu$ and extrapolating the linear part of the obtained plot to zero. The typical Tauc band gap obtained for a-Si:H is $\sim$ 1.75 eV. The Klazes band gap can be determined very similar assuming linear band edges ($p = q = 1$), but in this work we only consider the Tauc band gap.

2.2.4 Dual Beam Photoconductivity (DBP) and Fourier Transform Photocurrent Spectroscopy (FTPS)

Ideal semiconductors have no energetic states between conduction and valence band. In most materials, however, states in this forbidden gap are present, and in the case of amorphous silicon they can be present in considerable concentration, affection the electric properties of the material and leading to a continuous density of states as can be seen in Fig. 1.4(b). These energetic states in the

band gap are called defect states. They are usually the result of dangling bond configurations in the material that are not saturated by a H atom.

Although defect states are only present in relatively low concentration, $\sim 10^{15}$ cm^{-3} for solar grade material, they do have a considerable effect on the electronic properties. However, since the concentration of these defects is so low it can not be determined directly from regular R-T measurements which have too low sensitivity. Therefore the defect density is determined from indirect measurements.

Dual Beam Photoconductivity (DBP)

The dual beam photoconductivity (DBP) measurement technique is based on the decrease in conductivity of the film when the free charge carrier concentration decreases. The photoconductivity is measured as function of photon energy, starting at high energies in the visible range and decreasing the energy until photon energies < 1 eV are reached.

Our home-built DBP setup consists of a chopped (13 Hz) halogen lamp and an EG&G Instruments 7260 DSP lock-in amplifier, a Zolix Omni λ 300 monochromator for wavelength selection, a Keithley 6517A electrometer, and HP 3478A multimeter and a red bias light source. The measurement range for this setup is from 2.1 - 0.7 eV. The red bias light is directed onto the area between two narrow coplanar aluminium strips. It leads to relatively homogeneous charge carrier generation and recombination throughout the sample, upon which the secondary charge carrier generation from the chopped light source is superimposed. This secondary generation leads to changes in the conductivity of the a-Si:H film, which is measured by applying a voltage of 100 V between the two aluminium strips and measuring the resulting current.

The resulting data can be interpreted as relative changes in absorption coefficient $\alpha(h\nu)$. The data points need to be connected to an R-T measurement to obtain absolute values for the absorption coefficient in the sub band gap range. This connection is made in the energy range around 1.8 eV.

From combined R-T and DBP measurements, disorder and defect density can be estimated. The Urbach energy E_U is a measure for the disorder in the material and indirectly also for the defect density [80]. It is determined in the energy range where α depends exponentially on the photon energy, following the relation:

$$\alpha h\nu = \alpha_0 e^{-(h\nu - E_1)/E_U} \tag{2.13}$$

where α_0 and E_1 are constants. The Urbach energy can be regarded as a measure for the width of the exponential tail state distribution in a-Si:H. Device quality material has an Urbach energy < 50 meV.

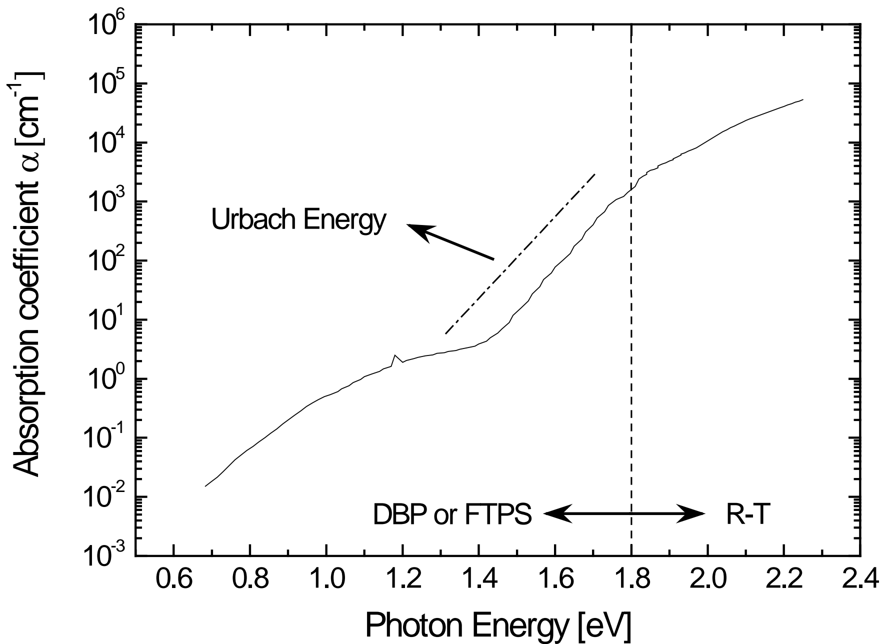

Figure 2.11 An example of an absorption spectrum, combined from an RT measurement > 1.8 eV and a DBP or FTPS spectrum < 1.8 eV.

Fourier Transform Photocurrent Spectroscopy (FTPS)

The FTPS technique is based on the photocurrent spectrum measurement using an interferometer. The technique makes use of the Michelson interferometer principle where all wavelengths of the investigated spectrum are investigated in parallel, which allows carrying out fast measurements at high accuracy. At sufficiently high conductivities of the sample measurements take just a few minutes, compared to DBP measurements that can take 45 minutes or more.

For our FTPS setup the same Thermo Electron Nicolet 5700 Fourier Transform Infrared spectrometer was adapted which is also used for FTIR measurements described above. A white 20 W tungsten light source provides the light which is modulated by the interfermeter in the setup, the measurement range is from 0.50 eV Ű- 1.95 eV. The induced photocurrent in the sample is amplified by an Keithley Model 428-PROG current preamplifier and then digitized by an analogue-to-digital converter. Like for DBP measurements, the obtained absorption spectrum is relative and needs to be connected to an R-T measurement before absolute absorption values are obtained. An example of an absorption spectrum that uses data from RT and DBP resp. FTPS measurement can be seen

in Fig. 2.11. The origin of the data above and below 1.8 eV is indicated as well as the slope that is used to determine the Urbach Energy

2.2.5 Dark Conductivity and Activation Energy

A general description for the conductivity of a material is as follows:

$$\sigma = q(\mu_n n + \mu_p p) \tag{2.14}$$

where q is the elementary charge, μ_n and μ_p the electron and hole mobility and n and p the free electron and hole concentration, respectively. Here the free charge carrier concentration are the most relevant parameters and depend on factors like the band gap, the activation energy as well as charge carrier generation from light absorption or recombination due to defect states in the band gap.

Both dark conductivity and activation energy have been determined on insulating glass substrates with a thin a-Si:H films and two coplanar aluminium contacts with a length of 20 mm and a distance of 0.5 mm between the contacts. The sample was placed on a temperature-controlled Temptronic Thermo-Chuck and a voltage of usually 10 V was applied on the contacts via a Keithley 617 electrometer. After an initial annealing phase of 30 min. at 130°C the current was measured as a function of substrate temperature in a range starting from 130°C down to 60°C. For each temperature the dark conductivity is then determined following:

$$\sigma_D = \frac{1}{R} \cdot \frac{d}{tL} = \frac{I}{V} \cdot \frac{d}{tL} \tag{2.15}$$

Here R is the resistance of the layer, d the distance between the electrodes, L the length of the electrodes and t the film thickness. R is determined from the current and voltage at each temperature following $R = V/I$. The activation energy was obtained by fitting the current-temperature relationship to:

$$\sigma_D = \sigma_0 e^{-E_a/kT} \tag{2.16}$$

with σ_0 a constant, E_a the activation energy and k Boltzmann's constant. The activation energy is a measure for the energy difference between either the Fermi level and the conduction band edge for n-type material, or alternatively between the Fermi level and the valence band edge for p-type material [15]. Although intrinsic a-Si:H was typically analyzed for this work and should have its Fermi level in the middle of the band gap, this is usually not the case, either due to unintentional oxygen doping during deposition or due to the higher mobility of electrons compared to holes in a-Si:H [81]. In either case a-Si:H behaves

slightly like an n-doped semiconductor. The dark conductivity at room temperature was extrapolated from the dark conductivity obtained between 130°C - 60°C.

2.2.6 Photoconductivity

The exposure of an a-Si:H film to light will lead to light absorption and the generation of excess free charge carriers. These excess charge carriers lead to a drastic increase in conductivity compared to the same film in the dark, as can be seen from Eq. 2.14. This conductivity under illumination, called photoconductivity, can be obtaind from simple J-V measurements.

In this work, the photoconductivity was determined under AM1.5 illumination from a He-Xe lamp in an Oriel solar simulator. Current-voltage measurements were carried out by a Hewlett Packard 4145B parameter analyzer. Sample structure was the same as for dark conductivity measurements. The voltage range was -1 to 50 V with a stepsize of 0.5 V. The conductivity was obtained from a linear fit of the J-V curve.

2.2.7 Atomic Force Microscopy (AFM)

AFM measurements were carried out with the microscope (NT-MDT) in tapping mode. The tips used in these scans were silicon cantilever tips with gold reflection coating and radii of < 10 nm. Images of the size of 2 μm $\times$ 2 μm at a resolution of 512 $\times$ 512 pixels were recorded. Tilting of the sample surface was corrected by 1st order surface background correction. In order to avoid artifacts introduced by sample drift during the measurement, only scan lines in the fast-scan direction were utilized for the analysis.

2.3 Solar Cell Characterization

2.3.1 Current-Voltage Characterization

The most basic properties of a solar cell can be obtained from simple current-voltage analysis. In this work current-voltage characterization has been carried out under AM 1.5 illumination at a power density of 1000 W/m^2. We used the same Oriel solar simulator and Hewlett Packard 4145B parameter analyzer that were also used for the photoconductivity measurements described above. The voltage range was typically -0.1 – 0.85 V with a stepsize of 0.05 V. An active area of 4 $\times$ 4 mm^2 was assumed for J-V analysis.

From the J-V measurements the external solar cell parameters were obtained. The current density at 0 V is called the short-circuit current density J_{SC}, the voltage at 0 A current the open-circuit voltage V_{OC}. The slope at these two

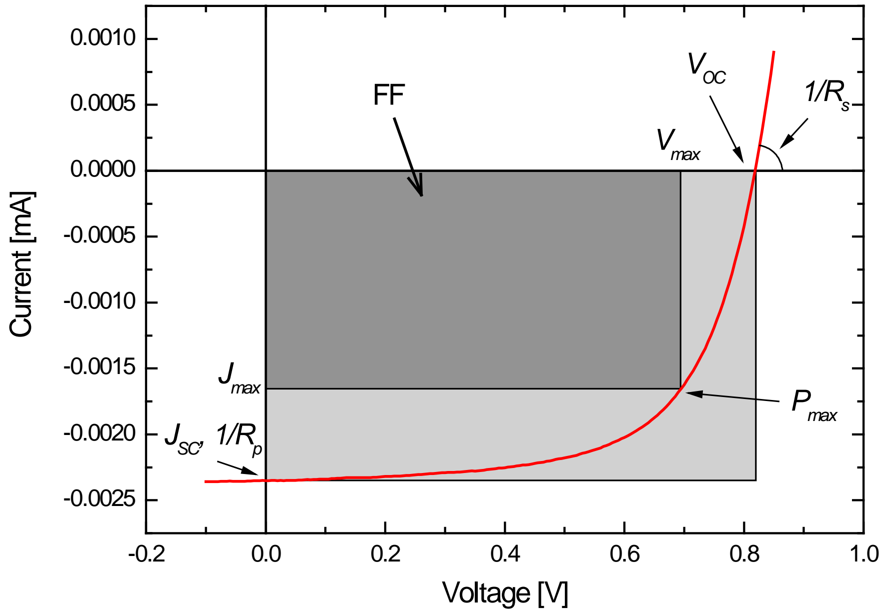

Figure 2.12 An example of a J-V measurement of an a-Si:H p-i-n solar cell. Indicated in the figure are the main parameters of a solar cell.

points determine upper limits for the parallel resistance R_p and series resistance R_s, respectively. The maximum-power point P_{max} of the cell is obtained at the point where the product of current density and voltage reach a maximum. From this point we can determine both the fill factor FF and the power conversion efficiency η. FF is determined from the ratio of $P_{max}/I_{SC}V_{OC}$ and is a measure for recombination in the solar cell, but also depends on the parasitic resistances R_p and R_s. η is determined from the ratio between P_{max} and the radiative power that illuminates the solar cell, 1000 $\mathrm{W/m^2}$ for the AM1.5 spectrum. An example of a J-V measurement of a p-i-n solar cell can be seen in Fig. 2.12, with all main solar cell parameters indicated in the figure.

2.3.2 Quantum Efficiency

The sensitivity of the solar cell to specific parts of the spectrum is determined from quantum efficiency measurements. The solar cell is illuminated by monochromatic light and the resulting photogenerated current is measured. Interference with external light is avoided by chopping the monochromatic light and measuring the photogenerated current with a lock-in amplifier. We can further

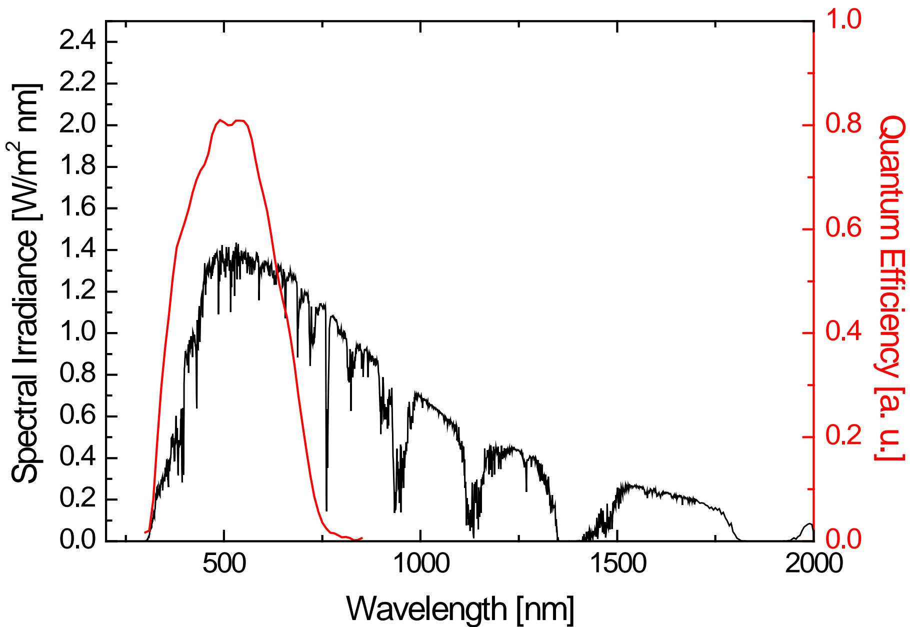

Figure 2.13 An example of a quantum efficiency measurement of a p-i-n solar cell (red solid line) compared to a large part of the AM1.5 solar irradiance spectrum (black solid line).

distinguish between internal and external quantum efficiency. The external quantum efficiency (EQE) determines the ratio of photogenerated current to photons incident on the solar cell. The internal quantum efficiency (IQE) considers losses of photons from reflection of photons on the glass surface or from passing through the solar cell without being absorbed. It will thus determine the ratio between photogenerated current and photons that have actually been absorbed in the solar cell. The IQE is always larger than the EQE. While a low IQE indicates that strong recombination occurs in the solar cell, a low EQE can indicate either that or strong light reflection on the solar cell surface as well as a too low photon absorption. In this work we only determine the EQE. The relation between photogenerated current $J_{ph}(\lambda)$, photon flux $\Phi_{ph}(\lambda)$ and EQE is given below:

$$EQE(\lambda) = \frac{J_{ph}(\lambda)}{q\Phi_{ph}(\lambda)} \tag{2.17}$$

Our spectral response measurements were carried out for a wavelength range from 300 - 850 nm with a home-built spectral response setup consisting

of an Oriel Cornerstone 130 monochromator and Oriel Apex monochromator illuminator. An example of an EQE measurement can be seen in Fig. 2.13, compared to the solar irradiance of the AM1.5 spectrum. In addition to unbiased measurements the cells could also be biased which was typically done at -1 V, in addition to unbiased measurements. At -1 V biasing the internal electric field between the p- and n-doped layers is increased by the applied external field, which ensures that practically all photogenerated charge carriers are collected at the contacts. The ratio of biased and unbiased EQE can then be used to analyze at which wavelength recombination occurs. These losses can then be attributed to the respective charge carriers [82]. Light from the blue part of the spectrum with higher photon energies is absorbed quickly due to the high $\alpha(\lambda)$ of a-Si:H in this part of the spectrum. Assuming that the light enters the cell from the p-side of the cell, holes generated close to the p-i interface have a relatively short distance to the p-layer, while electrons have to drift across the bulk of the i-layer to reach the n-layer. Thus a low ratio of $EQE(0V)/EQE(-1V)$ in the blue indicates losses of electrons before they reach the n-layer. Red light on the other hand is absorbed throughout the cell much more homogeneously. Thus a low $EQE(0\text{V})/EQE(-1\text{V})$ ratio in the red wavelength range is attributed to losses predominantly of holes before they reach the p-layer, since hole mobility is lower than electron mobility in a-Si:H [82].

Chapter 3

RF Biasing of ETP-CVD a-Si:H

3.1 Effect of RF Biasing on a-Si:H Thin Films Deposited at Different Reactor Pressures

3.1.1 Introduction

Hydrogen plays an important role in a-Si:H. It passivates dangling bonds in the a-Si:H network, reducing the defect density significantly compared to a-Si and permits the application of a-Si:H as material in, e.g., solar-cell devices. However, hydrogen is also involved in metastability mechanisms and a study of the hydrogen bonding configuration is therefore important to assess the material quality. Hydrogen bonding configuration is usually studied by Fourier transform infrared (FTIR) absorption spectroscopy. Three vibration modes of SiH_x hydrides can be observed: a wagging mode at 640 cm^{-1}, bending modes in the range of $840 - 890$ cm^{-1}, and two stretching modes at $1980 - 2030$ cm^{-1} (low stretching mode, LSM) and $2060 - 2160$ cm^{-1} (high stretching mode, HSM). The LSM absorption is attributed to mono hydrides in mono- and di-vacancies, whereas the HSM is mainly ascribed to Si-H bonds located at void surfaces [76].

From film density measurements, it was recently concluded that when the total hydrogen concentration, c_H, is above a critical value, c_{crit}, of 14 at.% the material is regarded as void-dominated and below 14 at.% as vacancy-dominated [76]. In the vacancy dominated region the integrated absorption of the LSM mode, I_{LSM}, is larger than that of the HSM mode, I_{HSM}, and vice versa in the void dominated region. Therefore, the critical hydrogen concentration, c_{crit}, can be determined as that c_H for which $I_{LSM} = I_{HSM}$. Recently, Petit [53] investigated the dependence of c_{crit} on the reactor pressure during deposition. It was shown that increasing the reactor pressure above $\sim$ 0.20 mbar leads to

a reduction of c_{crit} [53] while it remains essentially independent of pressure below 0.20 mbar. The dependence of c_{crit} on pressure was attributed to an increased contribution of ionic clusters to the growth flux at increasing pressures. The production of these clusters depends on the silane density in the plasma beam [83] and the reactor pressure can be used to increase the silane density, thus increasing cluster ion production.

Alternatively, the material structure can be related to the hydrogen solubility limit (HSL), which is generally regarded as the hydrogen concentration that can be incorporated into the amorphous network without introducing hydrogen-rich voids into the material [84]. While the HSL for a-Si, in which hydrogen was implanted, was found to be around 4%, higher hydrogen concentrations can be obtained in directly deposited a-Si:H (up to 11%) [85, 86] while maintaining a void-free structure. However, these films are considered to be thermally unstable and void formation can be observed upon annealing above 450 °C.

Ion bombardment in remote plasmas can be achieved by applying a sinusoidal RF signal to the substrate. As a result of the ion bombardment several processes can occur, like enhanced surface mobility, surface and bulk atom displacement, and sputtering at very high ion energies. Additionally, substrate biasing might also lead to breaking up of ionic clusters in the sheath region around the substrate due to interactions with the secondary plasma or upon impact on the substrate surface. Ion energies of a few electron volts are already sufficient to affect material properties [87]. Several studies on the effect of ion bombardment on a-Si:H film growth have been carried out [88–91], generally describing a densification of the films upon ion bombardment.

In this chapter, we investigate how the relationship between c_{crit} and reactor pressure is affected by RF biasing. By changing the reactor pressure the ionic cluster formation in the plasma can be varied and the influence of these clusters on the material properties can be studied. The effect of the pressure on c_{crit} was first determined for our gas-flow conditions and then the influence of the RF biasing was investigated. FTIR spectroscopy will be used to analyze the hydrogen bonding configuration.

3.1.2 Experimental Details

The ETP-CVD technique is a deposition method based on a remote plasma created in a cascaded arc and has been described in more detail elsewhere [46]. Silyl-radicals (SiH_3) are the dominant growth radical responsible for 90% of the film growth [83]. Kessels et al. [83] have detected ionic clusters with up to 10 silicon atoms, which have a detrimental effect on the material density, especially at substrate temperatures below 300°C [76]. An externally induced ion bombardment is created by applying a 13.56 MHz RF signal to the substrate.

Depending on the applied RF power a DC voltage on the substrate between 0 and 70 V can be obtained. Additionally, RF biasing generates a secondary plasma around the substrate holder.

For all depositions reported here, identical gas flows were used: 570 sccm Ar and 190 sccm H_2 in the arc, 150 sccm H_2 in the nozzle, and 230 sccm SiH_4 in the injection ring. The current in the arc is 40 A. The substrate temperature was varied between 100 and 400°C for each deposition series. The reactor pressure between the different series was varied by partially closing the valve to the roots pumps. Depositions were carried out with and without RF substrate biasing at reactor pressures of 0.18 mbar, 0.24 mbar and 0.3 mbar. For 0.3 mbar, two biased series were deposited with 14 V and 20 V, at an RF power of $\sim$ 20 W and $\sim$ 90 W, respectively. The deposition rate varied from 1.5 to 2.5 nm/s, depending on the pressure.

The a-Si:H films have been deposited on c-Si wafers (prime wafer, 500-550 μm, native oxide). From the FTIR spectra the integrated absorption of the wagging mode, and the low and high stretching mode (LSM at 2000 cm^{-1} and HSM at 2100 cm^{-1}, respectively) have been determined, from which the total hydrogen concentration, c_H, the hydrogen concentration incorporated in vacancies (LSM), c_{LSM}, and voids (HSM), c_{HSM}, respectively, is calculated [76]. The proportionality constants we used were obtained from Smets et al. [76]: $A_{640} = 1.6 \times 10^{19}$ cm^{-2} and $A_(2000) = A_{2100} = 9.1 \times 10^{19}$ cm^{-2}.

3.1.3 Results&Discussion

Fig. 3.1 shows the concentration of hydrogen obtained from LSM (left-hand side) and HSM (right-hand side) plotted versus the substrate temperature for the three pressure series (top to bottom), each with and without RF substrate biasing. For all pressures, LSM increases with biasing. Additionally, for 0.3 mbar we observe that LSM increases further for biasing at a higher voltage of 20 V. HSM is not affected by 14-V biasing for all investigated pressures, however, for 20 V we observe a decrease of HSM by 2-3% at temperatures below 300 °C. For increasing reactor pressures, c_{LSM} shifts to lower concentrations at all temperatures, while c_{HSM} shifts up slightly and mainly at low temperatures.

In Fig. 3.2 both c_{LSM} and c_{HSM} have been plotted versus the total hydrogen concentration, c_H, for the seven different depositions series. In this figure c_{crit} is marked with vertical lines. The graphs on the left-hand side show the three unbiased series. While c_{crit} does not change much when increasing the reactor pressure from 0.18 to 0.24 mbar (around 14% for both pressures), there is a substantial change when the pressure is increased further to 0.3 mbar. In the latter case we observe a shift of c_{crit} from 14% down to 9.5%, mainly due to an absolute drop of c_{LSM} by roughly 3%, but also a slight shift of the c_{HSM} to higher concentrations. These changes are observed mainly at higher total hy-

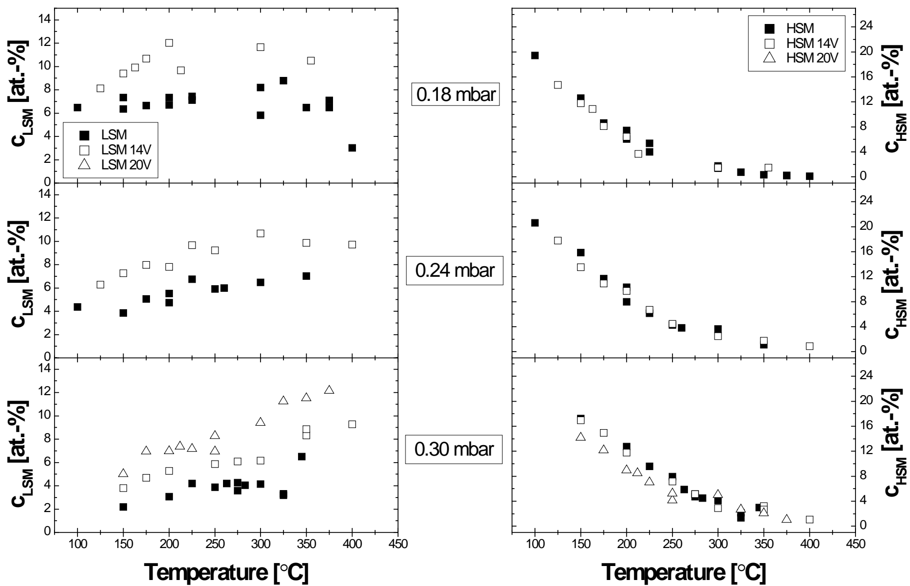

Figure 3.1 c_{LSM} and c_{HSM} for different substrate temperatures of all seven series. Full symbols are from unbiased and empty symbols from biased depositions.

drogen concentrations (which corresponds to deposition at low temperatures). Petit [53] observed a stronger dependence of c_{crit} on the reactor pressure, with a drop from 14% to 7% when increasing the pressure from 0.23 mbar to 0.25 mbar. However, her depositions were carried out at higher growth rates (3.2 to 6 nm/s compared to 1.5 to 2.5 nm/s for our series). An increased contribution of cluster ions to the growth flux can explain both the drop of c_{crit} with increasing reactor pressure and the stronger dependence of c_{crit} on reactor pressure at higher growth rates. With increasing pressure, the beam diameter is reduced, the silane density increased and thus the probability of ion-molecule (i.e. silane) interaction increases. Since ion-molecule reactions in the plasma occurs at near-collision rates, the increased interaction probability results in more and larger cluster ions formed in the beam [46,92]. For the same reason, more ionic cluster formation occurs at high growth rates, corresponding to higher gas flows of the growth precursor. These cluster ions and dust particles have higher sticking coefficients than SiH_3 radicals and contribution of these ionic clusters to the growth flux can result in poor material quality [93].

A similar trend can be observed for the depositions biased with 14 V as shown on the right-hand side of Fig. 3.2. When increasing the pressure from 0.18 mbar to 0.24 mbar, c_{crit} changes slightly from 15.5% to 14.5%. At 0.3 mbar,

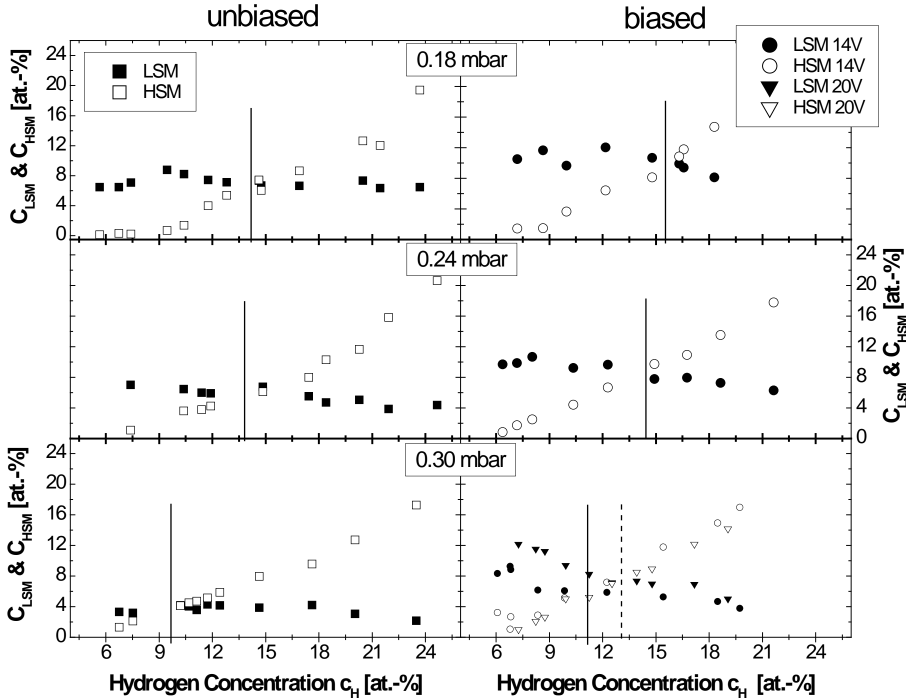

Figure 3.2 Plot of c_{LSM} and c_{HSM} versus c_H for the seven different series. The critical hydrogen concentration is marked by the vertical solid lines for 14-V biasing, and by the vertical dashed line for 20-V biasing.

a c_{crit} of 11% is found, which again we can attribute mainly to a decrease of c_{LSM} by approximately 3%. So for both biased and unbiased depositions, c_{crit} mainly changes due to lower c_{LSM}, corresponding to less hydrogen in vacancies, while the c_{HSM} remains largely unaffected. Compared with the unbiased series, biasing at 14 V hardly affects c_{crit}.

As shown above, we do not see a significant change in c_{crit} at 14 V biasing for the series at 0.3 mbar. However, at 20 V biasing we find a c_{crit} of 13% (dotted line), which is close to the 14% we obtain for the depositions at lower pressure. This high value for c_{crit} is due to an increase in LSM and a decrease in HSM. The increase in LSM and the decrease in HSM can result from several effects. One possibility is that the increase in ion energy as result of the increase of bias voltage leads to more energy provided to substrate surface from bombarding ions. As will be discussed in more detail in Chapter 4, surface processes induced by ion bombardment can play an important role in growing dense, void-free films. Another possible mechanisms leading to denser films is related to a

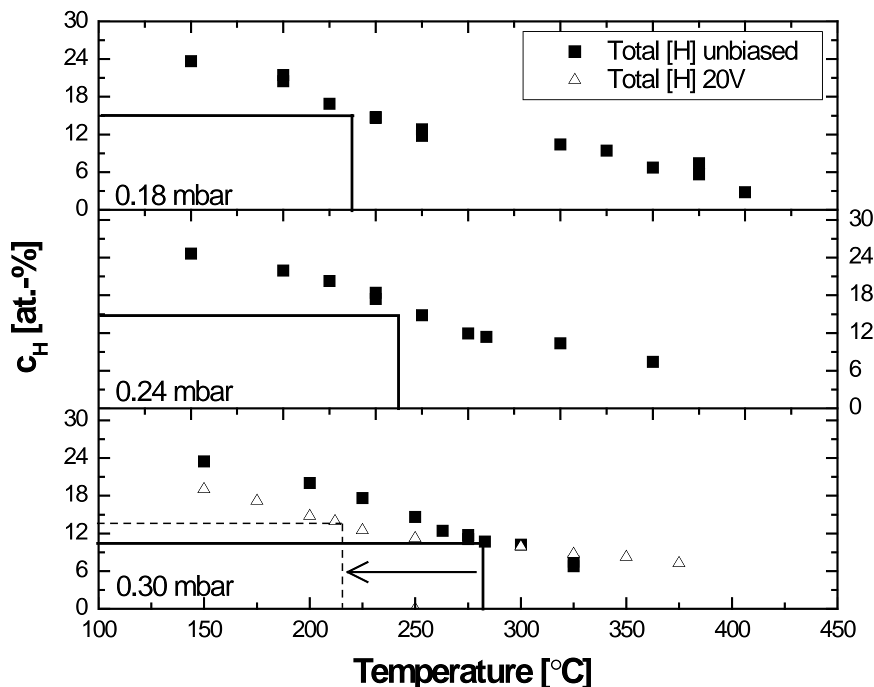

Figure 3.3 The total hydrogen concentration versus the substrate temperature for all series. Full symbols are from unbiased and empty symbols from biased depositions. The solid lines indicate the substrate temperature at which the critical hydrogen concentration is obtained, the dashed line does the same for the series at 0.3 mbar reactor pressure and 20 V substrate biasing.

reduced incorporation of cluster ions into the film. Cluster ions might break up upon impact on the surface, or cluster ions might break up in the secondary plasma around the substrate holder. The reduced cluster incorporation is not necessarily a result of the increased substrate voltage alone, also a higher ion current at increased RF power might contribute as it increases the ion-radical flux ratio and thus the energy per deposited cluster molecule. The ion-energy distribution of RF biasing is broad and bimodal [50], which complicates the interpretation of the observed trends further as both high and low energy ions are present in the plasma.

Fig. 3.3 shows the total hydrogen concentration, c_H, at different substrate temperatures. The typical decrease in c_H with increasing temperature can be seen for all series. An increase in pressure leads to an increased c_H for temperatures below 350°C, while virtually no changes can be observed above 350°C. The solid lines indicate the temperature, T(c_{crit}), at which c_{crit} is obtained

from the unbiased samples in Fig. 3.2. Above this T(c_{crit}), vacancy dominated material is obtained, whereas the material is void dominated material below $T(c_{crit})$. $T(c_{crit})$ shifts to higher temperatures with increasing reactor pressure, which demonstrates how the temperature range in which we obtain vacancy-dominated material is reduced with increasing reactor pressures, thus reducing the range in which solar-grade material can be obtained. The dashed line in the lowest graph in Fig. 3.3 indicates $T(c_{crit})$ for the series biased with 20 V at 0.3 mbar reactor pressure. We can clearly see how, due to the increased c_{crit} and the reduced hydrogen concentration at lower temperatures, $T(c_{crit})$ is shifted downwards, thus increasing the temperature range in which vacancy-dominated material can be obtained.

3.1.4 Conclusions

The influence of RF substrate biasing on the relationship between the critical hydrogen concentration c_{crit} and the reactor pressure has been investigated. An increase in reactor pressure leads to a decrease in c_{crit}, mainly above 0.24 mbar, which is attributed to an increased contribution of cluster ions and polymers to the growth flux. Ion bombardment at 14 V has hardly an effect on c_{crit}, yet an increase in LSM could be observed for all temperatures and pressures. Ion bombardment at 20 V for the high pressure series resulted in an increase of c_{crit} from 9% unbiased to 13% biased, along with a decrease of HSM and an increase of LSM. This is attributed to a reduced incorporation of ionic clusters and polymers into the film. A dependence of hydrogen solubility on reactor pressure and substrate biasing could be observed, but the thermal stability of these films has not been investigated.

Chapter 4

Pulse-Shaped Biasing as a New Tool to Control the Ion Energy Distribution Function in a-Si:H Film Growth in ETP-CVD

4.1 Introduction

Hydrogenated amorphous silicon (a-Si:H) is an increasingly important material for application in devices such as thin film transistors [94] and thin film solar cells [14]. While the most common method for deposition of a-Si:H is parallel-plate radio frequency-plasma enhanced chemical vapor deposition (RF-PECVD), there are numerous other deposition techniques available today, like very high-frequency (VHF) PECVD, hot-wire CVD (HW-CVD), or expanding thermal plasma CVD (ETP-CVD) used in this work. As in all plasma-based deposition techniques, also in ETP-CVD the film growth of a-Si:H is a result of predominantly SiH_3 radicals forming in the plasma and reacting with the substrate surface [95]. All plasma-based techniques have a complex surface chemistry in common, involving interaction between growth radicals, gas molecules, different types of ions and the substrate surface itself. The interaction of these reactive species with the surface at given gas pressure and substrate temperature determine the quality of the final bulk film. Understanding these processes is crucial to optimize deposition conditions and obtain the optimal material for the required applications.

While the effect of different gas flows, pressure, substrate temperature

and other parameters are well understood for CVD techniques in general and also for ETP-CVD technique [46], knowledge about the effect of ion bombardment is still comparatively poor for a-Si:H thin-film growth. In recent studies it was shown that ion bombardment offers additional control over film growth, with promising results demonstrating dense films at deposition conditions usually resulting in void-rich low-density material [48, 52, 54, 90, 91, 96–101]. It is therefore of great technological importance to understand the effect of ion bombardment on a-Si:H film growth, not only for the ETP-CVD technique but for any kind of plasma-involving CVD in general.

The type of interaction between bombarding ions and the a-Si:H film depends mostly on the amount of energy transferred from impinging ions to substrate surface or, at higher energies, subsurface layers. Important parameters to determine the type of interaction are the ion energy, ion flux, the mass ratio between bombarding ion and the target atom, the ion/atom arrival ratio and the average energy provided by ions per deposited Si atom. Achieving control over these parameters is crucial in order to study ion-surface interaction systematically. Control over all three parameters is given in a secondary ion source like e. g. an ion gun, which gives control over ion flux, ion energy and the type of ion created. Drawbacks of ion guns are their limitation to lower ion currents and low pressures for operation as well as their higher cost. In the approach discussed in this chapter, a secondary ion source is not required and only the ions naturally present in the plasma are accelerated towards the substrate surface, excluding the risk of disturbing the plasma chemistry by the energetic secondary ions. Utilizing a special type of substrate biasing, called pulse-shaped biasing (PSB), control over the ion-energy distribution function (IEDF) is obtained [54], resulting in a narrow distribution with a peak position that can be controlled over a wide energy range, in our case up to 200 eV. With control over the IEDF, we are able to attribute changes in material properties to certain ion energies and relate those energies to ion-surface atom and ion-bulk atom interactions. The PSB has no significant effect on the plasma chemistry [48] and thus in addition to the common processing parameters (e. g. substrate temperature, gas flows) two additional, independent parameters are obtained: the average energy of ions determined by the substrate voltage, as well as the ion current determined by the shape of the waveform.

This paper is organized as follows. In the experimental section we describe briefly the ETP CVD technique and the pulse-shaped biasing. We then present the results, which is split into two parts. In the first part we will demonstrate the principle of PSB. We will show how PSB results in a narrow and controllable IEDF, and how different types of substrates can result in the loss of this control if not addressed properly. In the second part we will show results of a-Si:H thin films deposited with PSB. We will discuss the results in terms of

ion - thin film interaction and determine an energy range for bombarding ions ideal to obtain dense and void-free a-Si:H deposition.

4.2 Analysis of Pulse-Shaped Biasing as a Tool to Control the Ion Energy Distribution

4.2.1 Experimental Details

The deposition method used in this work, the ETP-CVD technique, is a remote plasma technique. A schematic representation is shown in Fig. 4.1. The technique has been described in detail elsewhere [46]. In brief, an Ar-H_2 plasma is ignited and sustained in a cascaded arc at pressures around 0.46 bar. The plasma expands supersonically through a nozzle into a low pressure deposition chamber ($\sim$ 0.14 mbar). The nozzle also serves as an additional injection point for H_2 gas. The SiH_4 gas is injected into the Ar-H_2 plasma through an injection ring $\sim$ 10 cm below the nozzle and subsequently dissociates predominantly into SiH_3. These radicals are transported to the temperature controlled substrate holder where the a-Si:H film is deposited.

For all depositions the gas flows were 570 sccm Ar and 190 sccm H_2 in the arc, 150 sccm H_2 in the nozzle and 230 sccm SiH_4 in the injection ring, at a current of 40 A in the arc. Due to interference between the applied voltage and the thermocouple located in the chuck the thermocouple had to be disconnected during biased depositions, impeding active temperature control during depositions. To accommodate for this restriction, the samples were heated up to 210°C prior to deposition before the thermocouple was disconnected. During deposition the sample cooled down to about 185°C. Deposition time was 6.15 minutes for all depositions. The deposition rate was about of 0.8 nm/s for unbiased and up to 1 nm/s for biased depositions.

For a remote plasma like the ETP, ions are accelerated to the substrate only by the induced substrate self-bias, for the ETP typically < 2 V [46]. Without substrate biasing this leads to negligible ion energy compared to the applied voltages of up to 200 V in this study. Therefore the ETP-CVD technique is a very suitable system to study the effect of controlled ion bombardment on film growth.

The pulse-shaped biasing setup has been designed similar to the setup described by Wang et al. [54] and has been adapted to our ETP reactor. The whole setup can be seen in Fig. 4.1. The non-sinusoidal waveform is created by an arbitrary waveform generator (Agilent 33250A) and a broadband amplifier (Amplifier Research 150A250) with an amplification range from 10 kHz up to 250 MHz. The amplifier is connected via a 1 nF blocking capacitor to the chuck where either the substrate holder or the retarding field energy analyzer (RFEA)

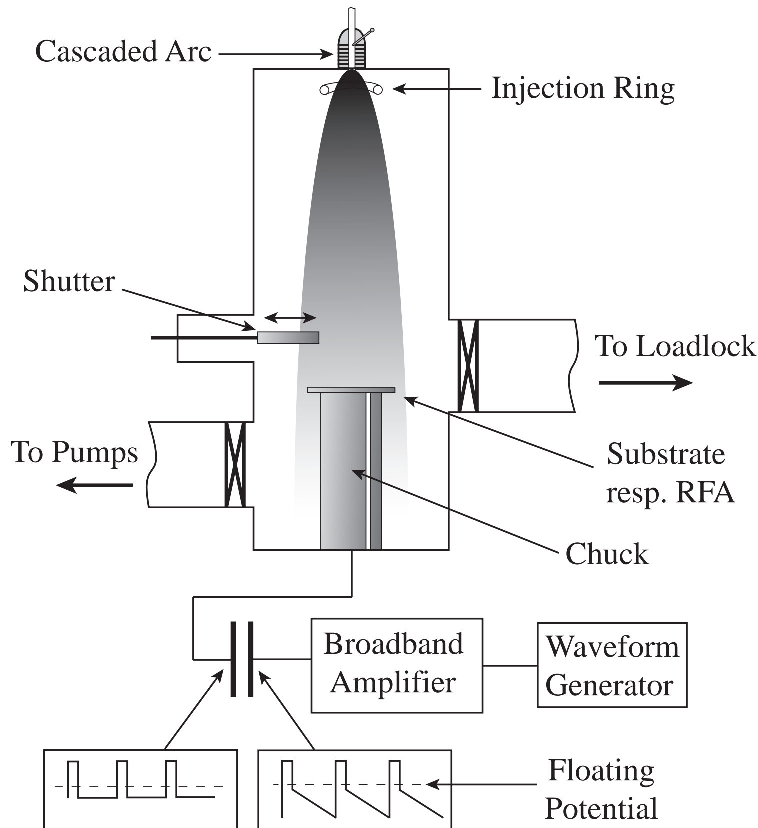

Figure 4.1 Schematic drawing of the ETP-CVD setup and the connected PSB setup.

unit are located. In principle, this setup enables us to operate in a frequency range for the non-sinusoidal wave from 10 kHz up to 8 MHz, but in this work a frequency of 100 kHz was used for all depositions, resulting in a period of 10 μs, unless noted otherwise.

The general idea of pulse-shaped biasing is that by coupling a specially tailored waveform to the substrate via a blocking capacitor, a constant negative potential can be obtained on the sample holder for most part of one period, T, of the waveform. This results in a very narrow ion energy distribution function (IEDF) contrary to the broad and bimodal IEDF obtained with RF biasing [54], assuming the sheath transit time is much shorter than the duration of the period with constant potential [101]. A schematic version of the waveform at the amplifier output can be seen in Fig. 4.2a and on the substrate surface in Fig. 4.2b. Each period of the amplifier output consists of a ramp with a negative slope

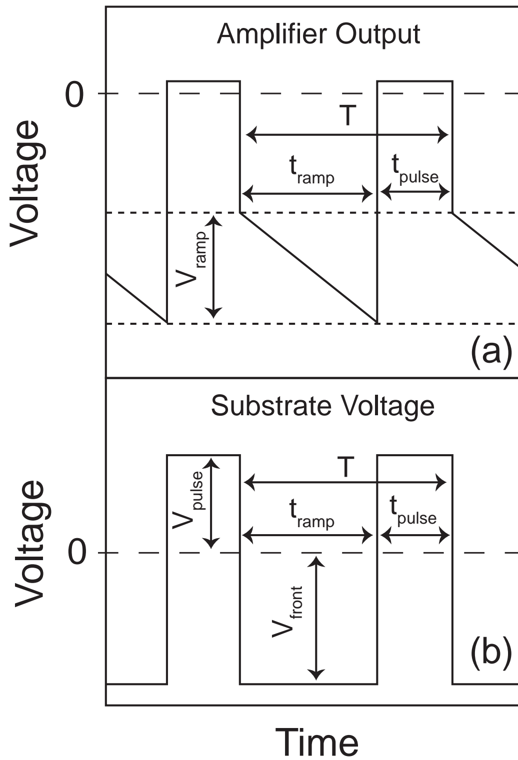

Figure 4.2 Schematic versions of the applied pulse-shaped waveform (a) at the broadband amplifier output and (b) on the substrate surface. Important characteristics of the waveforms are indicated in the figure.

followed by a discharge pulse. During the ramp part of the waveform, positive charge carriers are accelerated towards the substrate holder due to the potential difference, and charge is accumulated on the substrate holder due to the blocking capacitor. The negative slope, V_{slope}, in the output signal of the amplifier is tuned in such a way that it exactly balances this charge built-up. As a result we obtain a constant negative potential V_{front} on the substrate surface during the ramp. The pulses are necessary to discharge this built-up charge regularly, allowing negative charge carriers to reach the substrate surface, which occurs at voltages above the floating potential, for ETP technique around $>$ -2 V as explained above. The result is a constant negative potential between the discharge pulses. Important features in this waveform are the potential drop during the ramp, V_{slope}, the duration of the ramp, t_{ramp}, the potential during the discharge pulse, V_{pulse}, the duration of the pulse, t_{pulse}, and the average negative potential obtained during the ramp on the substrate surface. This last parameter has been

measured in two ways: indirectly by means of a voltage probe on the substrate side of the blocking capacitor (V_{aC}), or directly on the substrate surface, in our case with a Tektronix 1/100 passive voltage probe (V_{front}). Ideally these two voltages are identical, but for a non-conductive substrate they can be significantly different, as will be discussed below. In the following, we will use the term V_{front} in general, and only distinguish between these two methods where required. As V_{front} is much larger than the plasma potential, V_{front} determines the average energy of the ions entering the sheath region. In all our experiments with a period of $T = 10\mu$s the duration of pulse and ramp were t_{pulse} = 2.5 μs and t_{ramp} = 7.5 μs, respectively. The ratio between t_{pulse} and t_{ramp} allows controlling the substrate current, however in this work the ratio was constant for all depositions. The substrate current density J_s during the ramp was measured by means of a square tungsten probe, which was placed on the substrate holder and scanned in the voltage range from 0 to 200 V. For more details on the voltage and current measurement we refer to Ref. [102]. It should be noted that a weak secondary plasma was visible around the substrate holder during biased depositions.

Time-averaged measurements of the IEDF have been carried out with a commercial planar gridded RFEA (Semion System). More information on the RFEA can be found in Ref. [102] and Ref. [49]. As the measurement range of the RFEA unit is limited to 150 V, IEDF measurements were limited to $V_{front} <$ 100 V to ensure that the whole width of the IEDF peaks can be acquired.

4.2.2 Results & Discussion

As explained above, the voltage on the substrate surface has been measured in two different ways: directly on the substrate surface (V_{front}) and on the substrate side of the blocking capacitor (V_{aC}). Both are plotted along with the output of the broadband amplifier (V_{bC}) for different substrates in Fig. 4.3. Three different types of substrates have been used: conductive substrate (a), non-conductive substrate (b) and non-conductive substrate with TCO layer (c). In this case the plasma was a non-depositing Ar-H_2 plasma with 710 sccm Ar and 190 sccm H_2 in the arc and 150 sccm H_2 in the nozzle. This type of plasma has a higher substrate current density J_s compared to a depositing Ar-H_2-SiH_4 plasma as a result of the higher ion density in this type of plasma [38]. Due to faster charging of the substrate under these conditions, a frequency of 125 kHz was required to maintain a flat V_{front} during measurements (alternatively V_{ramp} could have been increased). For a conductive substrate in Fig. 4.3a, we clearly see the ramp in the output of the amplifier, V_{bC}, and the resulting flat potential between pulses for both V_{front} and V_{aC}. The overlap between V_{front} and V_{aC} demonstrates that for a conductive substrate V_{aC} accurately represents the potential on the substrate surface. This allows measuring the substrate voltage

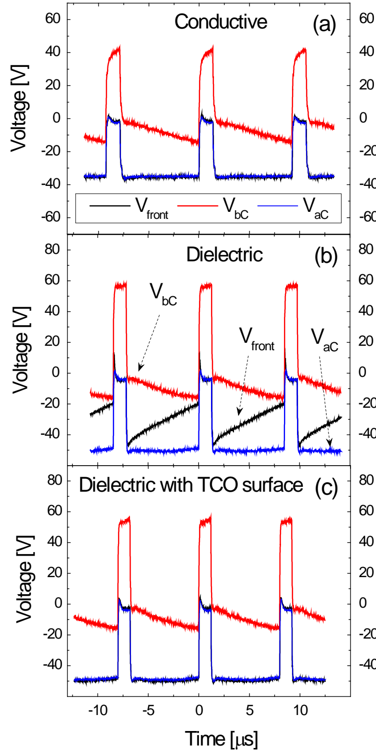

Figure 4.3 Measured voltages during PSB deposition in an Ar-H_2 plasma on the substrate surface (V_{front}), on the amplifier side of the blocking capacitor (V_{bC}) and on the substrate side of the blocking capacitor (V_{aC}). All three voltages are shown for (a) conductive substrate, (b) non-conductive substrate and (c) non-conductive substrate with a thin, conductive TCO surface layer.

outside of the deposition reactor and directly on the blocking capacitor, without the need to have a voltage probe on the substrate surface during deposition. For a non-conductive substrate, however, V_{aC} is clearly different from V_{front} as can be seen in Fig. 4.3b. The non-conductive substrate acts as a separate capacitor on the floating chuck, leading to a stronger charge built-up on the substrate surface than on the rest of the substrate holder. Consequently, while V_{aC} measures the whole voltage drop over chuck and substrate surface and appears to be flat during the ramp, the surface potential actually behaves quite differently. V_{front} clearly shows a positive slope between the pulses, which is a result of the faster charge built-up on the surface. The constant increase in V_{front} will lead to a much broader IEDF [102]. In case of a non-conductive substrate, V_{aC} can thus not always be used to tune the output waveform and a voltage probe must

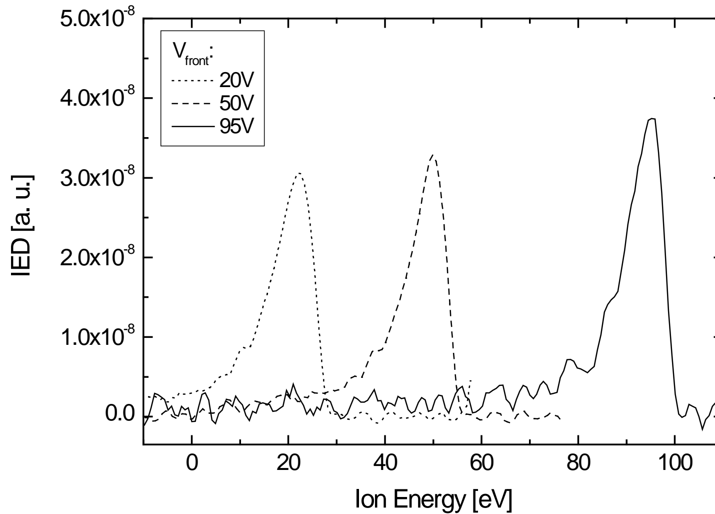

Figure 4.4 Ion energy distribution measurements in an Ar-H_2 plasma for surface voltages of 20 V (dotted line), 50 V (dashed line) and 95 V (solid line).

be used. However, if we have a conductive film on the substrate surface (in this case TCO), we return to the situation of a conductive substrate, as can be seen in Fig. 4.3c. In this case the substrate surface was connected to the chuck through the same electrically conductive clamps and screws that are commonly used in this setup. In this setup V_{aC} represents V_{front} accurately again and the two curves overlap so well that they can hardly be distinguished in the figure. We have demonstrated that the presence of a non-conductive substrate is only problematic if a dielectric material is deposited. For the deposition of a conductive material, e. g. a-Si:H in our case, V_{aC} is inaccurate only in the initial phase of the deposition, but will give a very good representation of V_{front} as soon as a closed conductive film is formed. Ion bombardment will thus be accurately controlled for the bulk of the film deposition.

Measurements of the ion energy distribution function can be seen in Fig. 4.4 for three different substrate voltages V_{front}: 20 V, 50 V and 95 V. The peak position corresponds well to the applied voltage for all three measurements, demonstrating the control achieved over the IEDF. We observe broadening of the peaks which can be separated into two components: a broadening symmetric around the peak position and an additional shoulder at the low-energy side of the peaks. The symmetric broadening around the peak center shows an FWHM of about 6.9 eV, 6.6 eV and 6.2 eV for 20 V, 50 V and 95 V respectively. The FWHM was determined on the high-energy side of the peak and

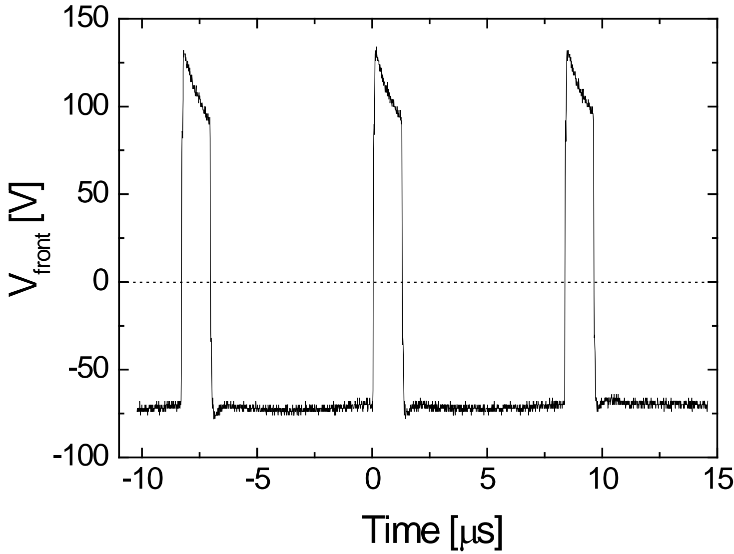

Figure 4.5 Measurement of V_{front} for an Ar-H_2-SiH_4 plasma, the dotted line marks the 0 V - potential.

then doubled, to avoid an overestimation due to the low-energy shoulder. This symmetric broadening is a result of noise in the broadband amplifier output signal, which leads to small, continuous variations of the voltage during the ramp. The importance of waveform instabilities for IEDF broadening is discussed in detail in Ref. [102]. The additional low-energy shoulder is a result of collisions of ions in the sheath region, leading to scattering losses. Following the collisionless Child law [39], an increase in substrate voltage leads to an increase in sheath thickness, s. The mean free path, λ_{mfp}, is independent of the substrate voltage, consequently the number of average collision events per ion, s/λ_{mfp}, increases, resulting in an increase in scattering loss with increasing V_{front} and thus a broader low energy shoulder [103].

In Fig. 4.5 V_{front} is shown for a conductive substrate in an Ar-H_2-SiH_4 plasma. While in the Ar-H_2 plasma V_{pulse} was only slightly above the floating potential, here V_{pulse} exceeds 100 V. This is related to the current balance that automatically establishes in the system as a result of the blocking capacitor. In general the built-up of charge due to the current of positive charge carriers during the ramp is exactly balanced by the current of negative charge carriers during the pulse. In case of an Ar-H_2 plasma the ion current is carried predominantly by positive H_3^+ ions [104] and during the pulse free electrons are the dominant charge carriers. In both cases the current is a function of the density

of the charge carrier, its respective mobility and the potential difference between plasma and substrate. Due to the much higher mobility of the electrons compared to ions, and assuming a similar carrier density, the short pulse duration at a voltage just above the floating potential is sufficient to compensate completely for the charge built-up during the ramp [105]. In case of an Ar-H_2-SiH_4 plasma, the pulse voltage of around 100 V suggests a change in composition of negative species in the plasma with lower mobility and lower concentration. This indicates the strong presence of negatively charged ions or particles in the plasma, with a much lower mobility compared to free electrons. In order to maintain a balance between the two currents a voltage offset occurs, leading to the large positive voltage during the pulse, which is necessary to get sufficient negative ions to the substrate surface to compensate fully for the charge on the substrate built-up during the ramp.

A substantial presence of negative ions/particles in the plasma also has an effect on the IEDF using different biasing techniques like RF biasing. Since a considerable part of the voltage would be positive, alternating bombardment with positively and negatively charged ions would occur, instead of the expected bombardment with predominantly positive ions. Furthermore the presence of negative ions/particles leads to a much higher RF power required to obtain the same average substrate voltage V_{dc} as compared to conditions without negative ions/particles in the plasma, which will also result in a much broader IEDF. In case of heavier molecules or dust particles the impact on the substrate surface could result in their break-up. To avoid the large positive voltage during the ramp, the duration t_{pulse} can be increased, giving negative species more time to discharge the substrate during the pulse. Alternatively PSB could be adjusted to achieve control also about the bombardment with negative ions on the substrate surface. Introducing a slope to the pulse similar to the slope of the ramp during negative voltages would allow gaining control also over the energy of negative ions. Ideally this could be used twofold: to break up larger negative ionic clusters upon impact on the surface during the pulse, and to provide the surface with additional energy from controlled ion bombardment during the ramp.

Fig. 4.6 shows the growth flux, the ion flux and the resulting average energy deposited per incorporated Si atom, eV/Si atom, as a function of substrate voltage. The Clausius-Mossotti relation was used to determine the mass density $\rho_{a-Si:H}$ of the films from the IR refractive index and the total hydrogen content c_H [76]. The growth flux Γ_{Si} was determined from the mass density. The ion flux during the ramp Γ_{ion} was directly determined from the substrate current density J_s by means of a square tungsten probe. Both fluxes continuously increase with V_{front}. This indicates that substrate biasing has a clear effect on the gas phase, leading to additional SiH_3 production in the plasma and therefore an increase

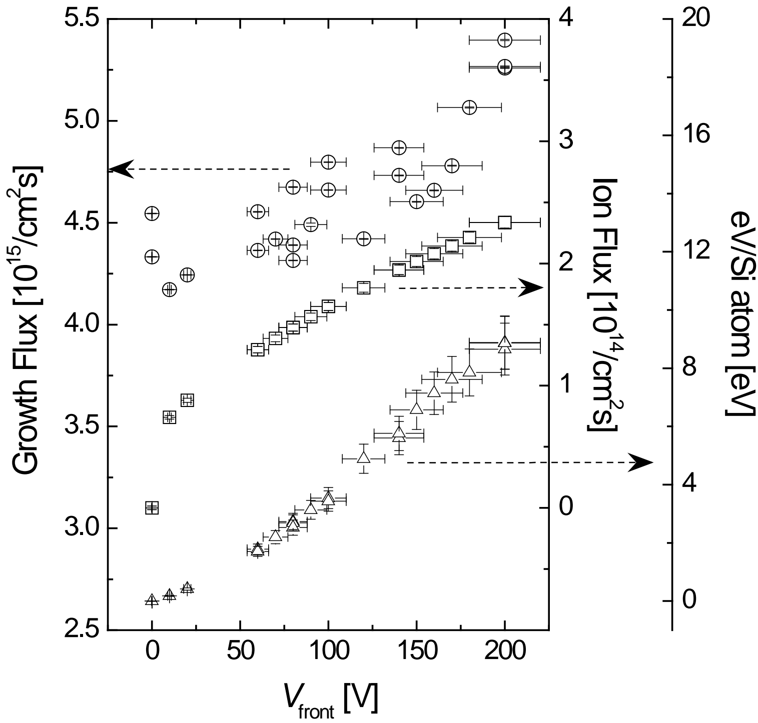

Figure 4.6 Growth flux Γ_{Si}, ion flux Γ_{ion} and energy deposited per incorporated Si atom vs. the surface voltage V_{front}.

in growth flux . An increase in SiH_3 production has been observed in previous studies for RF biasing [52, 106] and attributed to additional gas-phase reactions in the secondary plasma around the substrate holder. It was not observed in a recent study on pulse-shaped biasing by Martin et al. [48], however, they assumed a constant mass density of 2.25 g/cm^3 and constant IR refractive index for all samples, while we include changes in both mass density and IR refractive index in our analysis via the Clausius-Mossotti relation. The increase in growth flux could also be partly related to the presence of negatively charged ions, as shown above. During biased deposition the large positive voltage during the discharge pulse could lead to their partial break-up and subsequent incorporation into the film. The increase in ion flux is related to both the ionization in the secondary plasma as well as the increase in ion current with increasing V_{front} due to an increase in sheath thickness s and thus collection area around the substrate holder as mentioned above [107].

The ratio between the two fluxes times the average substrate voltage de-

termines the average energy deposited per incorporated Si atom. Also for the average deposited energy we observe an increase with increasing V_{front}, which is a result of the stronger increase in Γ_{ion} compared to Γ_{Si} (∼160% relative increase of Γ_{ion} compared to ∼25% for Γ_{Si}, respectively). The following discussion of material properties below will be in terms of deposited energy per Si atom for an easier comparison with results published in literature. It should be noted that the error for the substrate voltage given in Fig. 4.6 overestimates the actual voltage noise during the ramp. The step size of the volt meter increases with the measured voltage range, resulting in a decreasing resolution. This also leads to an overestimation in the error of the deposited energy.

4.3 Effect of Ion Bombardment with a Narrow Ion Energy Distribution on a-Si:H Film Growth and Material Properties

4.3.1 Experimental Details

The a-Si:H thin films have been deposited on c-Si wafers (prime wafer, 500-550 μm) with ∼ 2 nm native oxide for in-situ real-time spectroscopic ellipsometry (RTSE) measurements (J. A. Woollam Co., Inc M-2000F rotating compensator spectroscopic ellipsometer) and Fourier transform infrared spectroscopy (FTIR) analysis (Nicolet 5700, Thermo Electron Corp.). From FTIR spectra the integrated absorption of the wagging mode (at 640 cm^{-1}), the low stretching mode (LSM at 2000 cm^{-1}) and high stretching mode (HSM at 2100 cm^{-1}) have been determined, from which the total hydrogen concentration, c_H, the hydrogen concentration incorporated in vacancies, c_{LSM}, and nanovoids, c_{HSM}, respectively, is calculated. Our in situ RTSE measurements were performed using a J. A. Woollam Co., Inc M-2000F spectroscopic ellipsometer. In our RTSE data analysis we follow a procedure that was described in detail by Van den Oever et al. [63]. The actual data obtained in an RTSE measurement is the change of the polarization state of the incident light beam, defined by the ellipsometric angles Ψ and Δ, as a function of wavelength. Actual physical information like film thickness and surface roughness are obtained after fitting the ellipsometric angles, in our case with EASE 2.13 software by J. A. Woollam Co. The a-Si:H dielectric function is obtained from the Tauc-Lorentz parameterization. The only dynamic fitting parameters are the bulk film thickness d_b and the surface roughness d_s.

For optical measurements samples were deposited on Corning 7059 glass with coplanar Al contacts to determine optical constants, band gap, and Urbach energy. For reflection-transmission measurements our spectrometer setup

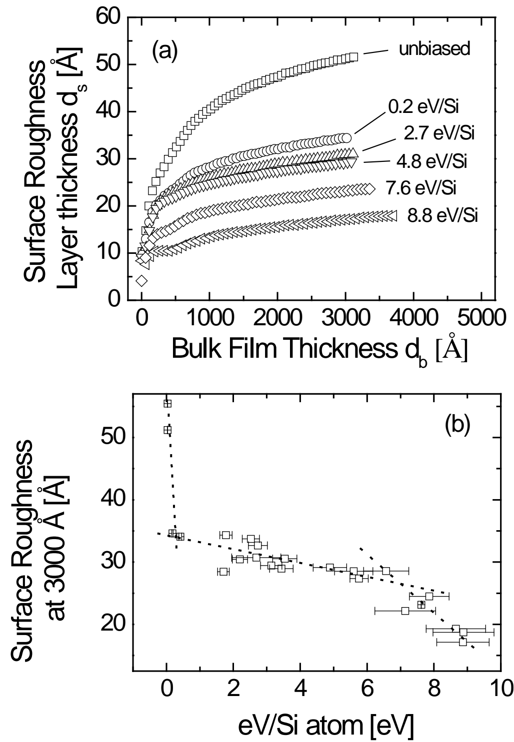

Figure 4.7 (a) The surface roughness layer thickness ds as a function of the bulk film thickness db for different deposited energies per Si atom. (b) The surface roughness layer thickness ds at a bulk film thickness of 3000 ? vs. the energy deposited per Si atom.

consisted of a halogen lamp and a SPEX 1680B monochromator. The Urbach energy was determined from combined reflection-transmission measurements and dual-beam photoconductivity (DBP) measurements.

It is worth noting that for $V_{front} > 180$ V several samples showed peeling from the substrate surface for both glass and silicon wafers. This indicates significant stress induced at these voltages, e. g. due to thermal gradients induced by local surface heating from ion bombardment, or incorporation of Ar ions into the film [108].

4.3.2 Results & Discussion

The predominant part of the energy deposited during ion bombardment remains in the surface layer of the film, as the stopping power for Ar ions bom-

barding on a silicon surface is around 270 eV/nm [109]. We therefore examine the development of the surface roughness d_s versus bulk film thickness d_b, as determined from in-situ RTSE as a function of the deposited energy up to 9 eV/Si atom. The surface roughness development as a function of bulk-layer thickness is shown in Fig. 4.7a. The roughest films are obtained for unbiased depositions with a surface roughness layer thickness of about 50 Å at 3000 Å bulk film thickness. A strong reduction of d_s is observed already upon mild ion bombardment around 0.2 eV/Si; a further increase in V_{front} leads to even smoother surfaces. At 8.8 eV/Si atom very smooth films below 20 Åd_s are grown, otherwise typically obtained in our ETP-CVD reactor only at growth rates around 1 Å/s or at higher substrate temperatures [110]. Since all depositions had the same deposition time of 6.15 minutes we can also observe the increase in deposition rate above 4.8 eV/Si atom, which can be concluded from the increase in final bulk film thickness. The surface roughness at 3000 Å bulk film thickness as a function of deposited energy per Si atom can be seen in Fig. 4.7b. Three different regions can be distinguished. Already at very low deposited energies < 1 eV/Si atom d_s at 3000 Å strongly decreases with substrate voltage. The decrease in d_s between 1 and 4.8 eV/Si atom is much weaker, and becomes larger above 4.8 eV/Si atom. The three areas are indicated in the plot by dotted lines. From the roughness layer development it is clear that an increase in deposited energy leads to smoother surfaces.

FTIR results can be seen in Fig 4.8a and 4.8b. Figure 4.8a shows the dependence of the total hydrogen concentration c_H and Fig. 4.8b the dependence of the LSM mode associated with divacancies, c_{LSM}, and HSM mode associated with nanovoids, c_{HSM}, on the deposited energy per Si atom. The data in Fig. 4.8a show some scattering, but in general the hydrogen concentration increases continuously with eV/Si atom. The same observation can be made in Fig. 4.8b for divacancies. The increase appears to be stronger for voltages < 4.8 eV/Si atom and weaker for > 4.8 eV/Si atom. The absorption due to nanovoids (HSM) continuously decreases until for > 4.8 eV/Si atom it could not be determined anymore. This important transition voltage has been marked in Fig. 4.8b with a dashed line and the regions below and above 4.8 eV/Si atom are labeled region I and II, respectively.

The infrared (IR) refractive index as a function of eV/Si atom is shown in Fig. 4.9a and shows a similar separation into two regions. Below 4.8 eV/Si atom in region I the refractive index continuously increases, indicating an increase in material density. This is in good agreement with the reduction in void content deduced from c_{HSM} in Fig. 4.8b. In region II (> 4.8 eV/Si atom) the refractive index is constant and does not change with deposited energy, which is also in agreement with the constant c_{HSM} in region II. The clear relation between void concentration and IR refractive index indicates that for our experimental

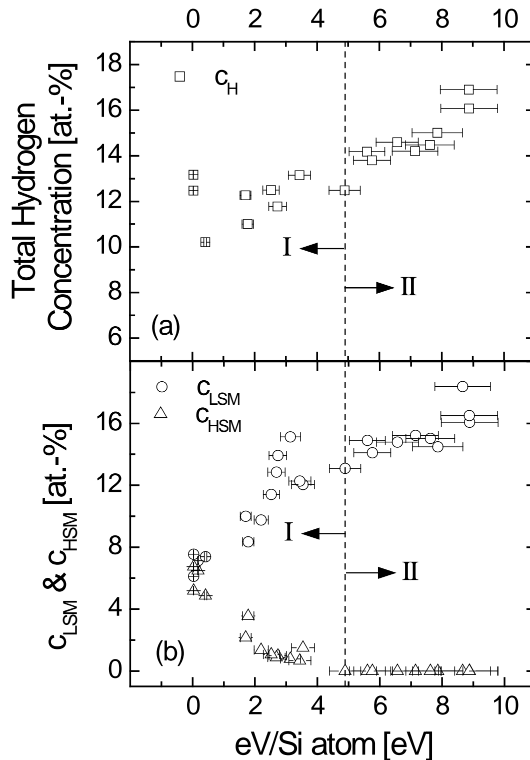

Figure 4.8 (a) The total hydrogen concentration cH as a function of energy deposited per Si atom. (b) The hydrogen associated to divacancies (cLSM) and nanovoids (cHSM) as a function of deposited energy per Si atom. The dashed lines in both figures indicate the transition from region I to region II at 4.8 eV/Si atom.

conditions the material density mainly depends on the void concentration. No material densification occurs due to a densification of the amorphous matrix upon ion bombardment. The Urbach energy, a good measure for the material disorder, is shown in Fig. 4.9b as a function of energy per deposited Si atom. Low values of around 50 meV are observed for the Urbach energy in region I and an increase can be seen from 4.8 eV/Si atom onwards, with an increasingly sharp raise towards 8 eV/Si atom up to $>$ 100 meV indicating incorporation of defects.

The increase in c_H suggests that ion bombardment and substrate temperature are not interchangeable ways of providing the film with energy. Although many film characteristics like film density, surface roughness or nanovoid con-

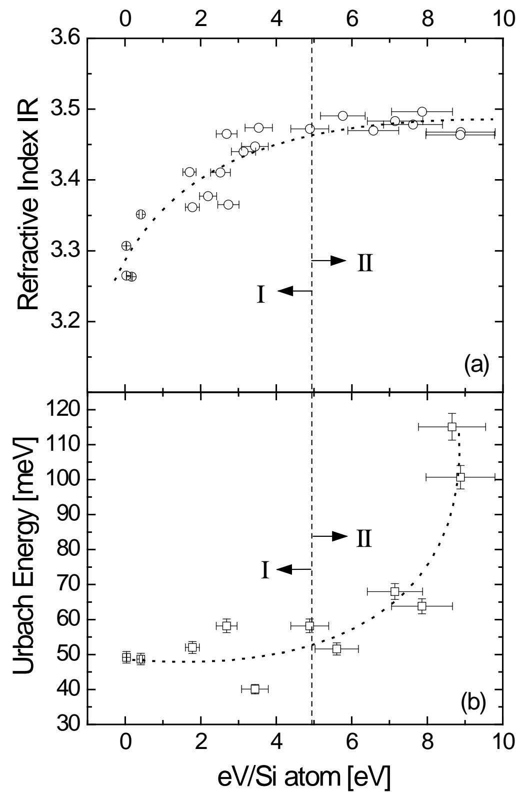

Figure 4.9 (a) The refractive index in the infra-red as obtained from FTIR analysis vs. the deposited energy per Si atom. (b) The Urbach energy vs. the deposited energy per Si atom. The dashed lines indicate the transition from region I to region II at 4.8 eV/Si atom, the dotted line in (b) is a guide to the eye.

centration behave similar for both methods, we observe a clear difference in the variation of c_H. In our experiments c_H increases with increasing deposited energy, whereas an increase in substrate temperature typically leads to a decrease in c_H [111].

As seen above, our results can be categorized into two regions, above and below 4.8 eV/Si atom. In region I, for which the deposited energy $<$ 4.8 eV/Si atom, we observe a reduction in void content, as concluded from FTIR data in Fig. 4.8b, and an increase in material density as concluded from the increase in refractive index in Fig. 4.9a. Also the roughness layer thickness development at 3000 Å shown in Fig. 4.7b suggests such a transition region, where surface smoothening is present throughout the deposited energy range, but seems to

be enhanced in region II. These observations will be discussed in terms of ion-surface interactions. We assume the dominant ion to be SiH_3^+ as a result of a charge exchange reaction between Ar^+ or H^+ and a SiH_4 molecule [46, 83]. Since the mass of the SiH_3^+ ion is very close to the mass of a silicon atom on the film surface the energy transfer between them is very efficient [109].

The a-Si:H growth mechanism is a dynamic and complex system with a multitude of surface reactions that can be considered during film growth, such as surface diffusion of several different species (SiH_3, H, -SiH_x, etc.), dangling bond coverage and formation, direct SiH_3 insertion into strained bonds, subsurface processes, etc. (see Introduction). Due to this complexity it is difficult to attribute specific changes we see in material properties upon ion bombardment to distinct interactions between bombarding ions and any of these given mechanisms relevant for a-Si:H growth. In the following discussion we focus on the interaction between bombarding ions and surface silicon atoms as well as silicon atoms within the penetration depth of the ions.

At the lowest substrate voltages simple energy transfer from impinging ions to surface atoms results in local thermal spikes and no surface or bulk Si atom displacement occurs yet. The observed smoothening of the surface already at very low energies is possibly related to enhanced surface mobility on the substrate surface, as only these processes can be activated at such low energies [52]. The mobile species are not necessarily SiH_3 radicals, also H atoms or dangling bonds as well as whole -SiH_x surface groups are possible candidates. The threshold energy for surface atom displacement of a Si surface atom exposed to an Ar ion beam (which has a mass close to that of an SiH_3^+ ion, thus we expect a similar energy transfer) has been estimated to be around 18 eV, and the threshold energy for bulk atom displacement around 40 eV [112]. Bulk atom displacement has been shown to increase sharply with increasing ion energy [112] and more energy is deposited in subsurface layers then in the surface layer at ion energies > 100 eV. This is due to repeated collisions of ions with atoms in the material at higher energies, with most of the collisions resulting only in a fractional energy transfer from ion to atom. Although sputtering can already occur at 50 eV Ar^+ ion bombardment, it is expected to become relevant for energies > 100 eV [35].

Local thermal spikes and surface atom displacement are sufficient to lead to a strong decrease in surface roughness d_s and an increase in material density as seen from the IR refractive index, without increasing the Urbach energy significantly. Broken bonds created by surface atom displacement can be annihilated easily by the incoming growth flux particles and thus do not contribute to defect creation in the material. On the other hand, in subsurface layers the more rigid atomic structure in the bulk requires more energy to rearrange and defect annihilation is less likely to occur. Thus bulk atom displacement is the

most probable effect that leads to defect creation and increased disorder in the material, as can be seen in our Urbach energy data with a strong increase at deposited energies > 4.8 eV/Si atom. This energy corresponds to V_{front} of around 100 V or ion energy of 100 eV, which we attribute to the aforementioned mechanism of subsurface atom displacement. The increase in defect density has been observed for RF substrate biasing before [87]. Significant penetration depth of ions with higher energies can also lead to what appears to be an increase in growth flux, assuming the dominant ion is SiH_3^+. Ions are typically neutralized a few angstroms above the substrate surface via a charge-exchange mechanism (Auger or resonant tunneling process) [113]. Thus the substrate surface is in fact bombarded by neutral radicals, but with the energy of the previously neutralized ion. While SiH_3 radicals typically have a reaction probability of 0.3 on an a-Si:H surface [106], the penetration of the bombarding radicals deeper into the film at sufficient energies can lead to a reaction coefficient on the order of 1, as suggested by Hamers et al. [90]. This effect might in fact be visible in Fig. 4.6 where the growth flux appears to be increasing stronger above 150 V, or equivalently > 4.8 eV/Si atom deposited. The enhanced smoothening at ion energies > 4.8 eV/Si atom observed in Fig. 4.7b can be related to enhanced etching or sputtering of the surface, which starts to become significant for $V_{front} > 100$ V.

While the increase in divacancy density for energies < 4.8 eV/Si atom could be a result of the decrease in void concentration and their transformation into vacancies, we attribute the increasing divacancy density for energies > 4.8 eV/Si atom to the breaking of subsurface bonds due to bulk atom displacement and subsequent saturation of the created dangling bond by a hydrogen atom [52]. We observe strong similarities with results reported on RF substrate biasing [52] for material grown at similar growth rates, whereas we do not observe the increase in nanovoid concentration reported by Smets et al. [52] at very high ion energies, which were obtained for higher growth rates around 2 - 4 nm/s and voltages > 100 V. Drevillon et al. [89] reported a similar increase in c_H with increasing ion energy and argued that this is the result of $Si_nH_m^+$ ions impinging on the substrate surface, associating the hydrogen incorporation with a modification of the whole a-Si:H structure and predominant bonding of the additional H in vacancies. This increase in c_{LSM} is also experimentally observed in our results.

The Tauc band gap as a function of energy per deposited Si atom can be seen in Fig. 4.10a. We observe two regions in band gap development with increasing deposited energy. Starting at 1.82 eV for unbiased material the band gap drops to $\sim$1.74 eV at 4.8 eV/Si atom. For deposited energies > 4.8 eV/Si atom the band gap is constant around 1.74 eV. Commonly a change in a-Si:H Tauc band gap is related to a change in hydrogen content c_H, usually observing an increase in band gap with increasing c_H [114]. However, comparing Fig.

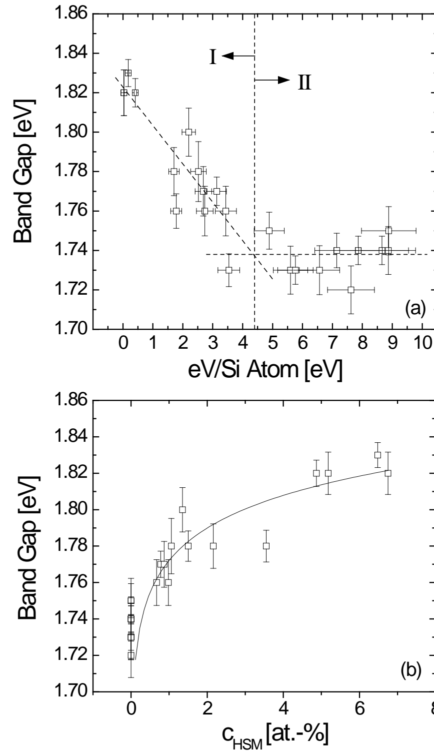

Figure 4.10 (a) The Tauc band gap as a function of deposited energy per Si atom. The vertical dashed line indicates the transition from region I to region II at 4.8 eV/Si atom, the other dashed lines are guides to the eye. (b) The Tauc band gap versus the concentration of hydrogen associated to nanovoids, cHSM. The solid line is a guide to the eye.

4.10a with Fig. 4.8a, we observe the opposite trend for our data: a decrease in band gap with increasing c_H. However, when plotting the Tauc band gap vs. the concentration of hydrogen in nanovoids, c_{HSM}, in Fig. 4.10b we see a strong correlation. This observation has been made before by Fukutani et al. [115]. They concluded from their study on sequential hydrogen and Ar ion treatments that the band gap is most strongly correlated to c_{HSM}, whereas c_H, c_{LSM}, and R^* only seem correlated to the band gap through their own correlation with c_{HSM}. In a related publication, Fortmann [116] suggests a phonon band-indirect optical gap model to explain the dependence of the band gap on c_{HSM}. Commonly, parameters that lead to a reduction in the total hydrogen content also lead to a reduction in void concentration in the material (e. g. an increasing substrate temperature), which conceals the trend we observed and suggests that the band

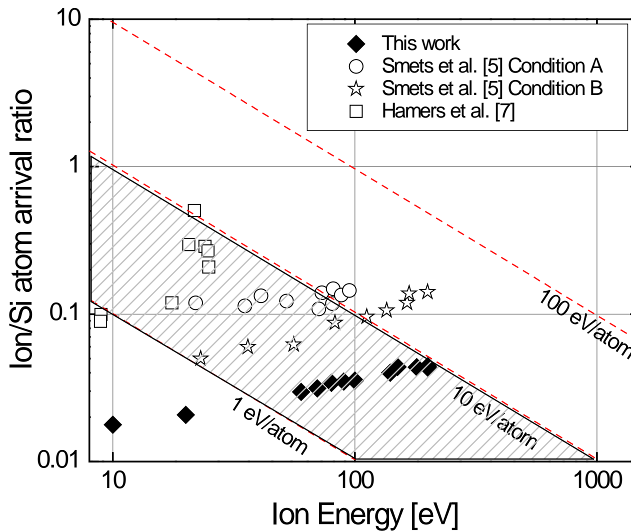

Figure 4.11 Energy deposition map containing results from this work (full diamonds), two experimental conditions of Smets et al. (empty circles and empty stars) and Hamers et al.(empty squares). The shaded area marks the region considered useful for film densification during ion-assisted film-deposition by Kaufmann et al. 34.

gap is related to c_H. In this context pulse-shaped biasing is unique, as it leads to an increase in c_H while c_{HSM} decreases, for the first time experimentally revealing the underlying trend between hydrogen and band gap. We therefore think that our results strongly suggest that the band gap is dependent on c_{HSM} as described above. Additionally, two distinct slopes can be observed in Fig. 4.10b, a steep slope < 2 at.-% c_{HSM} and a less steep slope > 2 at.-% c_{HSM}. A similar observation was reported by Smets et al. *(in Arnos thesis, ask for correct reference)* and it was suggested that the band gap is affected differently by small voids < 2 at.-% c_{HSM} than by larger voids > 2 at.-% c_{HSM}.

Following a concept introduced by Kaufmann et al. [87], Figure 4.11 shows an energy deposition map. The figure contains data from our work along with data from Smets et al. [52] deposited with the ETP-CVD technique as well as data from Hamers et al. [90] deposited with VHF-PECVD. The results from Smets et al. [52] obtained for RF biasing under condition A correspond to a-Si:H films grown at 1.1 - 1.7 nm/s and under condition B to films grown at 2.5 - 4.2 nm/s and show densification below 10 eV/Si atom similar to our results.

Hamers et al. [90] also report material densification for ion energy depositions below $<$ 10 eV/atom and constant material density for $>$ 10 eV/atom. Kaufmann et al. [87] argued that for ion assisted thin-film deposition the range of deposited ion energy that leads to material densification without increase in defect density lies between 1 and 10 eV/atom. This range is indicated in Fig. 4.11 by the dashed area. Most of our samples fall into this range of deposited energy, samples from region I that increase in density while retaining a low Urbach energy as well as samples from region II that show no increase in material density, but instead an increase in Urbach energy and presumably also in defect density. This latter increase suggests that Kaufmann's suggestion about the ideal energy deposition range $<$ 10 eV/Si atom is too general. From the average deposited energy alone conclusions about the changes in material properties can not be drawn. It is necessary to obtain information about the ion energy distribution and subsequently ion - surface- or bulk-atom interactions in order to determine ideal conditions for ion-assisted thin film deposition.

4.4 Conclusions

Pulse-shaped biasing has been investigated as a technique to achieve controlled ion bombardment during a-Si:H deposition with ETP-CVD at substrate temperatures $\sim$ 200°C. Accurate control over the substrate voltage is achieved for conductive substrates or non-conductive substrates when a conductive surface layer is connected to the substrate holder. Good control over the IEDF has been demonstrated with retarding field analyzer measurements for $V_{front} < 100$ V. The presence of negative ions/particles in the Ar-H_2-SiH_4 plasma is deduced from large positive voltages during the discharge pulse.

For material analysis as function of deposited energy per silicon atom we can distinguish roughly between two regions, region I $<$ 4.8 eV/Si atom and region II $>$ 4.8 eV/Si atom. Throughout region I we observe an increase in material density due to a decrease in nanovoid concentration as deduced from FTIR analysis. At the transition between region I and II around 4.8 eV/Si atom the densest material with low nanovoid concentration and low Urbach Energy is obtained. Above 4.8 eV/Si atom we see an increase in Urbach energy. The increase in material density and the reduction in surface roughness are attributed to an increase in surface mobility of mobile species as well as surface atom displacement. The increase in Urbach energy is related to bulk atom displacement in subsurface layers at higher ion energies. We report a clear dependence of the band gap on hydrogen in nanovoids as determined from the c_{HSM} mode, and not the correlation with the total hydrogen concentration c_H which is typically reported in literature. To our knowledge this is a unique experimental observation.

Chapter 5

Implementation of Intrinsic a-Si:H Layers Deposited with Pulse-Shaped Biasing in p-i-n Solar Cells

5.1 Introduction

An important milestone of photovoltaic (PV) module research is to reach grid parity for solar electricity, the point when photovoltaic electricity has the same cost/Watt as electricity from the grid. To this end, factors like module lifetime, energy conversion efficiency and fabrication costs are crucial and thus subject of continuous research. Depending on the development in the near future, grid parity of PV generated electricity in central Europe could be achieved between 2013-2030 according to different projections [12, 13]. Already now, in many countries PV generated electricity can be cheaper than peak prices in the electricity exchange market [10].

One technology with the potential to deliver electricity at grid parity is the thin-film solar cell technology due to the requirement of less material as well as cheaper fabrication of modules compared to crystalline silicon modules [11]. Thin film modules are expected to reach significant industrial production volumes in the near future - currently planned thin-film PV production capacities project a production share of 35% at $>$ 20 GW/year by 2012 [10]. Among the thin-film solar cells, silicon-based technologies are expected to be dominant.

Among Si-based thin-film solar cells, hydrogenated amorphous silicon

Table 5.1 Overview of solar cells deposited at different substrate temperatures with ETP-CVD.

Temperature	Efficiency	Short Circuit Current	Open Circuit Voltage	Fill Factor
°C	%	mA/cm^2	V	a. u.
200	5.8	133.0	0.81	0.53
300	4.0	123.9	0.65	0.5
400	3.7	123.1	0.63	0.47

(a-Si:H) based solar cells have always received strong attention in the research community since their first demonstration in p-i-n devices in 1976 by Carlson et al. [37]. Development of a-Si:H production technology also benefited from the increasing interest due to other potential applications in transistors or flat-panel displays [14]. Due to extensive research effort over many years, a large number of deposition techniques have been applied to deposit a-Si:H thin films. The most widespread technology is parallel-plate radio frequency-plasma enhanced chemical vapor deposition (RF-PECVD), which dominates both research and production. There are however numerous other deposition techniques available today, like very high-frequency (VHF) PECVD, hot-wire CVD (HW-CVD), Electron Cyclotron Resonance CVD (ECR-CVD) or the expanding thermal plasma CVD (ETP-CVD).

ETP-CVD is the deposition technique used in this work. It is a remote plasma technique with the potential to deposit a-Si:H at very high growth rates of > 1 nm/s [46], which indicates its potential for thin film solar cell fabrication at low cost. Deposition techniques operating at higher deposition rates enable a higher throughput in production, especially since the intrinsic absorber layer is a rather thick layer in single junction a-Si:H based solar cells. Up-scaling of this technique has been demonstrated in the past [117]. Problematic in terms of p-i-n solar cell deposition is the need of substrate temperatures $> 300°$C in the ETP-CVD technique in order to obtain dense, void-free a-Si:H films required for solar cell application. At these temperatures the p-doped layer undergoes thermal degradation which reduces the resulting energy conversion efficiency of the fabricated solar cells. This decrease in efficiency can be seen in Table 5.1, where the external solar cell parameters are shown for three solar cells deposited at substrate temperatures between 200 – 400°C. In particular, both open-circuit voltage and short-circuit current density show a substantial decrease, while the fill factor decreases only slightly. Consequently, in ETP-CVD substrate temperatures $< 250°$C for the intrinsic layer deposition are desired. In order to reduce the substrate temperature while maintaining the material quality, an alternative approach is to provide the growing film surface with additional energy through ion bombardment. Ions are naturally present in a plasma, so ion bombardment

can simply be achieved by accelerating positive ions onto the substrate surface by applying a negative voltage to the substrate. The simplest way to obtain ion bombardment is by applying an external, sinusoidal rf voltage at 13.56 MHz to the substrate voltage. This method has been explored for ETP-CVD deposition in the past [48, 52], and it was demonstrated that it can result in deposition of dense, void-free material at substrate temperatures of 200°C [52]. However, the high frequency excitation during sinusoidal rf biasing can result in the formation of a strong secondary plasma around the substrate holder, which affects both the ion flux as well as the growth flux composition [48]. Moreover, the ion energy distribution becomes broad and bimodal [49, 50] and control over both ion flux and ion energy is imprecise.

A method to avoid these shortcomings of rf biasing has been proposed by Wang et al. [54] with the pulse-shaped biasing (PSB) technique, which will be employed in this work. By means of a tailored waveform, a near-constant voltage is obtained on the substrate, interrupted by discharge pulses. With this method, control over both the ion energy distribution (IED) and the ion flux is obtained [102], at sufficiently low frequencies of 100 kHz to avoid significant power coupling to the plasma and suppression of a strong secondary plasma around the substrate. The resulting narrow IED can be scanned over a wide range of ion energies and the effect of distinct ion energies on material properties can be investigated [118].

This paper is split into two sections: in the first section we discuss the effect of PSB on the deposition of intrinsic a-Si:H, focusing on material properties relevant to solar cell application. In the second section we incorporate these pulse-shape biased intrinsic a-Si:H layers into p-i-n solar cells and relate the resulting solar cell properties to the observed changes in material properties discussed in the first section.

5.2 Experimental Details

Intrinsic and n-doped a-Si:H layers were deposited in a three-chamber vacuum system. Two chambers are used for material deposition and one for sample transfer and loading. One deposition chamber utilizes the ETP-CVD for the deposition of intrinsic a-Si:H around 1 nm/s. In this chamber the pulse-shaped biasing technique was applied during deposition of intrinsic a-Si:H. In the other deposition chamber radio-frequency plasma-enhanced chemical vapor deposition (rf-PECVD) for deposition of both p- and n-doped a-Si:H layers is employed.

The ETP-CVD technique is shown schematically in Fig. 5.1. The technique has been described in detail by Van de Sanden et al. [46]. In brief, an Ar-H_2 plasma is ignited and sustained in a cascaded arc at pressures around 0.5

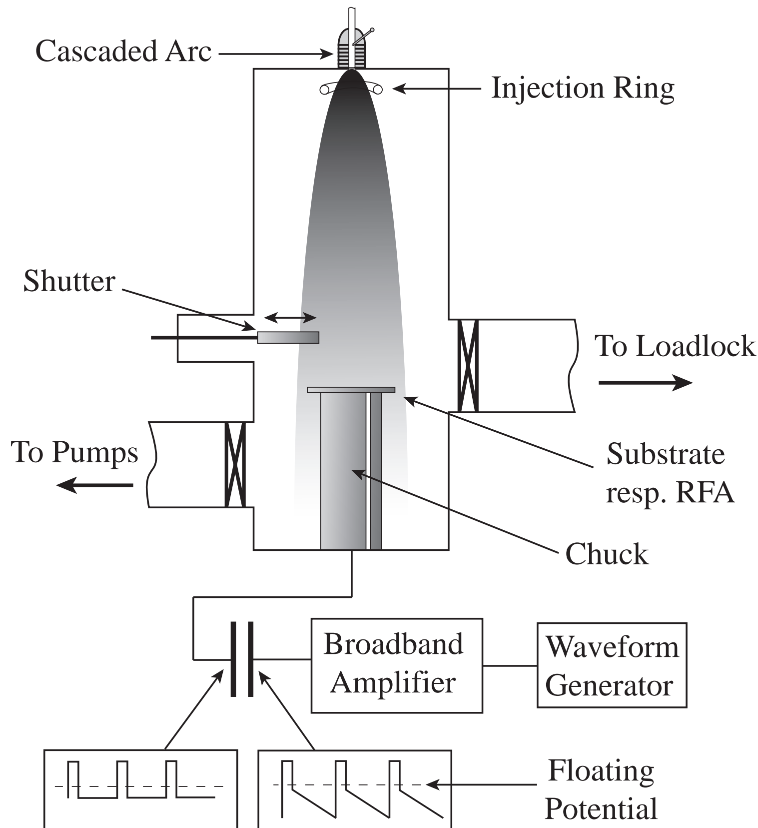

Figure 5.1 Schematic drawing of the ETP-CVD setup and the connected PSB setup.

bar. The plasma expands supersonically through a nozzle into a low pressure deposition chamber (∼0.15 mbar). The nozzle also serves as an additional injection point for H_2 gas. The SiH_4 gas is injected into the Ar-H_2 plasma through an injection ring ∼10 cm below the nozzle and subsequently dissociates predominantly into SiH_3. These radicals are transported to the temperature controlled substrate holder where the a-Si:H film is deposited on the substrate surface.

The pulse-shaped biasing setup has been designed similar to the setup described by Wang et al. [54] and has been adapted to our ETP-CVD reactor. The whole biasing setup is shown in Fig. 5.1. The non-sinusoidal waveform is created by an arbitrary waveform generator (Agilent 33250A) and a broadband amplifier (Amplifier Research 150A250). The amplifier is connected via a 1-nF coupling capacitor to the chuck where the substrate holder is located. A frequency of 100 kHz was used for all depositions in this work.

The operating principle of pulse-shaped biasing technique has been described in detail in a related publication [118]. In brief, by applying a specially tailored waveform to the substrate during deposition a constant negative potential is obtained on the sample holder for most part of one period, T, of the waveform. This results in a very narrow ion energy distribution function (IEDF). A schematic version of the waveform at the amplifier output can be seen in Fig. 5.2a and on the substrate surface in Fig. 5.2b. Each period of the amplifier output consists of a ramp with a negative slope followed by a discharge pulse. The negative slope, V_{slope}, in the output signal of the amplifier is tuned in such a way that it exactly balances the charge built-up during the ramp. As a result we obtain a constant negative potential V_{front} on the substrate surface during this part of the waveform for deposition on both glass coated with a conductive TCO layer as well as conductive substrates [118]. As charge cannot be accumulated indefinitely the pulse is necessary to discharge the substrate regularly at a voltage above floating potential, allowing negative charge carriers to reach the substrate surface.

For all intrinsic layer depositions the gas flows were 570 sccm Ar and 190 sccm H_2 in the arc, 150 sccm H_2 in the nozzle and 230 sccm SiH_4 in the injection ring, at a current of 40 A in the arc. Due to interference between the voltage applied during substrate biasing and the thermocouple located in the chuck the thermocouple had to be disconnected during biased depositions, impeding active temperature control during depositions. To accommodate for this restriction, the samples were heated up to 210°C prior to deposition before the thermocouple was disconnected. During deposition the temperature dropped to about 185°C. The deposition time was 6.15 minutes for all individual intrinsic layer depositions and was adjusted for intrinsic layer depositions for solar cells to ensure that all layers had the same final thickness of about 300 nm. The deposition rate was about 0.8 nm/s for unbiased and increased up to 1 nm/s for biased depositions.

Our p-i-n-solar cells were deposited on Asahi U-type substrates with 700 nm SnO_2:F. Deposition of a-SiC:H p- and buffer-layers were carried out in a separate rf-PECVD reactor for which optimized procedures were available. Following the p-layer deposition a thin a-SiC:H buffer layer of ~5 nm was deposited before the samples was transferred to the CASCADE setup. Sample transfer into the CASCADE setup meant that the samples were exposed to atmospheric conditions for a brief moment before processing continued with the intrinsic a-Si:H deposition in the ETP-CVD chamber After deposition of the intrinsic layer the n-layer was deposited in the rf-PECVD chamber of the CASCADE setup. Gas flows were 40 sccm SiH_4 and 11 sccm PH_3 at a power of 1.3 W and an electrode distance of 21.5 mm, deposition time was 13 minutes. Subsequently an Ag reflective layer (100 nm) and Al protective contacts (200 nm) were thermally

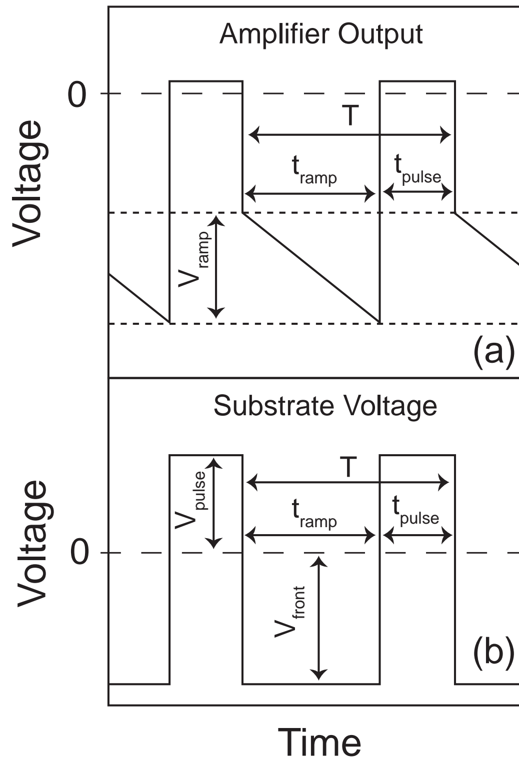

Figure 5.2 Schematic versions of the applied pulse-shaped waveform at (a) the broadband amplifier output and (b) on the substrate surface. Important characteristics of the waveforms are indicated in the figure.

evaporated onto the substrate through a shadow mask, resulting in 30 cells of 4 mm $\times$ 4 mm per sample.

For analysis of intrinsic material properties, a-Si:H films were deposited on both c-Si wafers and glass substrates. Crystalline Si wafer substrates (prime wafer, 500-550 μm) with $\sim$2 nm native oxide have been used for in situ real-time spectroscopic ellipsometry (RTSE) measurements and Fourier transform infrared spectroscopy (FTIR) analysis (Nicolet 5700, Thermo Electron Corp.). From FTIR spectra the integrated absorption of the wagging mode (at 640 cm^{-1}), the low stretching mode (LSM at 2000 cm^{-1}) and high stretching mode (HSM at 2100 cm^{-1}) were determined, from which the total hydrogen concentration, c_H, the hydrogen concentration incorporated in vacancies, c_{LSM}, and nanovoids, c_{HSM}, respectively, was calculated. RTSE measurements were performed using a J. A. Woollam Co., Inc M-2000F spectroscopic ellipsometer. In our RTSE data analysis we followed a procedure that was described in detail

by Van den Oever et al. [63]. The a-Si:H dielectric function is obtained from the Tauc-Lorentz parameterization. The only dynamic fitting parameters are the bulk film thickness d_b and the surface roughness d_s.

Optical and electrical measurements were carried out on films deposited on Corning 7059 glass with coplanar Al contacts, 20 mm long and 0.5 mm apart, to determine optical constants, band gap, Urbach energy, dark- and photoconductivity. For reflection-transmission measurements our spectrometer setup consisted of a halogen lamp and a SPEX 1680B monochromator. The Urbach energy was determined from combined reflection-transmission measurements and dual-beam photoconductivity (DBP) measurements. The dark conductivity was measured using a Temptronic Thermo-Chuck system for temperature control and a Keithley 617 electrometer. Measurements were carried out from 60 to 130°C and the dark conductivity at room temperature was extrapolated from these data. Photoconductivity was determined using an Oriel solar simulator with an He-Xe lamp at 300 W providing an AM1.5 spectrum, and a Hewlett Packard 4145B parameter analyzer.

For p-i-n solar cells illuminated current-voltage as well as quantum efficiency measurements were carried out. Solar cell illumination characteristics were obtained from current-voltage measurements under AM1.5 conditions between -0.1 and $+0.85$ V using the above mentioned Oriel solar simulator. From these J-V curves we obtained the short-circuit current density J_{SC}, open-circuit voltage V_{OC}, fill factor FF and the energy conversion efficiency η. External quantum efficiency was measured in a wavelength range from 300 to 850 nm, typically both unbiased and at -1 V biasing, with a spectral response setup consisting of an Oriel Cornerstone 130 monochromator and Oriel Apex monochromator illuminator.

5.3 Results & Discussion

In a related publication [118] the control PSB can give over the IEDF has been demonstrated and additional material properties for intrinsic a-Si:H have been analyzed as function of ion bombardment. In this chapter we focus on material properties relevant for solar cell application. All material properties are discussed in terms of the average supplied energy per deposited silicon atom, which is determined as follows:

The growth flux, the ion flux and the resulting average energy supplied per incorporated Si atom, hereafter called deposited energy (eV/Si atom) as a function of substrate voltage, can be seen in Fig. 5.3. The Clausius-Mossotti relation was used to determine the growth flux Γ_{Si} of the films from the film density, the infrared (IR) refractive index and the total hydrogen content obtained from FTIR measurements. The ion flux during the ramp Γ_{ion} was directly determined

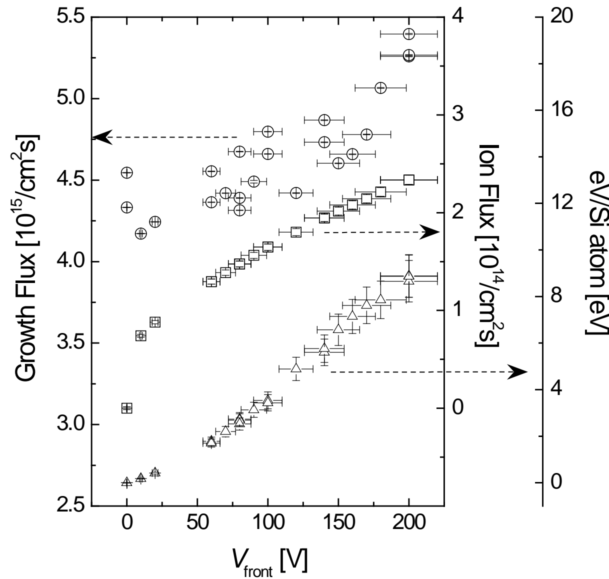

Figure 5.3 Growth flux Γ_{Si}, ion flux Γ_{ion} and energy deposited per incorporated Si atom vs. the surface voltage V_{front}.

from the substrate current J_s by means of a square platinum probe. The continuous increase of the growth flux as a function of substrate voltage is a result of additional SiH_3 production in the plasma [52,106]. The increasing ion flux is related to both the ionization in the secondary plasma as well as the rise in ion current due to a thicker plasma sheath around the substrate holder and thus collection area at higher V_{front} [107]. The ratio between the two fluxes multiplied by the average substrate voltage determines the average energy deposited per incorporated Si atom.

5.3.1 Intrinsic a-Si:H Analysis

The IR refractive index obtained from FTIR analysis is shown in Fig. 5.4a as a function of deposited energy per Si atom and shows a clear separation into two regions, I and II. In region I, below 4.8 eV/Si atom, the refractive index continuously increases, indicating an increase in film density. Above 4.8 eV/Si atom the refractive index is constant and does not change with deposited energy. We observed the same trend in FTIR analysis (not shown) [118], where we determined a reduction in void content from the low stretching mode, c_{HSM}, below 4.8 eV/Si atom until it can no longer be detected > 4.8 eV/Si atom. The clear relation between void concentration and IR refractive index indicates that

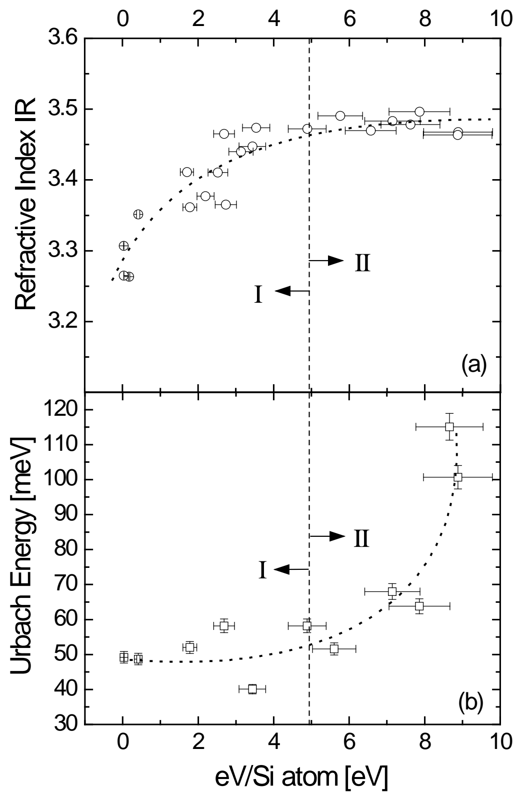

Figure 5.4 (a) The refractive index in the infra-red as obtained from FTIR analysis vs. the deposited energy per Si atom; (b) the Urbach energy vs. the deposited energy per Si atom. The dashed lines indicate the transition from region I to region II at 4.8 eV/Si atom, the dotted line in (b) is a guide to the eye.

for our experimental conditions the material density mainly depends on the void concentration. No material densification occurs from a further densification of the amorphous matrix upon ion bombardment. The Urbach energy, a good measure for the material disorder and indicator of defects in the material, is shown in Fig. 5.4b as a function of eV/Si atom. A low Urbach energy of around 50 meV is observed in region I and an increase can be seen from 4.8 eV/Si atom onwards, with an increasingly sharp rise up to $>$ 100 meV towards 8 eV/Si atom. The defect density shows an exponential dependence on Urbach energy due to conversion of strained, weak bonds in the valence band tail states into dangling bond defects [80].

These trends for refractive index and Urbach energy can be related to

specific ion-surface interactions [118]. We assume the dominant ion to be SiH_3^+ as a result of a charge exchange reaction between Ar^+ or H^+ and a SiH_4 molecule [46, 83]. At the lowest substrate voltages simple energy transfer from impinging ions to surface atoms results in a local thermal spikes. Surface diffusion of growth precursors on the substrate surface can be activated by such low energies [52], but no surface or bulk Si atom displacement occurs yet. The diffusing species must not necessarily be SiH_3radicals, also H atoms or dangling bonds are possible candidates. The threshold energy for surface atom displacement of a Si surface atom exposed to an Ar ion beam has been estimated to be around 18 eV, and the threshold energy for bulk atom displacement around 40 eV [112]. Both enhanced diffusion length as well as surface atom displacement can lead to a densification of the film, as concluded from the increase of IR refractive index. While broken bonds created by surface atom displacement can be annihilated easily by the incoming growth flux particles, broken bonds created by bulk atom displacement in subsurface layers requires rearrangement of the more rigid a-Si:H network and thus defect annihilation is less likely to occur. Thus bulk atom displacement is the most likely candidate leading to defect creation and increased disorder in the material, as can be observed in our Urbach energy data with a strong increase at deposited energies > 4.8 eV/Si atom.

In Fig. 5.5 the Tauc band gap is shown vs. the deposited energy per Si atom. Also here we observe two regions in band gap development with increasing deposited energy. Starting at 1.82 eV for unbiased material the band gap drops to $\sim$1.74 eV at 4.8 eV/Si atom. For deposited energies > 4.8 eV/Si atom the band gap is constant around 1.74 eV. A change in a-Si:H band gap is usually attributed to a change in total hydrogen content [114]. However, for samples deposited with PSB we have reported a clear dependence of the band gap on the nanovoid content in the material, deduced from the hydrogen absorption in the high stretching mode [118]. It had been suggested before that this could be explained by a phonon band-indirect optical gap [116].

The dependence of photoconductivity, dark conductivity and photo response on deposited energy can be seen in Fig. 5.6a, b and c, respectively. Both dark and photoconductivity increase with deposited energy until a plateau is reached around 4.8 eV/Si atom above which both remain constant, around 6×10^{-6} S/cm and 1×10^{-11} S/cm for photo- and dark conductivity, respectively. These are again the same distinct two regions identified above, with a transition around 4.8 eV/Si atom. The photoresponse (which is the ratio of photoconductivity to dark conductivity) reaches a maximum of 2×10^6 already around 3 eV/Si atom, due to the stronger increase in dark conductivity relative to the photoconductivity.

The trend in dark conductivity is directly related to the change in band

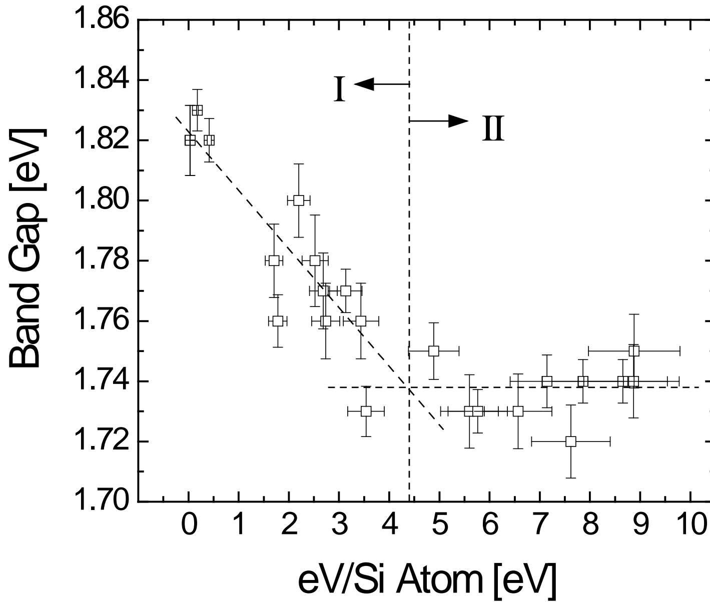

Figure 5.5 The Tauc band gap as function of deposited energy per Si atom. Dashed lines serve as guide to the eye. Also the transition from region I to region II is indicated by a vertical line.

gap with deposited energy. For a semiconductor, the conductivity is determined from:

$$\sigma = q(\mu_e n_e + \mu_h n_h) \tag{5.1}$$

with n_e and n_h the electron and hole concentration and μ_e and μ_h the electron and hole mobility, respectively. For an intrinsic semiconductor we can assume that $n_e = n_h = n_i$, with n_i the intrinsic charge carrier concentration. n_i is exponentially related to the band gap through:

$$n_i = \sqrt{N_C N_V} \cdot e^{-E_g/2k_B T} \tag{5.2}$$

with N_C and N_V the effective density of states in conduction and valence band, respectively, E_g the band gap and T the temperature. Assuming all other factors constant, we obtain a direct relation between the conductivity and the band gap with a proportionality of $e^{-E_g/2k_B T}$. This relation is plotted in Fig. 5.7a as solid line along with the experimental values. The good match between the experimental trend and fit following Eq. 5.2 demonstrates that (i) the change

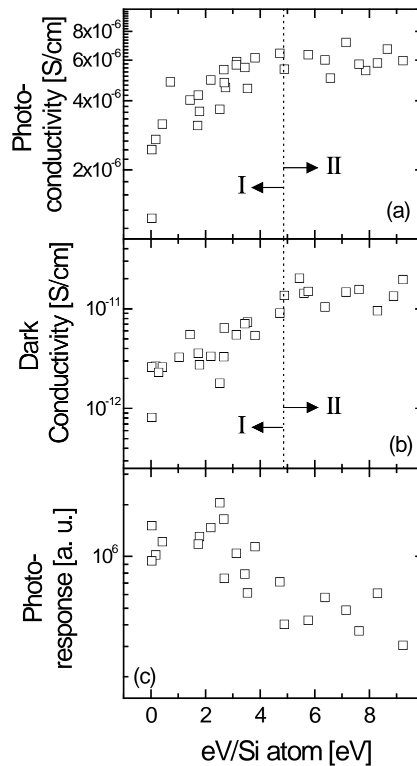

Figure 5.6 (a) The photoconductivity, (b) dark conductivity and (c) photoresponse as function of deposited energy per Si atom. The transition from region I to region II is indicated in (a) and (b) by a vertical dashed line.

in dark conductivity is a direct result of the decrease in band gap with increasing deposited energy and (ii) indicates that both electron and hole mobilities are not affected by ion bombardment and remain relatively unchanged.

Since the charge carrier mobility appears to be unaffected by substrate biasing, the change in photoconductivity must also be related to the change in free charge carrier density. For illuminated samples the concentration of photogenerated charge carriers exceeds the intrinsic charge carrier concentration by far and the change in conductivity cannot be explained by the increase in intrinsic charge carrier concentration due to reduced band gap. The photogenerated charge carrier concentration is related to the absorption coefficient of the film. Figure 5.7b shows the change in absorption coefficient α, as obtained from SE measurements, from 1.5 – 3.75 eV, for samples deposited at no substrate biasing, 3.8 eV/Si atom and 8.9 eV/Si atom. An increase in α will increase the

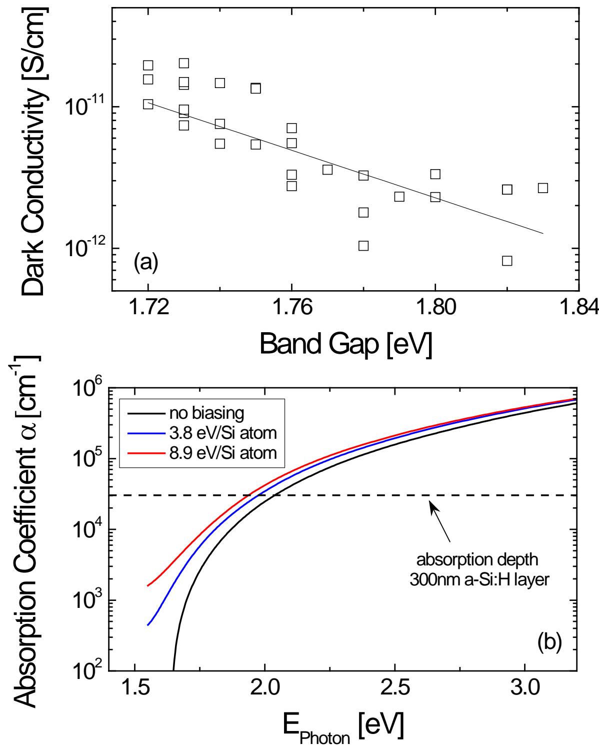

Figure 5.7 (a) The dark conductivity as function of Tauc band gap. The exponential relationship between these two properties is shown in the plot by a solid line. (b) The absorption coefficient as function of photon energy for unbiased deposition (black line) and biased deposition at 3.8 eV/Si atom (blue line) and 8.9 eV/Si atom (red line). The horizontal line indicates the absorption depth for a 300 nm thick a-Si:H film.

photo-generated charge carrier concentration. We observe an increase in α at mild substrate biasing with 3.8 eV/Si atom, where the increase in α for photon energies $E_{photon} < 1.75$ eV is presumably related to the decrease in band gap described above. Therefore more electron-hole pairs are generated leading to a higher conductivity. Despite the slightly higher α at substrate biasing around 8.9 eV/Si atom the photoconductivity remains constant above 4.8 eV/Si atom. This can be related to an increase in defect density as discussed above, reducing the charge carrier density by stronger electron-hole recombination.

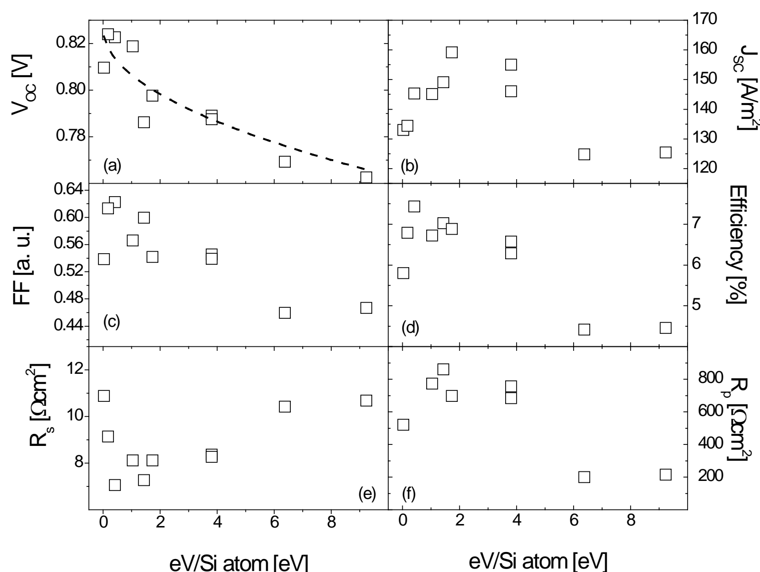

Figure 5.8 The external solar cell parameters as function of deposited energy per Si atom. Shown are the (a) V_{OC}, (b) J_{SC}, (c) FF, (d) η, (e) R_s, and (f) R_p. Additionally the theoretical relationship between band gap and V_{OC} is shown in (a) by a dashed line.

5.3.2 Solar Cell Analysis

Solar cells have been deposited with intrinsic a-Si:H deposition utilizing PSB in the same way as described above. In the following, we discuss the properties of the obtained solar cells and relate these results to the changes in material properties discussed in the previous section.

Several important solar cell characteristics are summarized in Fig. 5.8. Shown versus the deposited energy per Si atom are key characteristics averaged over the top 10 dots per sample in terms of energy conversion efficiency. Shown are the open-circuit voltage V_{OC}, short-circuit current density J_{SC}, fill factor FF, energy conversion efficiency η, series resistance R_s and shunt resistance R_p in Fig. 5.8 a-f, respectively. In Fig. 5.9 representative J-V curves for each cell are shown for different deposited energies. The dashed line represents the J-V curve for unbiased depositions and the solid line the sample with PSB.

We see in Fig. 5.8 how V_{OC}, FF and η show a very similar dependence in the deposited energy. All three increase strongly at very low deposited energies, reach a maximum around 1 – 2 eV/Si atom and subsequently decrease at higher deposited energies. For the cell deposited at about 0.8 eV/Si atom we obtain a record efficiency of 7.4% for solar cells deposited with ETP-CVD at substrate

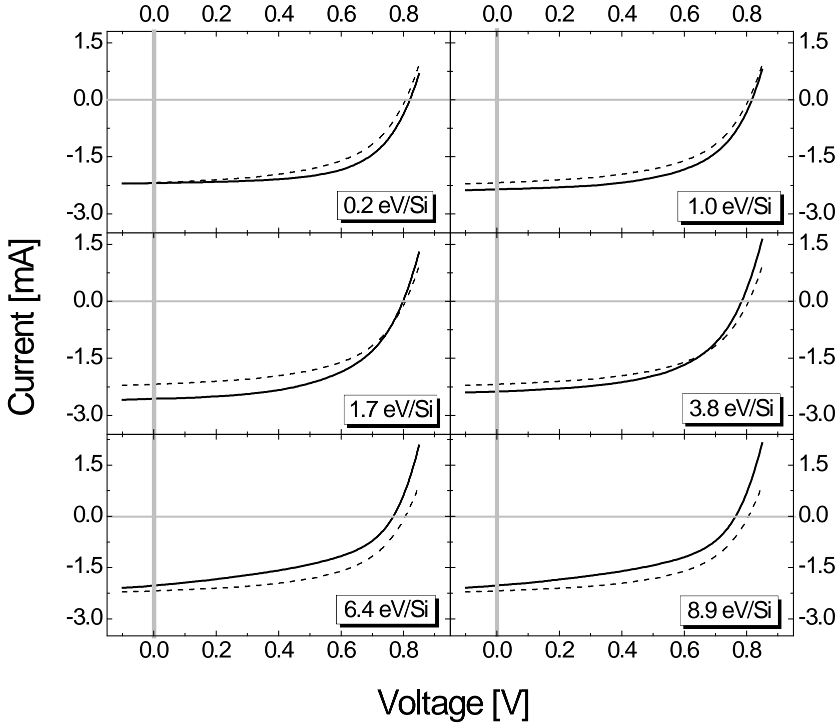

Figure 5.9 Current-voltage relationships for solar cells with the intrinsic layer deposited at 0.2 eV/Si atom (a), 1 eV/Si atom (b), 1.7 eV/Si atom (c), 3.8 eV/Si atom (d), 6.4 eV/Si atom (e) and 8.9 eV/Si atom (f). In each graph the current-voltage relationship for a solar cell deposited without substrate biasing is shown as dashed line.

temperatures around 200°C. With increasing energy the efficiency drops quickly to values below 5% at the highest deposited energy. This is a result of the strong decrease in FF, which drops from 0.625 at ~ 1 eV/Si atom to < 0.5 at the highest deposited energies. The trend for J_{SC} is shifted by about 2 eV/Si atom. Starting at 132 A/m^2 for unbiased cells we see a continuous increase until a maximum current of > 150 A/m^2 is reached $\sim$4 eV/Si atom. Subsequently the current drops below the unbiased value at higher energies. The described changes in J_{SC}, V_{OC} and FF with deposited energy can also be seen in the J-V curves in Fig. 5.9.

The change in V_{OC} can be directly related to the decrease in band gap shown in Fig. 5.5 as follows. An estimate of V_{OC} is given by:

$$V_{OC} \approx \frac{k_B T}{q} ln(\frac{J_{SC}}{J_0}) \tag{5.3}$$

with k_B the Boltzmann constant, T the temperature, q the elementary charge, J_{SC} the short circuit current and J_0 the dark saturation current [11]. With J_{SC} known from the measurement, the only other band gap dependent factor is J_0 which is proportional to n_i^2 , which in turn is related to the band gap through an exponential relationship $\propto e^{-E_g/2k_BT}$ [11]. This relationship is shown in Fig. 5.8a as a dashed line and reproduces the experimental trend very well, apart from the increase in V_{OC} at deposited energies around 0.5 eV/Si atom which could be related to an improved p-i interface upon ion bombardment. However, the reported changes in V_{OC} are predominantly a result of the decrease in band gap with increasing deposited energy per Si atom.

In order to explain the development of J_{SC} with deposited energy we analyze the spectral response of the cells with (external) quantum efficiency (QE) measurements. QE measurements are commonly used to determine the losses responsible for drops in measured J_{SC} compared to the maximum achievable photocurrent. QE measurements for different deposited energies are shown in Fig. 5.10, with the dashed lines showing the QE measurement for a cell deposited without PSB and the solid lines the results of cells using PSB. Up to 1.7 eV/Si atom we see an increase in the red response and subsequently a drop below quantum efficiencies of unbiased samples. The increase for energies $<$ 1.7 eV/Si atom is due to the increase of the absorption coefficient in the red as a result of the decrease in band gap. However, the subsequent decrease in red response is in contrast to the continuing decrease of band gap until a minimum is reached at 4.8 eV/Si atom. Biased QE measurements in Fig. 5.11 show the unbiased QE measurement normalized to QE measurements at -1 V biasing. Negative sample biasing during QE measurements increases the electric field between the doped layers and improves the collection of photogenerated charge carriers. At sufficiently large reverse bias all photogenerated charge carriers are collected and no electric collection losses occur [82]. Not only does this allow to distinguish between optical losses and electrical losses in a solar cell, but it also allows to distinguish between loss of electrons and holes due to their different mobilities [82]. Considering the red response in Fig. 5.11, the slight increase of QE(0V)/QE(-1V) in the red part of the spectrum at 1 eV/Si atom suggests an improvement in hole collection at the p-i-interface, since holes generated from red light absorption at the back of the cell have to drift the longest distance to reach the p-layer. Accordingly, the decrease of QE(0V)/QE(-1V) observed in the red part of the spectrum for deposited energies $>$ 1 eV/Si atom corresponds to a decrease in hole collection. This can be explained by the increase in defect state density at higher deposited energies per deposited Si atom as indicated from the Urbach energy plot in Fig. 5.4. An increase in defect density increases

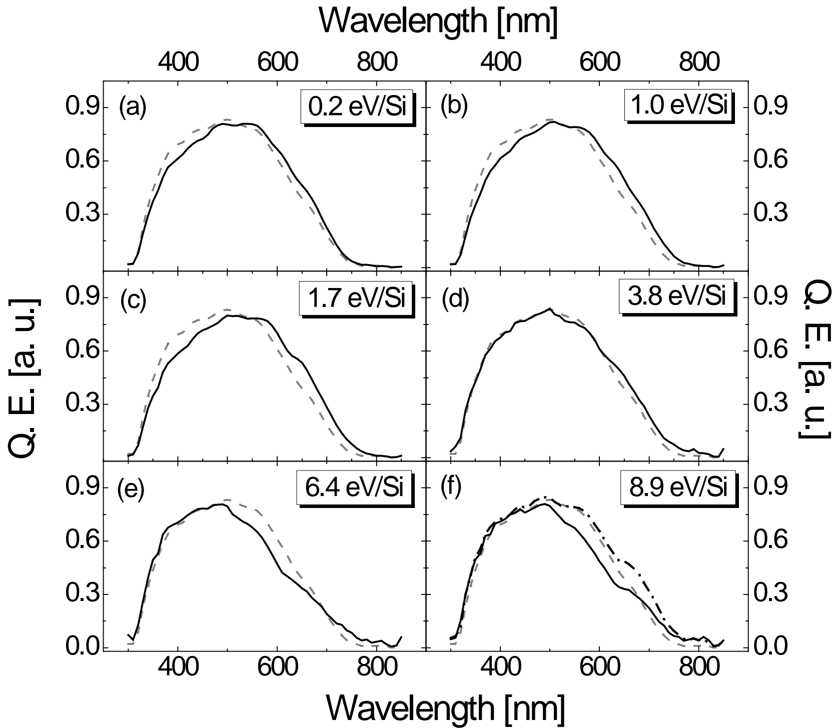

Figure 5.10 The external quantum efficiency for solar cells with the intrinsic layer deposited at (a) 0.2 eV/Si atom, (b) 1 eV/Si atom, (c) 1.7 eV/Si atom, (d) 3.8 eV/Si atom, (e) 6.4 eV/Si atom and (f) 8.9 eV/Si atom. In each graph the external quantum efficiency for a solar cell deposited without substrate biasing is shown as dashed line. In (f) also the external quantum efficiency for a solar cell deposited at 8.9 eV/Si atom is shown when a -1 V bias is applied during the measurement.

the chance that holes generated in the back of the cell are trapped in a defect state and recombine while drifting across the i-layer. Above $\sim$ 3 eV/Si atom the reduction in hole collection begins to compensate for the increase in absorption coefficient due to reduced band gap and the QE for higher wavelengths drops. This becomes very pronounced for samples deposited with $>$ 6.4 eV/Si atom deposited energy where the QE decreases by up to 30% due to electrical losses. These biased QE results also indicate that defect formation already starts at deposited energies between 1.7 - 3.8 eV/Si atom, and not > 4.8 eV/Si atom as deduced from the Urbach energy in Fig. 5.4b. The influence of charge carrier recombination on the QE at 8.9 eV/Si atom is shown in Fig. 5.10f where in addition to QE(0 V) also QE(-1 V) is shown as dash-dotted line and a strong decrease $>$ 500 nm can be observed.

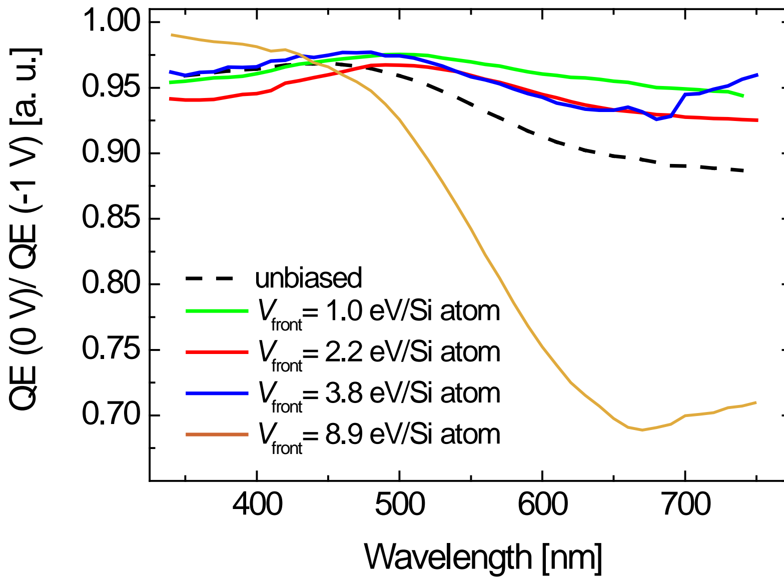

Figure 5.11 The ratio between the external quantum efficiency measured at 0 V substrate bias and at -1 V substrate bias, QE (0 V)/QE(-1 V), for solar cells deposited without substrate biasing during the intrinsic layer deposition as well as with deposited energies of 1 eV/Si atom (green line), 2.2 eV/Si atom (red line), 3.8 eV/Si atom (blue line) and 8.9 eV/Si atom (yellow line) during intrinsic layer deposition.

The fill factor as a function of deposited energy per Si atom in Fig. 5.8c develops similarly to V_{OC} and η, with a strong initial increase and a maximum of 0.62 around 0.5 eV/Si atom, followed by a continuous decrease with increasing deposited energy. It is difficult to draw conclusions about the FF from illuminated J-V measurements alone, as the FF depends mostly on parameters that are not directly accessible from these J-V measurements, namely the ideality factor n, the series resistance R_s and the shunt resistance R_{sh} (although illuminated J-V curves can give us an indication of R_s and R_{sh}) [119]. Presumably FF will depend strongest on the ideality factor since n is a measure for charge carrier recombination [119]. The strong dependence of the FF on the mobility-lifetime product has been discussed in literature [120]. Charge carrier recombination is related to the defect density, which we assume to be increasing $>$ 4.8 eV/Si atom as deduced indirectly from the Urbach energy seen in Fig. 5.4b. However, already the QE results discussed above indicated that the onset of defect generation might in fact already occur at lower deposited energies per

Si atom between 1.7 - 3.8 eV/Si atom, a suggestion which is further corroborated by the observed trend in FF. The strong increase in FF at very low deposited energies $\sim$ 0.5 eV/Si atom could be a result of an improved p-i interface, as suggested above for the increased V_{OC} for similar deposited energies. The parasitic resistances R_s and R_{sh} in Fig. 5.8e and 5.8f show a minimum for R_s and a maximum for R_{sh} around 0.5 eV/Si atom and increase respectively decrease at higher deposited energies. Both an increase in R_s and a decrease in R_{sh} result in a decrease in fill factor [119], but both resistances would need to be measured separately to be able to distinguish between the influence of resistances and of recombination on FF. The power efficiency in Fig. 5.8d is directly related to V_{OC}, J_{SC} and FF. Of these parameters FF has the strongest dependence on the deposited energy per Si atom and accounts for most of the increase in η at low deposited energies as well as the decrease $>$ 1 eV/Si atom. [120]

5.4 Conclusions

Pulse-shaped biasing has been applied in the deposition of intrinsic a-Si:H layers at substrate temperatures around 200°C and growth rates around 1 nm/s. These layers have been implemented in p-i-n solar cells and record initial energy conversion efficiencies of 7.4% have been obtained for cells grown by ETP-CVD with the intrinsic layer grown at such high growth rates and low substrate temperatures. The open-circuit voltage has a maximum of 0.82 V around 1 eV/Si atom and decreases at higher deposited energy, which can be attributed to the decrease in band gap with increasing deposited energy. The short-circuit current density reaches a maximum around 4.8 eV/Si atom and decreases at higher deposited energies due to an increase in hole collection losses as determined from external quantum efficiency measurements. The decrease in fill factor above 1 eV/Si, atom which we suggest is related to a decrease in mobility-lifetime product due to increasing charge carrier recombination as result of defect generation at deposited energies above 1.7 eV/Si atom.

Chapter 6

On the Surface Roughness Evolution of a-Si:H films

6.1 Influence of RF Substrate Biasing on the Surface Roughness Evolution

6.1.1 Introduction

The kinetic roughening of thin film growth follows from a competition between roughening and smoothening mechanisms. Thus from a study of the surface roughness evolution versus deposition time, insight into growth mechanisms, and their influence on structural properties of films can be gained. Consequently, there is a strong technological motivation to understand the origin of surface roughness and morphology.

Hydrogenated amorphous silicon (a-Si:H) develops extraordinarily smooth surfaces under optimum growth conditions, which is an indication for the presence of strong smoothening mechanisms during film growth. Surface smoothening is usually attributed to surface diffusion of growth precursor molecules [121] and is assumed to be a dominant surface mechanism for mass transport in different a-Si:H deposition techniques such as plasma-enhanced chemical vapor deposition (PE-CVD) [121] or hot-wire CVD (HW-CVD) [72]. The driving force for surface diffusion of radicals toward surface valleys is described by a chemical potential proportional to the curvature of surface features. This leads to a diffusion away from surface hills (negative curvature) and toward surface valleys (positive curvature) [122]. Diffusion lengths around 50 -Ű 100 Å are typically assumed to explain the surface morphology obtained for a-Si:H thin

films [121].

However, regularly experimental and modeling results are published, which conflict with the idea of dominant surface diffusion of physisorbed SiH_3 radicals. Ceriotti and Bernasconi [29] have utilized ab initio calculations to investigate surface diffusion of SiH_3 radicals on fully hydrogenated H:Si (100) surfaces and obtained maximum diffusion lengths in the order of only a few lattice spacings at temperatures ranging from 300 to 1000 K, due to quick desorption of physisorbed SiH_3 radicals. Consequently, SiH_3 surface diffusion would not be able to explain the development of surface features in the nanometer range, as is observed for a-Si:H thin film growth with atomic force microscopy (AFM) (e.g., Sperling and Abelson [123]). Cheng et al. [31] concluded from experimental low-pressure CVD (LPCVD) studies utilizing a special cavity that surface diffusion does not play a significant role for step coverage. Smets et al. [28] obtained a rather high activation energy for surface smoothening of around 1 eV for a-Si:H film growth from solid-on-solid modeling, which conflicts with the low activation energy of SiH_3 radicals on a hydrogenated surface.

In this section, we will present in situ real-time spectroscopic ellipsometry (RTSE) results of a-Si:H thin films grown with the ETP-CVD technique at growth rates of about 1 Å/s for substrate temperatures ranging from 150 to 400°C. We will address the evolution of the surface roughness to gain insight into mass transport mechanisms that underlie our experimental observations and show that our results cannot be explained by a simple surface-diffusion dominated growth model of physisorbed SiH_3 radicals. Additionally, we study the effect of ion bombardment via external rf substrate biasing.

6.1.2 Experimental Details

The a-Si:H thin films have been deposited on c-Si wafers (prime wafer, 500 Ű- 550 μm) with about 2 nm of native oxide, as determined by spectroscopic ellipsometry (SE). Our RTSE measurements were performed using a J. A. Woollam Co., Inc. M-2000F rotating compensator spectroscopic ellipsometer. In our RTSE data analysis, we follow a standard procedure for RTSE data analysis is described in more detail by Van den Oever et al. [63]. Koh et al. [66] have shown that the roughness obtained from SE measurements is linearly related to the rms roughness obtained from AFM measurements over a range of bulk film thicknesses up to at least 6500 Å, demonstrating that SE is a viable method for surface roughness analysis for the film thickness range utilized in this study. RF substrate biasing was generated with a rf generator (Coaxial RFGS 100 SE); the applied rf power was 60 W, leading to an average dc substrate voltage of 21 V. There was a delay between start of the deposition and activation of the substrate biasing of about 5 s, equivalent to approximately 5 Å of film growth.

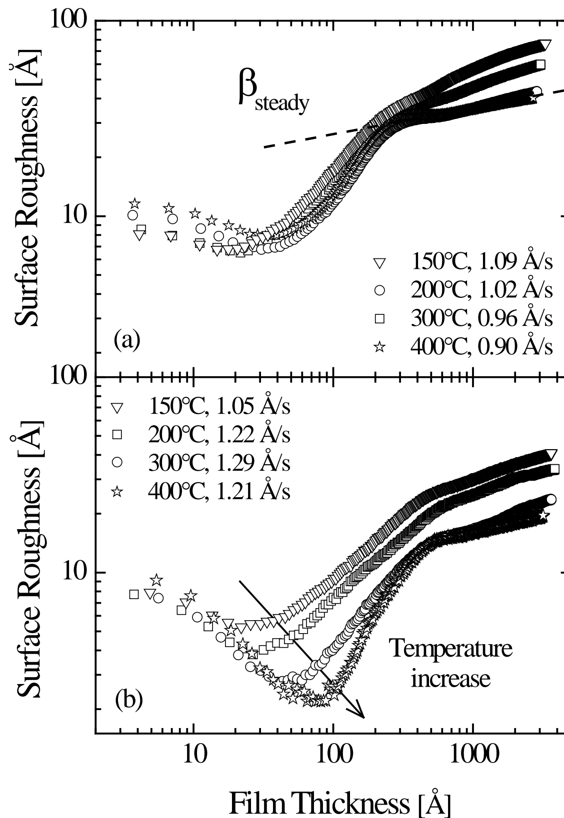

Figure 6.1 Surface roughness layer thickness development as a function of bulk film thickness for depositions (a) without substrate biasing and (b) with substrate biasing.

6.1.3 Results

The development of the surface roughness layer, d_s, versus the bulk film thickness, d_b, for depositions without substrate biasing can be seen in Fig. 6.1 (a), and for depositions with substrate biasing in Fig. 6.1(b)), in both cases for a temperature range of 150 Ű- 400°C. Substrate biasing leads to an increase in deposition rate of about 15% Ű- 20% (see legend) in Fig. 6.1(a) and 6.1(b)). It was concluded by Hoefnagels et al. [106] that this increase is caused by the production of additional SiH_3 radicals.

For all depositions, with and without biasing, we can identify several phases.

- Phase I: A phase in which the roughness decreases until a minimal roughness is reached. Commonly this initial roughness is attributed to nucleation on the oxidized silicon wafer surface [69]. At the onset of film growth, coalescence of neighboring nuclei occurs and smoothening mechanisms result in considerable mass transport into the surface valleys between adjacent nuclei, leading to the roughness reduction. For unbiased deposition in Fig. 6.1(a), the lack of temperature dependence of the negative slope suggests that surface processes are virtually temperature independent or have extremely low activation energy. Also for biased depositions in Fig. 6.1(b) the negative slope appears to be temperature independent, but the duration of phase I increases with increasing temperature and a lower roughness in the minimum at higher bulk film thicknesses is reached.

- Phase II: A subsequent phase with a strong roughness increase. The onset of this phase is in between 20 and 100 Åbulk film thickness, depending on the bulk thickness at which the minimum occurs. This onset might be related to the a-Si $\rightarrow$ a-Si roughening transition introduced by Collins et al. [69]. Also this phase shows no strong temperature dependence for unbiased depositions. For biased depositions the roughening is stronger for higher substrate temperatures. When analyzing the surface roughness development in this phase according to the dynamic scaling theory, we can determine the growth exponent β [122]. A growth exponent of 0.5 is obtained under complete absence of any smoothening or roughening conditions, simply due to the random nature of the growth flux distribution. Consequently, a β-value below 0.5 is a direct result of the presence of smoothening mechanisms. The peculiarly strong roughening in this phase with $\beta > 0.8$ (not shown) indicates the dominance of roughening mechanisms. A comparable strong roughening early in the deposition was previously reported e. g. for HW-CVD depositions [72], as well as a strikingly similar roughness development throughout the deposition in general. In other literature, strong roughening, either throughout or in certain stages of film growth, has been reported for amorphous thin-film deposition in recent years, ranging from $\beta = 0.7 - 1.5$, both in experiment and in simulation [71, 72, 123–132]. Typical mechanisms for strong roughening include shadowing [124, 125, 131, 132], columnar growth [129], or diffusion barrier steps [130].

- Phase III: The steady growth phase with the β-value labeled β_{steady}. At a film thickness between 300 and 400 Å the strong roughening levels off and the film enters the steady growth phase for the rest of the deposition. When analyzing the surface roughness development in this phase

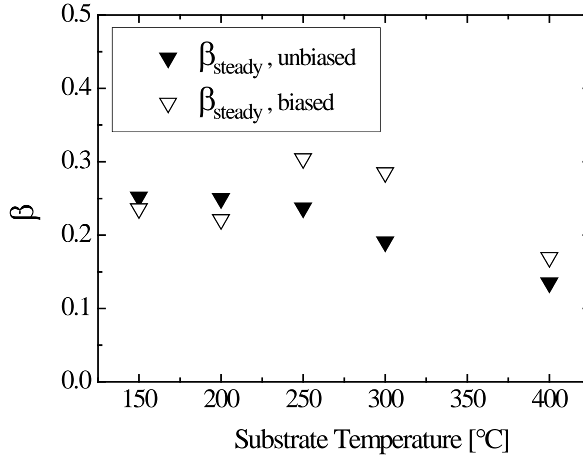

Figure 6.2 Growth exponent β_{steady} determined from the roughness development in the steady growth phase shown in Fig. 6.1.

according to the dynamic scaling theory (see, e.g., Ref. [128]), we can determine the growth exponent β from the relation $d_s \sim t^{\beta}$ with t the deposition time. As explained above, a β-value below 0.5 as we observe in this phase ($\beta_{steady} \sim 0.25 - 0.15$, Fig. 6.2) is a direct result of the presence of a smoothening mechanisms. We can observe a weak temperature dependence for β.

The reduction of the surface roughness minimum in the coalescence phase at the transition from phase I to phase II seems to be enhanced by substrate biasing at elevated temperatures, resulting in smoother surfaces at higher temperatures in the roughness dip, as can be seen in Fig. 6.1(b). However, we suggest that surface smoothening in this phase is not due to a reduction of the actual surface roughness, but is in fact related to the presence of a hydrogen rich or low density layer in the early growth phase for unbiased depositions and its removal/densification under substrate biasing. The formation of a hydrogen rich/low density layer in the early growth phase has been reported before, e.g., by Fujiwara et al. [133] and Drevillon et al. [134]. It has a significantly lower density and dielectric function than the bulk a-Si:H network and can thus be misinterpreted as surface roughness by SE measurements. This was also demonstrated by Fujiwara et al. [135] and a hydrogen concentration of ∼25% was estimated for the initially deposited monolayers. The removal or densification of this layer by ion bombardment can explain what is misinterpreted as a reduction in surface roughness in the coalescence phase by the SE. Due to the broad ion energy distribution obtained with rf substrate biasing

both ion-surface atom interactions as well as ion-subsurface atom interactions, which require higher energetic ions, could lead to this densification. From further SE analysis we can see that indeed the surface roughness layer in this phase shows a void fraction of about 33% for unbiased depositions and around 42% for biased depositions at 400°C (not shown), indicating that subsurface layers with very low density might be misinterpreted as surface roughness for unbiased depositions, and is removed by substrate biasing at elevated temperatures. The temperature dependence of this effect suggests that also thermally activated mechanisms are involved and in fact required in order to lead to the removal/densification of the hydrogen rich/low density layer, e.g., by facilitating the abstraction of hydrogen atoms from surface or subsurface layers. Within this interpretation we must conclude that thermal energy alone, however, is not sufficient and ion bombardment is required, as can be deduced from Fig. 6.1(a) where a reduction in roughness at the roughness minimum cannot be observed even at 400 °C.

The presence of smoothening mechanisms in phase I is obvious, demonstrated by the strong decrease in roughness during that phase. Dominance of smoothening mechanisms in the steady growth phase, phase III, is less obvious, but can be deduced from dynamic scaling theory as discussed above. The presence of extraordinarily strong roughening in phase II, however, indicates a temporary reduction of smoothening processes. This observation is not compatible with surface diffusion-driven smoothening. If surface diffusion is the main smoothening mechanism in phase III, it would require rather long diffusion lengths comparable to the feature size on the surface. However, with such long diffusion lengths any kind of surface features present in phase II would be smoothened and strong roughening should not occur. Consequently, would surface diffusion be dominant in both phase I and III, the presence of phase II would require a strong temporary reduction of radical diffusion at the roughness minimum and its resumption at the beginning of phase III. Such change in radical diffusion is highly unlikely, as there is no change in radical flux arriving at the surface. Alternatively, we might have a very strong roughening mechanism that is only present in phase II, but such a short-term roughening mechanism has not been observed or suggested in literature yet. Therefore we anticipate the presence of strong roughening in phase II implies that surface diffusion cannot be the dominant smoothening mechanism in a-Si:H film growth.

Re-emission is an alternative nonlocal mass transport mechanisms that can explain smoothening on large lateral length scales. In the re-emission model a particle with a sticking coefficient < 1 can be re-emitted from surface features upon impact and transported deeper into the surface valley, thus transporting mass into surface valleys. Re-emission is related to the shadowing effect where particles with high sticking coefficients lead to enhanced growth of surface pro-

trusions over surface valleys by receiving more growth flux under a non-normal angular distribution. A change in balance between shadowing and re-emission as dominant roughening and smoothening mechanisms during film growth is able to explain β-values in a wide range from 0.1 to > 1 [136]. It can therefore explain both the dominant roughening in phase II and dominant smoothening in phase III by implying a change in the balance between re-emission as smoothening effect and shadowing as a roughening effect. Re-emission is a temperature independent process for growth precursors with temperature independent sticking coefficients as determined for SiH_3 precursors [106].

However, also with re-emission as dominant mass transport mechanism, the origin of the strong roughening in phase II cannot easily be explained, as the nature of the shift in balance between re-emission and shadowing needs to be identified. It might be related to the fact that re-emission requires a certain inclination of the surface slopes before it can act as smoothening mechanism. Also the formation of cusps at surface feature edges, as suggested by Singh et al. [32], might play a role here. They conclude that the formation of cusps can cause the decay of surface roughness for radicals with low sticking coefficients.

6.1.4 Conclusions

In conclusion, we have investigated the temperature dependence of surface roughness evolution for a-Si:H thin film deposition with and without external rf substrate biasing. The effect of external rf substrate biasing on the coalescence phase is discussed and a removal/densification of a hydrogen rich/low density layer is suggested to explain the observed roughness development in this phase. Following a discussion of two distinct phases in the roughness development of bulk film growth we suggest that alternative, nonlocal growth mechanisms, like the re-emission effect, could play an important role in a-Si:H film growth.

6.2 Influence of Hydrogen Dilution on the Surface Roughness Evolution

6.2.1 Introduction

The growth mechanism of hydrogenated amorphous silicon (a-Si:H) is still an ongoing subject of scientific debate. It is well recognized that hydrogen dilution plays an important role in the preparation of a-Si:H films for RF plasma-enhanced chemical vapor deposition (PECVD). Stable material with the best electrical properties for application in thin film silicon solar cells is obtained at higher hydrogen dilution, just before the onset to microcrystalline film growth [69].

For the expanding thermal plasma chemical vapor deposition (ETP-CVD) technique utilized in this work it is well understood how the composition of the growth flux is related to the hydrogen dilution. When diluting the plasma with hydrogen, SiH_3 remains the dominant growth precursor, however, due to secondary hydrogen abstraction reactions the contribution of SiH_2, SiH and atomic Si radicals to the growth strongly increases with increasing hydrogen dilution [137]. Since these radicals have a much higher sticking probability compared to SiH_3, this change in the composition of the growth flux leads to an increase of the average sticking probability to higher values with increasing dilution, and thus a lower surface mobility. In this work we investigate the film growth as a function of growth flux composition, utilizing the previously mentioned dependence of the growth flux composition on hydrogen dilution.

6.2.2 Experimental Details

In the ETP-CVD technique, an Ar-H_2 plasma is created in the arc, where the gases are injected into a 2.5-mm diameter channel formed by six isolated copper plates [46]. A DC-discharge is sustained between three cathodes and a grounded copper plate. The precursor gas silane (SiH_4) is injected into the plasma beam via an injection ring, which reacts with the atomic hydrogen created in the Ar-H_2 plasma. Abstraction of hydrogen atoms from the SiH_4 molecule results in formation of the radicals that result in film growth on the substrate surface.

For all depositions reported here, the Ar flow was 530 sccm, H_2 flows are 160 sccm and 110 sccm in the arc respectively the nozzle. The SiH_4 flow in the injection ring is varied between 80-5 sccm. This results in a hydrogen dilution $R = [H_2]/[SiH_4]$ in the range of 3.4 - 56. The substrate temperature is constant at 300°C. The films have been deposited on c-Si wafers (prime wafer, 500-550 nm, 2 nm native oxide).

Atomic Force Microscopy (AFM) measurements were carried out using a NT-MDT AFM set-up in tapping mode. Images of the size of 10 μm $\times$ 10 μm were recorded. Our RTSE measurements were performed using a J. A. Woollam Co., Inc M-2000F rotating compensator spectroscopic ellipsometer. In our RTSE data analysis we follow a procedure similar to the one established by Van den Oever et al. [63], unless specified otherwise. The dielectric function of the deposited films are modeled by the parameterized Tauc-Lorentz formalism. Surface roughness is implemented using the Bruggeman effective medium approximation (EMA) with 50% voids [135]. Unless indicated otherwise, the only fitting parameters are the bulk film thickness d_b and the surface roughness layer thickness d_s.

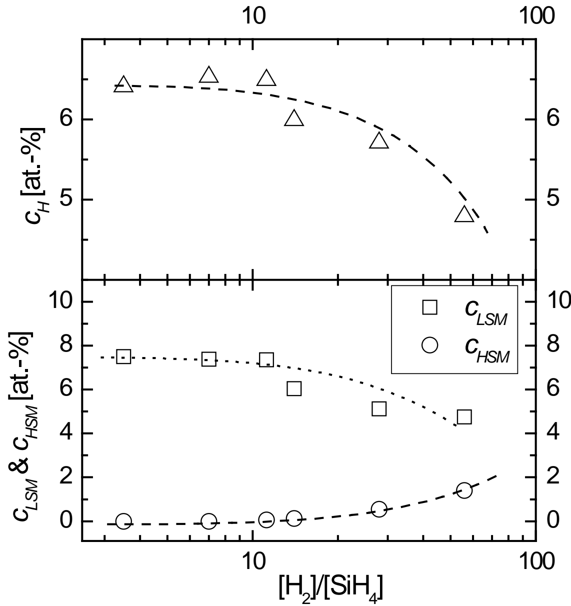

Figure 6.3 Total hydrogen concentration c_H and hydrogen concentration associated to voids c_{HSM} and vacancies c_{LSM} as a function of hydrogen dilution.

6.2.3 Results & Discussion

Influence of Dilution

The effect of hydrogen dilution on the hydrogen bonding configuration is demonstrated by FTIR results in Fig. 6.3. The total hydrogen concentration c_H is constant up to $R = 10$ and decreases for $R > 10$. The concentration of hydrogen associated to vacancies (c_{LSM}) and to voids (c_{HSM}) is constant for $R < 10$. For $R > 10$ we see that the contribution of voids increases and at the same time hydrogen associated to vacancies decreases. We relate this increase in void volume fraction to the transition of the plasma-beam composition from low- to high-sticking precursors. These particles have a lower surface mobility and can lead to conditions where shadowing (i. e. shading of surface valleys by surface protrusions and preferential growth of the latter) has a significant influence on the development of the surface morphology, resulting in columnar growth. Contrary to conventional RF PECVD, strong hydrogen dilution in our remote plasma deposition leads to growth of material with voids and thus reduced bulk density.

The evolution of the surface roughness layer thickness d_s as obtained

from RTSE measurements is shown in Fig. 6.4 for different hydrogen dilutions. All curves show a similar behavior and consist in general of three phases. The initial reduction in surface roughness is related to the smoothening after coalescence of nuclei [69]. Following the roughness minimum, we observe a stronger roughening phase, which shows a clear dependence on the hydrogen dilution. The roughness built in this phase is about 50 Å for high dilutions and only 10 Å for low dilutions. Such a strong roughening phase has been reported before by RTSE studies [72, 110]. Subsequently film growth continues in the steady growth phase, in which most of the bulk film growth occurs. We observe a second roughness minimum for higher dilutions before the onset of the steady growth phase, the origin of this minimum is unknown at present. In the steady growth phase all depositions show a similar RTSE roughness evolution, independent of R. The early growth phase up to 100 nm thickness is shown again in Fig. 6.5. Here the film growth rate is normalized to the average film growth rate of the whole deposition, along with the surface roughness layer thickness, both as function of deposition time, normalized to the time it takes to deposit 100 nm of a-Si:H. For both dilutions, at the beginning of the deposition we clearly see the nucleation phase with strong roughness increase at no film growth. Film growth starts at the first maximum of the roughness, when coalescence of nuclei leads to the formation of a closed film. Subsequently the growth rate reaches above-average values while the film roughness is reduced. The subsequent strong roughening phase yields below-average growth rates again, with more growth at surface hills then at surface valleys. After the strong roughening we observe the steady growth phase with average rates and slight continuous roughening. While we observe similar trends at both dilutions, they are clearly more enhanced at high dilution where stronger roughening occurs after the coalescence phase. This plot demonstrates well how in phases with strong roughening, more growth occurring on surface hills leads to below-average growth rates, whereas more growth occurring on surface valleys leads to smoothening and above-average growth rates.

The inset in Fig. 6.4 compares the RTSE roughness d_s to the double root-mean-square (rms) roughness obtained from AFM measurements at different times of the deposition. The AFM measurements were carried out for two dilution conditions, $R = 56$ and $R = 3.5$. We observe a linear relationship with a similar slope for both conditions, 1.4 ± 0.26 for $R = 56$ and 1.6 ± 0.32 for $R = 3.5$. Such a linear relationship between AFM and SE measurements has previously been reported by Koh et al. [66], with comparable slopes as we obtain (1.5). The offset of the fit for $R = 3.5$ is similar to literature reports (this work: ± 0.7 nm, Koh et al.: ± 0.4 nm), but is significantly different at high dilution, where we obtain a 4-nm offset. Samples of AFM scans can be seen in Fig. 6.14 and Fig. 6.15 at the end of this chapter for both dilution conditions and

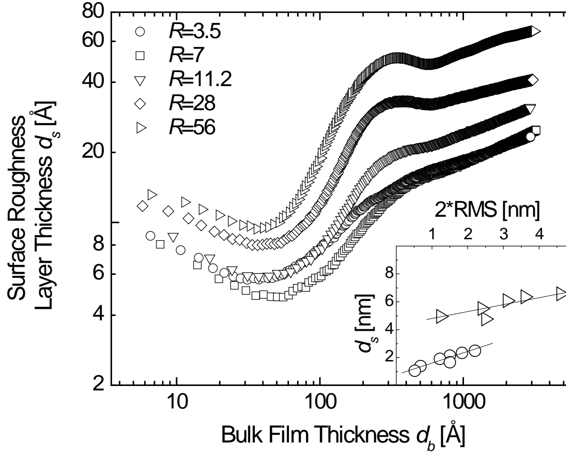

Figure 6.4 Evolution of the surface roughness layer thickness d_s as a function of bulk film thickness d_b for different R. The inset shows the surface roughness layer thickness d_s vs. the double rms surface roughness obtained from AFM measurements for two different hydrogen dilutions, $R = 3.5$ (circles) and $R = 56$ (squares).

different deposition times.

The roughness layer thickness obtained from RTSE for high dilution conditions is remarkably higher than the roughness obtained from AFM measurements. This suggests that the relationship is only correct for dense material as obtained by Koh et al. [66], and in this work for low dilution conditions. Assuming that rms roughness is a good representation of the physical roughness present at the surface, different effects can be considered that could lead to an over-interpretation of the roughness layer thickness by RTSE. We suggest that the difference is related to the presence of a hydrogen rich low density overlayer, which typically has a much lower density than the bulk film. Such a layer can be interpreted as part of the roughness layer by RTSE, as was demonstrated before [135]. This overlayer typically consists of surface hydrides (SiH_x with $x \leq 3$), of which only the higher hydrides are preferentially etched by atomic hydrogen [27]. At higher R, we suggest that the increasing contribution of hydrogen deficient radicals to the growth flux results in an overlayer dominated by lower hydrides, which are etched weaker then higher hydrides [27]. This reduced etching results in a thicker hydrogen rich/low density overlayer, which is then interpreted as part of the roughness layer by RTSE. The thickness of the hydrogen rich/low density layer can be calculated, simply from the difference between the double rms roughness value and d_s. We obtain a thickness of 1.9 nm for high dilution and 0.3 nm for low dilution in the steady growth

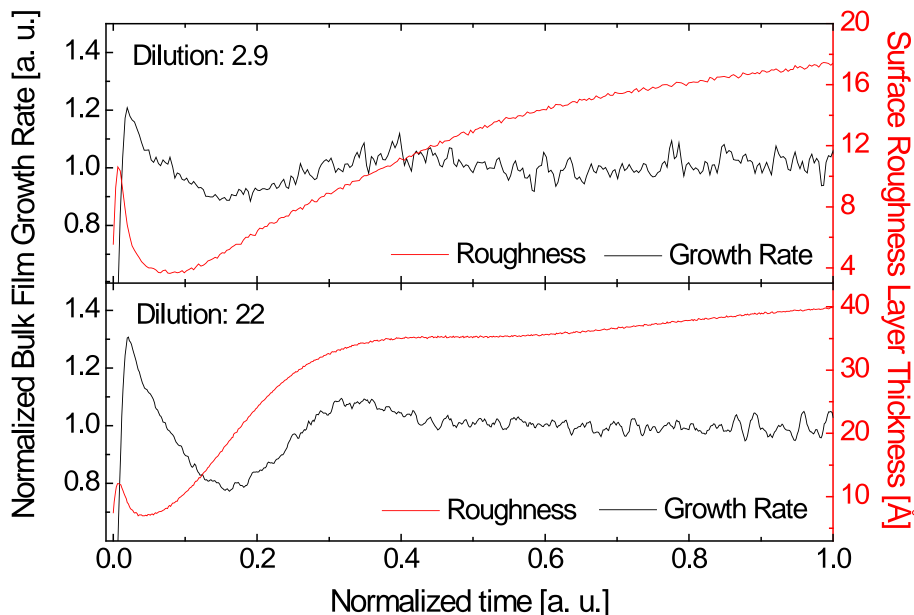

Figure 6.5 The film growth rate normalized to the average growth rate over the whole deposition and the surface roughness layer thickness are shown vs. time normalized to the time when the film reached 100 nm thickness. Both are shown for two dilutions, 2.9 and 22.

phase. Furthermore, we suggest that the strong roughening phase is related to the formation of this overlayer, and at the onset of the steady growth phase an equilibrium between overlayer formation and hydride etching is reached. Subsequently the overlayer thickness remains constant.

However, two experimental observations conflict with this idea. Firstly, the total hydrogen concentration c_H is reduced for $R > 10$, whereas the overlayer thickness increases. The reduced c_H might be related to an increased removal of excess subsurface hydrogen under conditions where hydrogen deficient radicals strongly contribute to the growth flux. Also the more porous structure of a columnar grown film might facilitate the removal of excess hydrogen.

Secondly, a thicker hydrogen rich/low density layer would result in a chemically less reactive surface due to a reduced dangling bond density and thus a higher surface mobility. However, we observe structures that indicate columnar growth at $R > 10$, as can be concluded from Fig. 6.6, where we see TEM images obtained for films deposited at $R = 7$, $R = 28$ and $R = 56$, with the

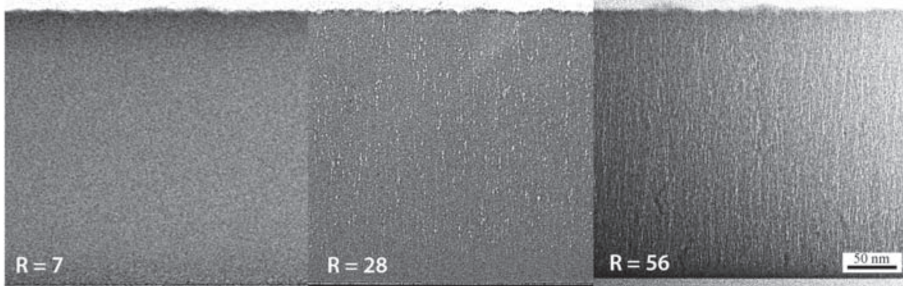

Figure 6.6 TEM images of samples deposited at three different dilutions of 7, 28 and 56. Light elongated structures can be seen at higher dilutions, indicating areas of reduced material density.

c-Si substrate to the bottom and the film growth direction to the top. For $R = 3.5$ we see a homogeneous amorphous structure without any indication of voids or less dense material. For $R = 28$ and $R = 56$ we can see brighter features, which indicate the presence of either voids or regions of material with density below the average bulk density. These structures are elongated in the growth direction of the film, indicating the presence of columnar growth at higher R and therefore a reduced surface mobility under these conditions. This indicates that the dangling bond concentration on the surface is less important for a-Si:H film growth, as frequently suggested by other authors [27, 106]. As mentioned above, the transition to higher sticking radicals can play a role. These particles have a lower surface mobility and their incorporation into the film might be independent of the presence of dangling bonds on the surface. Additionally, other growth mechanisms like direct insertion of radicals into stretched bonds can play a role. The concentration of stretched bonds might be higher for a thicker hydrogen rich/low density overlayer, thus reducing the surface mobility at higher R. It is worth noting that columnar structures are not visible in the first 50 nm and the film appears to be denser.

The effect of a change in dilution during deposition on the surface roughness evolution obtained from SE can be seen in Fig. 6.7. For both depositions shown in (a) and (b) respectively the deposition was started at a dilution of $R = 28$ and then switched to $R = 7$ without stopping the deposition after (a) 25 minutes and (b) 5.5 minutes. The dielectric function was determined separately for the two deposition phases. In both cases we can see that a change in dilution results in an almost immediate reduction of SE surface roughness. The fast reduction in roughness inicates that this is the result of a fast change in chemical structure of the surface and not a change in actual physical roughness which should take significantly longer. This suggests a change in thickness of a surface layer with reduced density as proposed above.

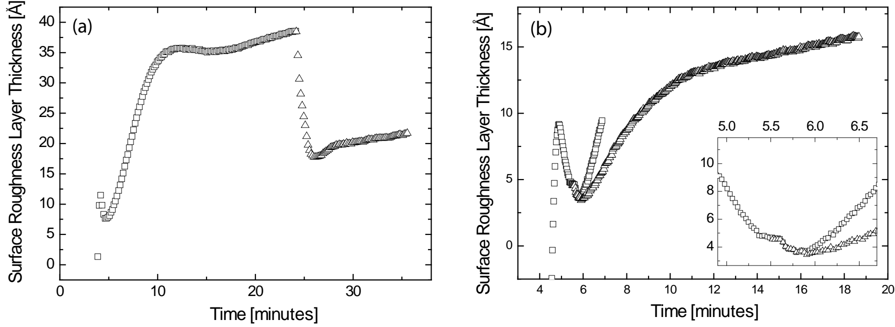

Figure 6.7 The surface roughness layer thickness as a function of time for two depositions at a dilution of $R = 28$. In both cases the dilution was changed to $R = 7$ after (a) 25 minutes and (b)5.5 minutes. The inset in (b) shows a closeup of the time between 5 - 6.5 minutes where the transition occurs.

In order to gain more insight into the film density evolution during deposition we have refitted the SE data with a parameterized Tauc-Lorentz model for the a-Si:H layer with the band gap as variable parameter. In this case the band gap acts as a measure for the material density, since it typically increases with c_{HSM}, which is a measure for the void fraction in a-Si:H films [115]. In Fig. 6.8(b) and (c) we see the surface roughness d_s and the band gap E_g as a function of bulk film thickness, respectively, for low and high dilutions. Additionally a small part of the TEM images in Fig. 6.6 is shown again in 6.8(a). The band gap varies strongly for very thin films with $d_b < 50$ nm. For ultra thin films with $d_b < 2$ nm we see a band gap > 2eV. A similar result has for example been reported by Van den Oever et al. [63] and is associated to a quantum confinement effect at very low thicknesses. The inset shows $\Delta E_g = E_g - E_{g,min.}$ for $d_b < 50$ Å , along with a fit of the band gap to the equation for 1D quantum confinement, $E_g - E_{g,min.} = C/(d_b)^2$, with C the confinement parameter. From the fit we obtain $C = 94 \pm 2.23$ eVÅ^2 for both dilution conditions, which is in a comparable range to the result of Van den Oever et al. [63] (120 $\pm$ 4 eVÅ^2).

Subsequently, for $R = 56$ we see a decrease of the band gap below the bulk value of 1.6 eV, to a minimum value of 1.3 eV, followed by a continuous increase until the bulk value is reached at 50 nm film thickness. As indicated by the dashed vertical lines, this variation in band gap overlaps well with the region where we observe a denser film in the TEM image in Fig. 6.8(a) and the phase with the strongest increase in roughness in Fig. 6.8(b). For $R = 3.5$ we see a similar trend for the band gap, with a similar minimum for the band gap around 1.3 eV, but a much lower bulk value around 1.45 eV. This trend suggests that we obtain much denser films during the initial phase of

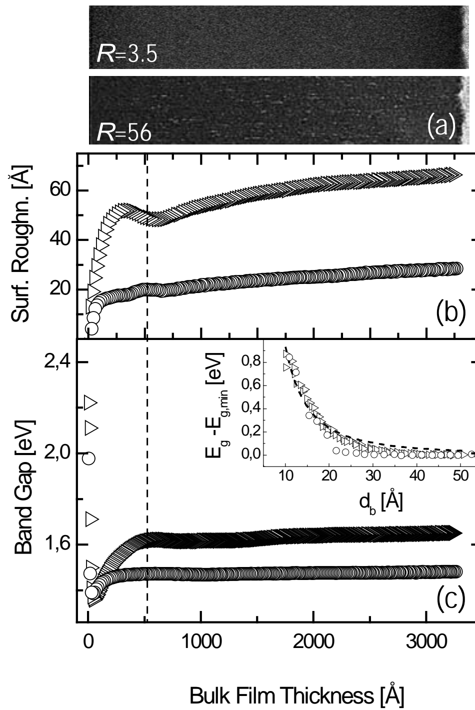

Figure 6.8 (a) TEM images of a samples deposited at dilutions of $R = 3.5$ (top) and $R = 56$ (bottom). (b) The surface roughness and (c) the band gap evolution as a function of bulk film thickness for samples deposited at $R = 3.5$ (circles) and $R = 56$ (triangles). The inset in (c) shows the difference in band gap to the minimum band gap, $E_g - E_{g,min.}$, the line represents a fit of these data to 1D quantum confinement, following a $1/(d_b)^2$ relationship.

film growth in which the hydrogen rich/low density overlayer is formed. The transition phase lasts for 30-50 nm of bulk film thickness, after which growth of less dense bulk film is observed. We suggest that denser films are obtained while the hydrogen rich/low density layer is still forming, which indicates a higher surface mobility under these conditions. The increase in band gap then corresponds to a transition to growth of a less dense film, which we attribute to a transition to conditions with a lower surface mobility.

Both the SE fits in Fig. 6.8 and TEM results in Fig. 6.6 suggest that the void concentration is lower in the initial phase of film growth and increases with increasing distance from the substrate-a-Si:H interface. This observation can also be investigated with SE modelling when void fraction is implemented as a parameter, as can be seen in Fig. 6.9. For these fits, the dielectric function of the a-Si:H was determined under consideration of the voids in the material. In

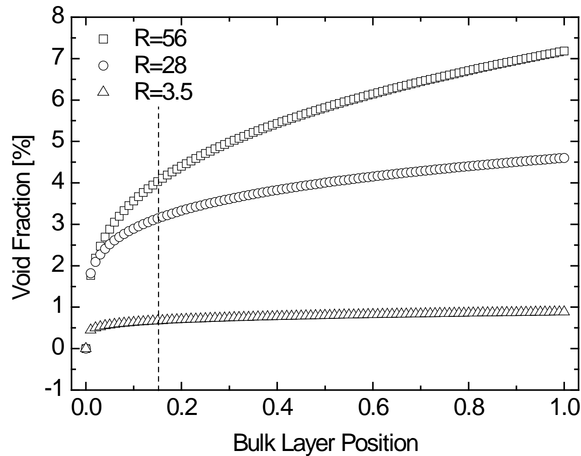

Figure 6.9 The void fraction versus the relative bulk film position in films with three different dilution. The bulk position corresponds to the substrate - a-Si:H interface at 0 and the a-Si:H surface at 1.

this way the dielectric function of a-Si:H is obtained as if no voids were present in the film. Then the voids are reintroduced into the model as fitting parameter. The void fraction as function of bulk layer position is then plotted in Fig. 6.9. Bulk layer position in this case indicates the relative position in the film where 0 is at the substrate surface and 1 at the film surface. The void fraction can only vary following a simple exponential function, but the obtained distribution shown in the Figure gives a relatively good confirmation of the trends seen in both Fig. 6.8 and 6.6. While for $R = 3.5$ the void fraction stays $< 1\%$ we obtain a significantly higher void raction at higher dilutions. The distribution is similar to the distribution indicated in Fig. 6.8 and 6.6, with very low void fractions close to the substrate and a continues increase towards the film surface.

Influence of PSB

As established in the previous section it appears that a hydrogen rich/low density layer leads to an overestimation of the surface roughness layer thickness from SE measurements. In this section we investigate the influence of pusle-shaped biasing on these layers. Depositions conditions were similar to the previous section, limited to two dilution conditions, $R = 7$ and $R = 56$. PSB was applied at voltages up to 50 V. Contrary to PSB experiments reported in Chapter 4, these depositions were carried out at much lower growth rates ~ 1 Å/s and higher substrate temperatures of 300°C. The substrate temperature had to be kept constant during these longer depositions and therefore the thermocouple

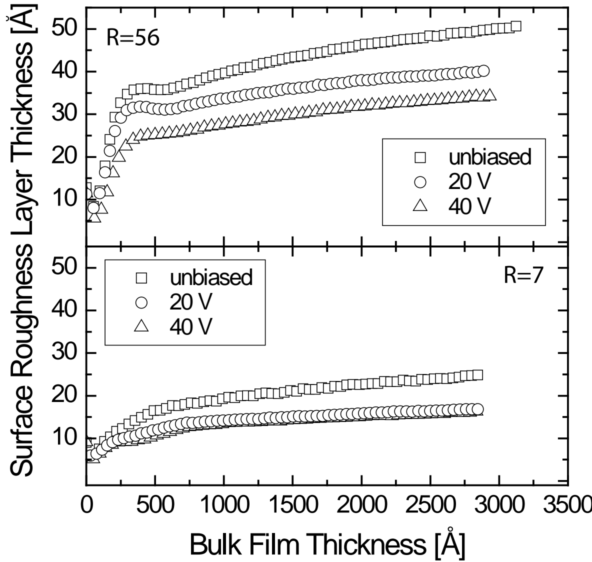

Figure 6.10 The surface roughness layer thickness versus bulk film thickness is shown at $R = 56$ (top) and $R = 7$ (bottom) respectively. Films were deposited without biasing and at V_{front} of 20 V and 40 V.

could not be disconnected, thus limiting the PSB to 50 V. At higher voltages strong interference between the thermocouple and the PSB signal occur.

The surface roughness evolution versus bulk film thickness for $R = 56$ and $R = 7$ is shown in Fig. 6.10 in the top and bottom figure, respectively, for unbiased, 20 V and 40 V biased depositions. In both cases ion bombardment leads to a considerable decrease in surface roughness. For $R = 56$ the roughness in the steady growth phase is reduced until 40 V bias and the reduction is mainly observed in the initial growth phase. At 50V biasing (not shown) no further smoothening was observed. Roughening in the steady growth phase $>$ 500 Å bulk film thickness seems unaffected by ion bombardment. For $R = 7$ the minimum roughness is obtained already at 20 V and no further smoothening is observed at 40 V. Also here the roughening in the steady growth phase seems largely unaffected by ion bombardment. Assuming that the roughness decrease can be attributed to densification of the hydrogen rich/low density layer introduced in the previous section, the described reduction in surface roughness upon biasing can be used to estimate the thickness of this surface layer. From the reduction in d_s at $d_b = 3000$ Å upon substrate biasing in Fig. 6.10 we can estimate that the hydrogen rich/low density layer has a thickness of 1.5 nm

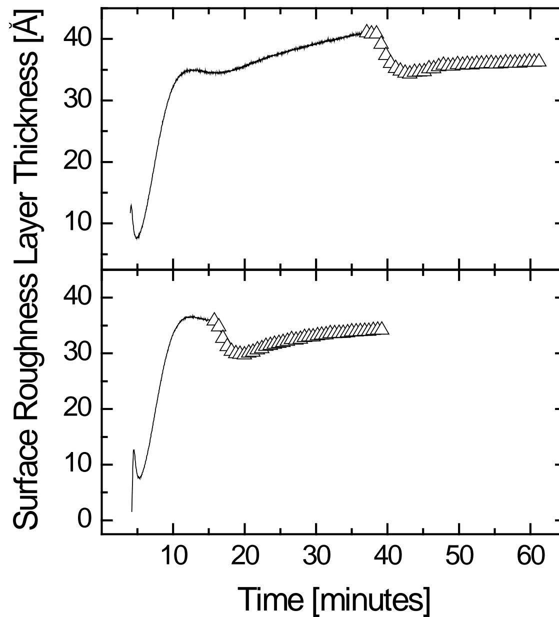

Figure 6.11 The surface roughness layer thickness versus bulk film thickness is shown at $R = 56$ for delayed PSB of 20 V starting after 30 minutes (top) and 10 minutes (bottom).

for $R = 56$ and 0.8 nm for $R = 7$. This is comparable to the values obtained in the previous section from comparison of AFM and SE roughness where we obtained 1.9 nm at high dilution and 0.3 nm at low dilution.

In Fig. 6.11 the roughness evolution for 20 V biasing at $R = 56$ is shown for delayed PSB. In this case the deposition was started without biasing and after 30 minutes (top) and 10 minutes (bottom) biasing was started, indicated by the triangular symbols in the plot. The roughness decreases quickly after biasing started, indicating that the densification of the low density layer and/or hydrogen removal from the hydrogen rich/low density layer occurs quickly. Especially from the top figure we can conclude that after the initial drop in roughness due to ion bombardment the roughness evolution is not significantly affected by ion bombardment.

The results of FTIR analysis are shown for $R = 56$ and $R = 7$ in Fig. 6.12. In Fig. 6.12(a) the total hydrogen concentration c_H is shown and for both $R = 56$ and $R = 7$ and c_H increases slightly with V_{front} for both dilutions. The increase is slightly stronger for the high dilution samples. This is in agreement with results on PSB from Chapter 4 where the same increase in c_H was observed

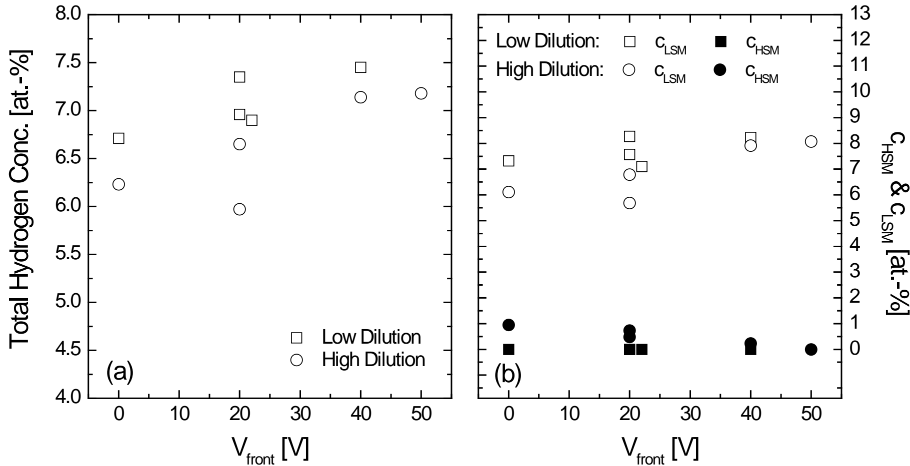

Figure 6.12 FTIR analysis of samples deposited at different PSB substrate voltages V_{front} for $R = 56$ and $R = 7$. The total hydrogen concentration is shown in (a) and the concentration of hydrogen associated to vacancies c_{LSM} and voids c_{HSM} in (b).

with increasing V_{front} for a wide range of voltages. The development of c_{LSM} and c_{HSM} is shown in Fig. 6.12(b). For the low dilution sample with $R = 7$, c_{HSM} was very low and the material can be assumed to be virtually void free, in agreement with the previous section. The increase in c_H is thus entirely due to the the increase in c_{LSM}. As shown in Chapter 4, this increase is presumably the result of subsurface atom displacement upon ion bombardment and subsequent hydrogen attachment to the resulting dangling bond. For the high dilution with $R = 56$ on the other hand, a low nanovoid fraction is present in the material and $c_{HSM} \sim 1\%$ for unbiased deposition. With increasing V_{front}, c_{HSM} decreases until the material appears to be void-free at $V_{front} = 50$ V. This has also been observed and explained in Chapter 4. The increase in c_{LSM} is thus stronger compared to depositions at $R = 7$ since both the decrease in c_{HSM} as well as the above mentioned mechanisms of subsurface atom displacement lead to an increase in c_{LSM}.

The dependence of the refractive index in the infrared is shown in Fig. 6.13 as function of V_{front} for both dilution series and serves here as a measure for the material density. For $R = 7$ the refractive index is independent of V_{front}, a very slight decrease can be seen which is presumably a result of a decrease in material density due to a slight increase in c_H as shown in Fig. 6.12(a). For $R = 56$ the refractive index increases with V_{front} which can be attributed to the decrease in nanovoid fraction in the material as deduced from c_{HSM} in Fig. 6.12(b).

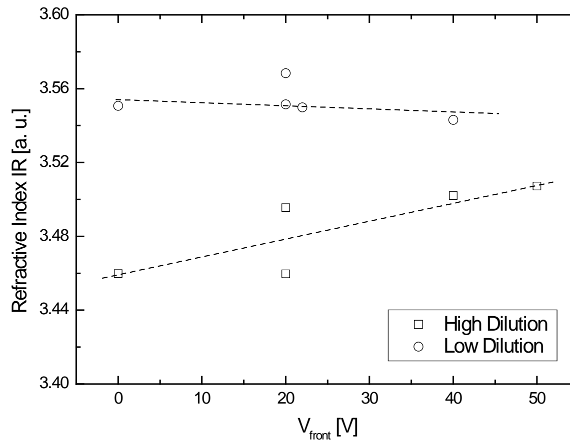

Figure 6.13 The refractive index in the infrared as obtained from FTIR measurements is shown for low dilution ($R = 7$) and high dilution ($R = 56$) as function of substrate voltage V_{front} during PSB. The lines serve as guide to the eye.

6.2.4 Conclusions

We observe a discrepancy in the surface roughness analysis between RTSE and AFM measurements. A mechanism that involves the formation of a hydrogen rich/low density overlayer and etching of higher hydrides in this overlayer is suggested to explain this observation. At higher hydrogen dilutions, we obtain a thicker overlayer dominated by lower hydrides. RTSE interprets this overlayer as additional surface roughness and consequently overestimates the surface roughness for higher dilutions. What appears to be an initial strong roughening phase is related to the built-up of this overlayer. In the phase where the overlayer is formed, we obtain denser films compared to the bulk film. This is related to a transition in surface mobility. From additional PSB experiments at two different dilutions we conclude that the hydrogen rich/low density layer is densified by the induced ion bombardment and/or excess hydrogen is removed. Apart from this densification roughening during the steady growth phase seems not to be not affected by ion bombardment.

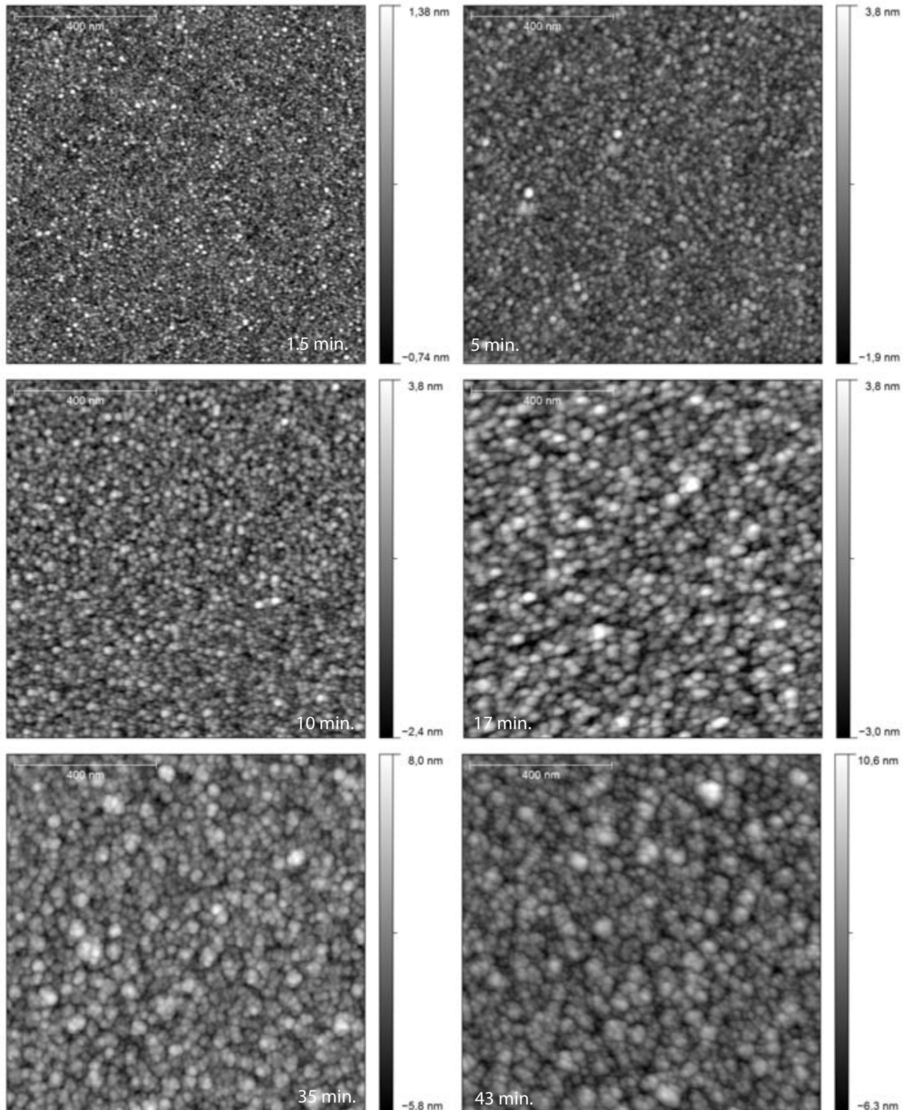

Figure 6.14 AFM scans of samples deposited at low dilution with $R = 3.5$ for different deposition times as indicated in the figures. All scans have a $1 \times 1\mu$m scan size at a resultion of 512×512.

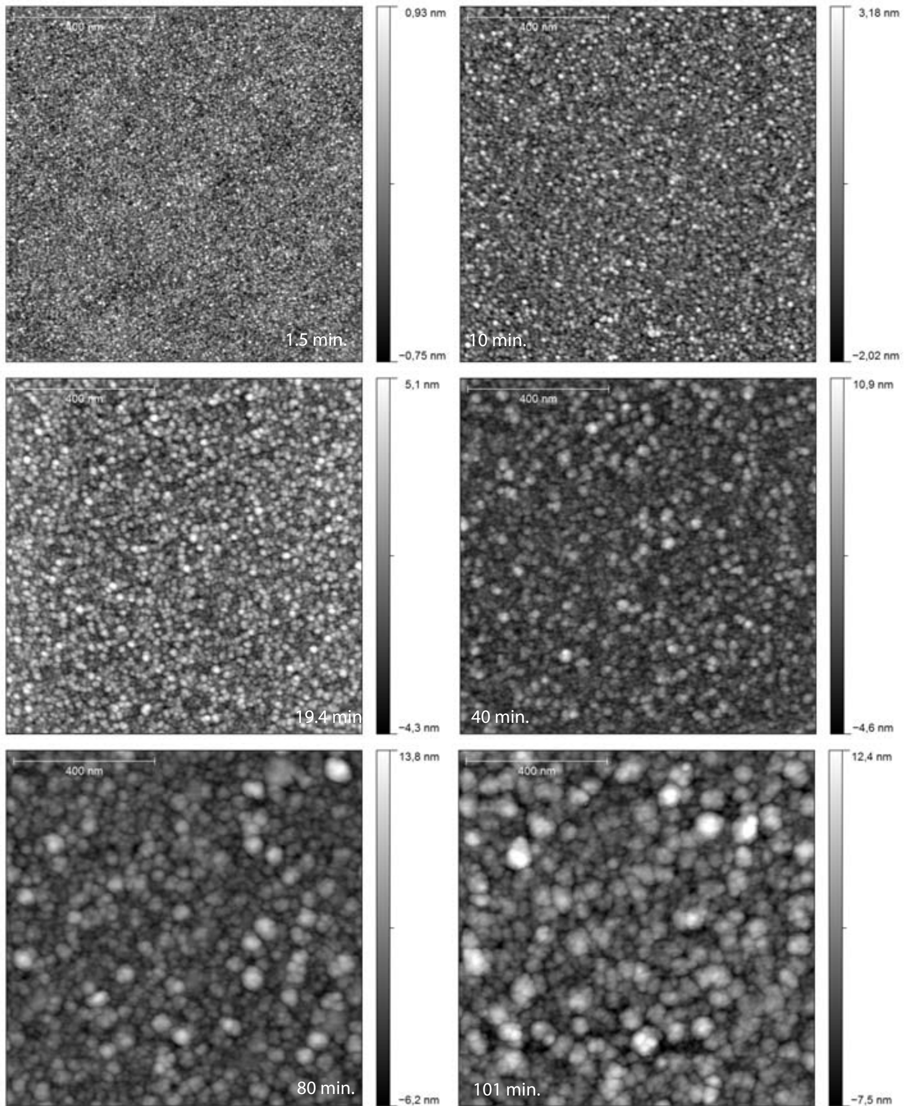

Figure 6.15 AFM scans of samples deposited at low dilution with $R = 56$ for different deposition times as indicated in the figures. All scans have a $1 \times 1\mu$m scan size at a resultion of 512×512.

Chapter 7

General Conclusions

Hydrogenated amorphous silicon (a-Si:H) thin films have been deposited with the ETP-CVD technique under various deposition conditions. Main goal of this work was to deposit solar-grade material at high growth rates of 1 nm/s and low substrate temperatures of 200°C. The results discussed in chapter 4 and 5 show that significant progress towards this goal has been achieved, as demonstrated by solar cells with $> 7\%$ initial efficiency at a growth rate of 1 nm/s and substrate temperatures between 200 – 180°C for the intrinsic layer. To achieve this we have utilised two types of substrate biasing, sinusoidal RF biasing and pulse-shaped biasing, with focus on the latter. Both biasing techniques result in ion bombardment of the film surface during deposition.

Both biasing techniques enable the deposition of solar-grade intrinsic a-Si:H at substrate temperatures below the 350°C required for unbiased deposition. In chapter 3 we demonstrate how RF substrate biasing leads to the growth of vacancy-dominated material up to 50°C below the temperature required for unbiased deposition. This conclusion is based on FTIR analysis with focus on c_{crit}, the hydrogen concentration where a transition form vacancy- to void-dominated material occurs. We investigated the dependence of c_{crit} on the reactor pressure and observed that an increase in reactor pressure lead to a decrease in c_{crit} above 0.24 mbar. This is attributed to an increased contribution of cluster ions and polymers to the growth flux. Ion bombardment at a DC bias voltage V_{DC} of 14 V has hardly any effect on c_{crit}, yet an increase in LSM was observed for all temperatures and pressures. Ion bombardment at $V_{DC} = 20$ V for the high pressure series resulted in an increase of c_{crit} from 9% unbiased to 13% biased, along with a reduction of HSM and a higher LSM. This is attributed to a reduced incorporation of ionic clusters and polymers into the film. A dependence of hydrogen solubility in a-Si:H on reactor pressure and

substrate biasing could be observed, but the thermal stability of these films has not been investigated.

The second type of substrate biasing utilized in this work is the pulse-shaped biasing, PSB. As shown in chapter 4, with PSB we are able to obtain accurate control over the ion energy distribution in a range of 0 - 200 eV without the formation of a strong secondary plasma typically present for RF substrate biasing. Control over the ion energy was confirmed by retarding field energy analyzer measurements for conductive substrates, and non-conductive substrates covered with a conductive surface layer which is connected to the sample holder. The presence of negative ions/particles in the Ar-H_2-SiH_4 plasma is deduced from large positive voltages during the discharge pulse.

For intrinsic a-Si:H deposited with PSB at a growth rate of 1 nm/s and substrate temperatures in the range of 180 - 200°C e can distinguish roughly between two regions: region I $<$ 4.8 eV of deposited energy per Si atom (eV/Si atom) and region II $>$ 4.8 eV/Si atom. In region I we observe an increase in material density due to a decrease in nanovoid concentration as deduced from FTIR analysis. At the transition between region I and II around 4.8 eV/Si atom the densest material with low nanovoid concentration is obtained. The increase in material density and the reduction in surface roughness in region I are attributed to an increase in surface mobility of mobile species as well as surface atom displacement. Above 4.8 eV/Si atom we see an increase in Urbach energy and presumably also defect density, which is related to bulk atom displacement in subsurface layers at higher ion energies. We report unique experimental evidence which indicates that the band gap is *not* correlated to the total hydrogen concentration, c_H, as usually reported in literature, but instead to the presence of nanovoids in the film, as determined from the c_{HSM} mode.

Intrinsic a-Si:H deposited with PSB under the same conditions as the films from chapter 4 have also been implemented in p-i-n solar cells. These cells are discussed in chapter 5 and a reproducible record initial energy conversion efficiencies of 7.4% was obtained for cells grown by ETP-CVD at such high growth rates and low substrate temperatures. This efficiency was obtained for cells grown around deposited energies of around 1 eV/Si atom. The open-circuit voltage has a maximum of 0.82 V around 1 eV/Si atom and decreases at higher deposited energies per Si atom, which is attributed to the lowe band gap at higher deposited energy. The short-circuit current density reaches a maximum around 4.8 eV/Si atom and decreases at higher deposited energies, which is attributed to a reduced hole collection determined from external quantum efficiency measurements. The fill factor decreases above 1 eV/Si atom which we attribute to a lower mobility-lifetime product due to stronger charge carrier recombination. This indicates defect formation at deposited energies above 1.7 eV/Si atom, significantly below the reported increase in Urbach energy around

4.8 eV/Si atom reported in chapter 4.

Chapter 6 discusses the development of the a-Si:H surface roughness as function of several parameters like substrate temperature, RF substrate biasing and hydrogen dilution at growth rates of 0.1 nm/s. Important for this analysis was the spectroscopic ellipsometry technique, which allows to monitor the surface roughness development in-situ during film deposition. Distinct phases of film growth can be distinguished, such as film nucleation, nuclei coalescence, strong roughnening phase and the steady growth phase. In the first section, from depositions with and without RF substrate biasing at different substrate temperatures the presence of a hydrogen-rich layer was suggested, which is removed/densified upon externally induced ion bombardment. Following a discussion of two roughening phases in the roughness development we suggest that alternative, nonlocal growth mechanisms could play an important role in a-Si:H film growth.

In the second section of chapter 6, the surface roughness development was investigated as function of hydrogen dilution. We observe a discrepancy in the surface roughness development between spectroscopic ellipsometry and AFM measurements. We interpret this as another indication of the presence of a hydrogen rich/low density overlayer. At higher hydrogen dilutions, we obtain a thicker overlayer dominated by lower hydrides. RTSE misinterprets this overlayer as additional surface roughness and consequently overestimates the surface roughness for higher dilutions. From additional PSB experiments at two different dilutions we conclude that the hydrogen rich/low density layer is densified by the induced ion bombardment and/or excess hydrogen is removed.

Bibliography

[1] "International Energy Outlook 2010" (US Energy Information Administration, www.eia.doe.gov, 2010).

[2] D. J. C. MacKay, "Sustainable Energy - without the hot air" (www.withouthotair.com, 2009).

[3] "BP Statistical Review of World Energy" (BP, bp.com/statisticalreview, 2010).

[4] N. Kautto and A. Jaeger-Waldau, "Renewable Energy Snapshot 2009" (European Commission, Joint Research Centre, Institute for Energy, 2009).

[5] "An Energy policy for Europe" (European Commission, Brussels, 2007).

[6] S. Solomon, D. Qin, M. Manning, Z. Chen, M. Marquis, K. Averyt, M. Tignor, and H. Miller (eds.), 'IPCC 2007: Summary for Policymakers" (Cambridge University Press, Cambridge, UK, 2007).

[7] S. Shafiee and E. Topal, Energy Policy **37**(1), 181–189 (2009).

[8] E. Tzima, A. Georgakaki, and S. D. Peteves, "Future Fossil Fuel Electricity Generation in Europe: Options and Consequences" (European Commision, Joint Research Center, Institute for Energy, 2009).

[9] "A European Strategy for Sustainable, Competitive and Secure Energy (European Commission, 2006).

[10] A. Jaeger-Waldau, "PV Status Report 2009" (European Commision, Joint Research Center, Institute for Energy, 2009).

[11] A. Luque and S. S. Hegedus (eds.), "Handbook of Photovoltaic Science and Engineering" (Wiley, Chichester, 2003).

[12] R. Bhandari and I. Stadler, Solar Energy **83**(9), 1634 (2009).

[13] L. M. Ayompe, A. Duffy, S. J. McCormack, and M. Conlon, Energy Policy **38**(7), 3731 (2010).

[14] L. L. Kazmerski, Journal of Electron Spectroscopy and Related Phenomena **150**(2-3), 105–135 (2006).

[15] W. Spear and P. LeComber, Solid State Comm. **17**, 1193 (1975).

[16] D. Staebler and C. R. Wronski, Applied Physics Letters **31**, 292 (1977).

[17] K. Winer, Physical Review B **41**, 7952 (1990).

[18] R. A. Street, Physical Review B **44**(19), 10610–10616 (1991).

[19] R. A. Street, Physical Review B **43**(3), 2454–2457 (1991).

[20] A. Gallagher, Materials Research Society Symposium Proceecings **70**, 3 (1986).

[21] A. Matsuda and K. Tanaka, Journal of Applied Physics **60**(7), 2351–2356 (1986).

[22] A. Matsuda, K. Nomoto, Y. Takeuchi, A. Suzuki, A. Yuuki, and J. Perrin, Surface Science **227**(1-2), 50–56 (1990).

[23] J. Perrin, Y. Takeda, N. Hirano, Y. Takeuchi, and A. Matsuda, Surface Science **210**(1-2), 114–128 (1989).

[24] I. M. P. Aarts, A. C. R. Pipino, M. de Sanden, and W. M. M. Kessels, Applied Physics Letters **90**(16), 3 (2007).

[25] S. Yamasaki, Materials Research Society Symposium Proceecings **609**, A1.1.1 (2000).

[26] J. Robertson, Journal of Applied Physics **87**(5), 2608–2617 (2000).

[27] A. von Keudell, J. R. Abelson, and Az, Physical Review B **59**(8), 5791–5798 (1999).

[28] A. H. M. Smets, W. M. M. Kessels, and M. C. M. van de Sanden, Applied Physics Letters **82**(6), 865–867 (2003).

[29] M. Ceriotti and M. Bernasconi, Physical Review B **76**(24) (2007).

[30] T. S. Cale and G. B. Raupp, Journal of Vacuum Science & Technology B **8**(6), 1242–1248 (1990).

[31] L. Y. Cheng, J. P. McVittie, and K. C. Saraswat, Applied Physics Letters **58**(19), 2147–2149 (1991).

[32] V. K. Singh and E. S. G. Shaqfeh, Journal of Vacuum Science & Technology A **11**(3), 557–568 (1993).

[33] W. M. M. Kessels, A. H. M. Smets, and M. C. M. van de Sanden, Journal of Non-Crystalline Solids **338-40**(Jun), 27–31 (2004).

[34] Z. Q. Ma, Y. F. Zheng, and B. X. Liu, physica status solidi (a) **169**(2), 239–248 (1998).

[35] K. Wittmaack, Physical Review B **68**(23), 11 (2003).

[36] W. M. M. Kessels, R. J. Severens, A. H. M. Smets, B. A. Korevaar, G. J. Adriaenssens, D. C. Schram, and M. C. M. van de Sanden, Journal of Applied Physics **89**(4), 2404–2413 (2001).

[37] D. E. Carlson and C. R. Wronski, Applied Physics Letters **28**(11), 671–673 (1976).

[38] W. M. M. Kessels, C. M. Leewis, A. Leroux, M. C. M. van de Sanden, and D. C. Schram, Journal of Vacuum Science & Technology A **17**(4), 1531–1535 (1999).

[39] M. A. Lieberman and A. J. Lichtenberg, "Principles of Plasma Discharges and Materials Processing" (Wiley, New York, 1994).

[40] G. Kroesen, D. Schram, and M. van de Sande, Plasma Chemistry & Plasma Processing **10**, 49 (1990).

[41] J. W. A. M. Gielen, W. M. M. Kessels, and M. C. M. v. d. Sanden, Journal of Applied Physics **82**, 2643 (1997).

[42] W. M. M. Kessels, F. J. H. van Assche, J. Hong, D. C. Schram, and M. C. M. van de Sanden, Journal of Vacuum Science & Technology A **22**(1), 96–106 (2004).

[43] F. J. H. van Assche, W. M. M. Kessels, R. Vangheluwe, W. S. Mischke, M. Evers, and M. C. M. van de Sanden, Thin Solid Films **484**(1-2), 46–53 (2005).

[44] J. J. Beulens, A. Buuron, and D. C. Schram, Surface & Coatings Technology **47**, 401 (1991).

[45] E. A. G. Hamers, Acta Physica Slovaca **50**(5), 533–544 (2000).

[46] M. C. M. van de Sanden, R. J. Severens, W. M. M. Kessels, R. F. G. Meulenbroeks, and D. C. Schram, Journal of Applied Physics **84**(5), 2426–2435 (1998).

[47] W. M. M. Kessels, M. G. H. Boogaarts, J. P. M. Hoefnagels, M. C. M. van de Sanden, and D. C. Schram, Journal of Vacuum Science & Technology A **19**, 1027 (2001).

[48] I. T. Martin, M. A. Wank, M. A. Blauw, R. A. C. M. M. Van Swaaij, W. M. M. Kessels, and M. C. M. Van de Sanden, Plasma Sources Science & Technology **19**, 015012 (2010).

[49] D. Gahan, B. Dolinaj, and M. B. Hopkins, Review of Scientific Instruments **79**(3), 9 (2008).

[50] E. Kawamura, V. Vahedi, M. A. Lieberman, and C. K. Birdsall, Plasma Sources Science & Technology **8**(3), R45–R64 (1999).

[51] C. Wild and P. Koidl, Applied Physics Letters **54**(6), 505–507 (1989).

[52] A. H. M. Smets, W. M. M. Kessels, and M. C. M. van de Sanden, Journal of Applied Physics **102**, 073523 (2007).

[53] A. M. H. N. Petit, Expanding Thermal Plasma Deposition of Hydrogenated Amorphous Silicon for Solar Cells, PhD thesis, Delft University of Technology, 2006.

[54] S. B. Wang and A. E. Wendt, Journal of Applied Physics **88**(2), 643–646 (2000).

[55] H. Fujiwara, "Spectroscopic Ellipsometry - Principles and Applications" (John Wiley & Sons Ltd., Chichester, 2007).

[56] K. Vedam, Thin Solid Films **313**(Feb), 1–9 (1998).

[57] P. Drude, Annals of Physics **34**, 489 (1888).

[58] D. E. Aspnes and A. A. Studna, Applied Optics **14**, 220 (1975).

[59] R. H. Muller and J. C. Farmer, Review of Scientific Instruments **55**, 371 (1984).

[60] Y. T. Kim, R. W. Collins, and K. Vedam, Surface Science **233**(3), 341–350 (1990).

[61] R. W. Collins, J. Koh, H. Fujiwara, P. I. Rovira, A. S. Ferlauto, J. A. Zapien, C. R. Wronski, and R. Messier, Recent progress in thin film growth analysis by multichannel spectroscopic ellipsometry, in: Symposium A on Photo-Excited Processes, Diagnostics and Applications of the 1999 E-MRS Spring Conference, (Elsevier Science Bv, Strasbourg, France, Jun 01-04 1999), pp. 217–228, 30 297BA.

[62] D. Bruggeman, Annals of Physics **24**, 636 (1935).

[63] P. J. van den Oever, M. C. M. van de Sanden, and W. M. M. Kessels, Journal of Applied Physics **101**(12), 10 (2007).

[64] H. Arwin and D. E. Aspnes, Thin Solid Films **113**, 101 (1984).

[65] G. E. Jellison and F. A. Modine, Applied Physics Letters **69**(3), 371–373 (1996).

[66] J. Koh, Y. W. Lu, C. R. Wronski, Y. L. Kuang, R. W. Collins, T. T. Tsong, and Y. E. Strausser, Applied Physics Letters **69**(9), 1297–1299 (1996).

[67] I. An, H. V. Nguyen, N. V. Nguyen, and R. W. Collins, Physical Review Letters **65**(18), 2274–2277 (1990).

[68] Y. M. Li, I. An, H. V. Nguyen, C. R. Wronski, and R. W. Collins, Physical Review Letters **68**(18), 2814–2817 (1992).

[69] R. W. Collins, A. S. Ferlauto, G. M. Ferreira, C. Chen, J. Koh, R. J. Koval, Y. Lee, J. M. Pearce, and C. R. Wronski, Solar Energy Materials and Solar Cells **78**(1-4), 143–180 (2003).

[70] D. Levi, B. P. Nelson, and R. Reedy, Thin Solid Films **430**(1-2), 20–23 (2003).

[71] D. H. Levi, B. P. Nelson, J. D. Perkins, and H. R. Moutinho, Journal of Vacuum Science & Technology A **21**(4), 1545–1549 (2003).

[72] W. M. M. Kessels, J. P. M. Hoefnagels, E. Langereis, and M. C. M. van de Sanden, Thin Solid Films **501**(1-2), 88–91 (2006).

[73] A. H. M. Smets, M. C. M. de Sanden, and D. C. Schram, Thin Solid Films **344**(Apr), 281–284 (1999).

[74] A. H. M. Smets, D. C. Schram, and M. C. M. van de Sanden, Journal of Applied Physics **88**(11), 6388–6394 (2000).

[75] R. W. Collins, J. Koh, A. S. Ferlauto, P. I. Rovira, Y. H. Lee, R. J. Koval, and C. R. Wronski, Thin Solid Films **364**(1-2), 129–137 (2000).

[76] A. H. M. Smets, W. M. M. Kessels, and M. C. M. van de Sanden, Applied Physics Letters **82**(10), 1547–1549 (2003).

[77] W. M. M. Kessels, M. C. M. v. d. Sanden, R. J. Severens, L. J. v. Ijzendoorn, and D. C. Schram, in: Mater. Res. Soc. Symp. Proc., (1998), p. 529.

[78] Z. Remes, M. Vanecek, P. Torres, U. Kroll, A. H. Mahan, and R. S. Crandall, Journal of Non-Crystalline Solids **227**, 876–879 (1998).

[79] J. Tauc, R. Grigorovici, and A. Vancu, physica status solidi (b) **15**(2), 627–637 (1966).

[80] M. Stutzmann, Philosophical Magazine B - Physics of Condensed Matter **60**(4), 531–546 (1989).

[81] R. E. I. Schropp and M. Zeman, "Amorphous and Microcrystalline Silicon Solar Cells - Modeling, Materials and Device Technology" (Kluwer Academic Publishers, 1998).

[82] S. S. Hegedus and W. N. Shafarman, Progress in Photovoltaics **12**(2-3), 155–176 (2004).

[83] W. M. M. Kessels, M. C. M. van de Sanden, and D. C. Schram, Applied Physics Letters **72**, 2397 (1998).

[84] S. Acco, D. L. Williamson, P. A. Stolk, F. W. Saris, M. J. vandenBoogaard, W. C. Sinke, W. F. vanderWeg, and S. Roorda, Physical Review B **53**(8), 4415–4427 (1996).

[85] S. Acco, D. L. Williamson, W. van Sark, W. C. Sinke, and W. F. van der Weg, Physical Review B **58**(19), 12853–12864 (1998).

[86] W. Beyer and U. Zastrow, Journal of Non-Crystalline Solids **230**, 880–884 (1998).

[87] H. R. Kaufman and J. M. E. Harper, Journal of Vacuum Science & Technology A **22**(1), 221–224 (2004).

[88] M. A. Ring, V. L. Dalal, and K. K. Muthukrishnan, Journal of Non-Crystalline Solids **338-40**(Jun), 61–64 (2004).

[89] B. Drevillon, J. Perrin, J. M. Siefert, J. Huc, A. Lloret, G. Derosny, and J. P. M. Schmitt, Applied Physics Letters **42**(9), 801–803 (1983).

[90] E. A. G. Hamers, W. van Sark, J. Bezemer, H. Meiling, and W. F. van der Weg, Journal of Non-Crystalline Solids **226**(3), 205–216 (1998).

[91] T. V. Herak, T. T. Chau, S. R. Mejia, P. K. Shufflebotham, J. J. Schellenberg, H. C. Card, K. C. Kao, and R. D. McLeod, Journal of Non-Crystalline Solids **97-98**(Part 1), 277–280 (1987).

[92] M. H. Brodsky, Thin Solid Films **40**(JAN), L23–L25 (1977).

[93] W. M. M. Kessels, M. C. M. van de Sanden, R. J. Severens, and D. C. Schram, Journal of Applied Physics **87**, 3313 (2000).

[94] Y. Kuo, Journal of the Electrochemical Society **142**(7), 2486–2507 (1995).

[95] W. M. M. Kessels, A. H. M. Smets, D. C. Marra, E. S. Aydil, D. C. Schram, and M. C. M. van de Sanden, Thin Solid Films **383**(1-2), 154–160 (2001).

[96] B. Drevillon, J. Huc, and N. Boussarssar, Journal of Non-Crystalline Solids **59-6**(DEC), 735–738 (1983).

[97] H. Rinnert, M. Vergnat, G. Marchal, and A. Burneau, Nuclear Instruments and Methods in Physics Research Section B **147**(1-4), 79–83 (1999).

[98] P. Roca i Cabarrocas, P. Morin, V. Chu, J. P. Conde, J. Z. Liu, H. R. Park, and S. Wagner, Journal of Applied Physics **69**(5), 2942–2950 (1991).

[99] A. S. Abramov, A. I. Kosarev, P. Roca i Cabarrocas, M. V. Shutov, and A. J. Vinogradov, Thin Solid Films **383**(1-2), 178–180 (2001).

[100] S. Zhang and D. E. Brodie, Journal of Physics: Condensed Matter **3**(34), 6597 (1991).

[101] E. V. Barnat and T. M. Lu, Journal of Applied Physics **92**, 2984 (2002).

[102] P. Kudlacek, R. F. Rumphorst, and M. C. M. van de Sanden, Journal of Applied Physics **106**(7), 8 (2009).

[103] W. D. Davis and T. A. Vanderslice, Physical Review **131**(1), 219–& (1963).

[104] G. J. H. Brussaard, M. van der Steen, M. Carrere, M. C. M. van de Sanden, and D. C. Schram, Surface & Coatings Technology **98**(1-3), 1416–1419 (1998).

[105] B. Chapman, "Glow Discharge Processes: Sputtering and Plasma Etching" (Wiley-Interscience, New York, 1980).

[106] J. P. M. Hoefnagels, Y. Barrell, W. M. M. Kessels, and M. C. M. van de Sanden, Journal of Applied Physics **96**, 4094 (2004).

[107] E. Stamate and H. Sugai, Physical Review E **72**, 036407 (2005).

[108] S. M. Rossnagel and J. J. Cuomo, Vacuum **38**(2), 73–81 (1988).

[109] A. R. Gonzalez-Elipe, F. Yubero, and J. M. Sanz, "Low Energy Ion Assisted Film Growth" (Imperial College Press, London, 2003).

[110] M. A. Wank, R. A. C. M. M. van Swaaij, and M. C. M. van de Sanden, Applied Physics Letters **95**(2), 021503 (2009).

[111] M. A. Wank, R. A. C. M. M. van Swaaij, and M. C. M. van de Sanden, Amorphous and Polycrystalline Thin-Film Silicon Science and Technology 2007 **989**, 523–528 594 (2007).

[112] Z. Q. Ma, International Journal of Modern Physics B **21**(25), 4299–4322 (2007).

[113] D. Marton, "Low Energy Ion-Surface Interactions" (Wiley, New York, 1994).

[114] G. D. Cody, B. Abeles, C. R. Wronski, R. B. Stephens, and B. Brooks, Solar Cells 2 p. 227 (1980).

[115] K. Fukutani, M. Kanbe, W. Futako, B. Kaplan, T. Kamiya, C. M. Fortmann, and I. Shimizu, 17th International Conference on Amorphous and Microcrystalline Semiconductors - Science and Technology (ICAMS 17)(Aug 25-29), 63–67 (1997).

[116] C. M. Fortmann, Physical Review Letters **81**(17), 3683 (1998).

[117] A. J. M. van Erven, R. C. M. Bosch, A. W. Weeber, and M. D. Bijker, in: 19th European Photovoltaic Solar Energy Conference and Exhibition, (2004), p. 2CV.2.20.

[118] M. A. Wank, P. Kudlacek, R. A. C. M. M. Van Swaaij, M. C. M. Van de Sanden, and M. Zeman, Journal of Applied Physics **108**, 103304 (2010).

[119] M. A. Green, "Solar Cells - Operating Principles, Technology and System Application" (Univ. of New South Wales, Kensington, 1992).

[120] B. W. Faughnan and R. S. Crandall, Applied Physics Letters **44**(5), 537–539 (1984).

[121] R. W. Collins and B. Y. Yang, Journal of Vacuum Science & Technology B **7**(5), 1155–1164 (1989).

[122] A. L. Barabasi and H. E. Stanley, "Fractal Concepts in Surface Growth" (Cambridge University Press, Cambridge, U.K., 1995).

[123] B. A. Sperling, J. R. Abelson, and Ss, Journal of Applied Physics **101**(2), 7 (2007).

[124] G. T. Dalakos, J. L. Plawsky, and P. D. Persans, Materials Research Society Symposium Proceecings **762**, A5.14 (2003).

[125] G. T. Dalakos, J. L. Plawsky, and P. D. Persans, Applied Physics Letters **85**(16), 3462–3464 (2004).

[126] G. T. Dalakos, J. P. Plawsky, and P. D. Persans, Physical Review B **72**, 205305 (2005).

[127] D. J. Eaglesham, Journal of Applied Physics **77**, 3597 (1995).

[128] M. F. Gyure, J. J. Zinck, C. Ratsch, and D. D. Vvedensky, Physical Review Letters **81**(22), 4931–4934 (1998).

[129] T. Karabacak, Y. P. Zhao, G. C. Wang, and T. M. Lu, Physical Review B **6408**(8), 6 (2001).

[130] M. Kondo, T. Ohe, K. Saito, T. Nishimiya, and A. Matsuda, Journal of Non-Crystalline Solids **230**, 890–895 (1998).

[131] A. Yanguas-Gil, J. Cotrino, A. Barranco, and A. R. Gonzalez-Elipe, Physical Review Letters **96**(23) (2006).

[132] A. Yanguas-Gil, J. Cotrino, A. Walkiewicz-Pietrzykowska, and A. R. Gonzalez-Elipe, Physical Review B **76**(7), 8 (2007).

[133] H. Fujiwara, Y. Toyoshima, M. Kondo, and A. Matsuda, Physical Review B **60**(19), 13598–13604 (1999).

[134] B. Drevillon and M. Toulemonde, Journal of Applied Physics **58**(1), 535–540 (1985).

[135] H. Fujiwara, J. Koh, P. I. Rovira, and R. W. Collins, Physical Review B **61**(16), 10832–10844 (2000).

[136] T. M. Lu, Y. P. Zhao, J. T. Drotar, T. Karabacak, and G. C. Wang, Materials Research Society Symposium Proceecings **749**, 3 (2003).

[137] W. M. M. Kessels, K. Nadir, and M. C. M. van de Sanden, Journal of Applied Physics **99**(7), 3 (2006).

Summary

Our modern lifestyle is currently fueled by two billion years of accumulated energy reserves. For several years now there has been a strong rise in research interest and more recently also implementation of renewable energy sources in the European Union. Driving factors for these developments are the increasing awareness of global warming in our society, the limited nature of current fossil fuel sources, the need for energy security & independence and the opportunity to develop new technologies and business opportunities.

Obtaining energy from solar radiation via solar cells based on cyrstalline silicon has seen continuous development since the demonstration of the first photovoltaic devices in the 1950's. These types of solar cells are still the dominant technology today, but other solar cell technologies are about to make the transition from research labs into significant production volumes. One of these technologies is the hydrogenated amorphous silicon (a-Si:H) thin film solar cell, which promises to be a cheap alternative to the crystalline silicon solar cell, albeit at a reduced energy conversion efficiency.

The deposition technique used to grow a-Si:H thin films in this work is the expanding thermal plasma chemical vapor deposition (ETP-CVD). Main benefit of ETP-CVD are the high growth rates of more than 1 nm/s that can be achieved, which is very beneficial for the growth of the thick intrinsic absorber layer in a solar cell. Substrate temperatures of $>300^\circ$C are required to obtain dense a-Si:H films suitable for solar cell application – temperatures that leads to degradation of previously deposited p-doped layers in a typical p-i-n solar cell. In order to reduce the temperature load during deposition, ion bombardment was employed with the goal to provide the growing film surface with kinetic energy from the bombarding ions, thereby allowing to deposit dense a-Si:H films at substrate temperatures around 200°C. The results discussed in chapter

4 and 5 show that significant progress towards this goal has been achieved, as demonstrated by solar cells with $> 7\%$ initial efficiency at a growth rate of 1 nm/s and substrate temperatures between 200 – 180°C for the intrinsic layer. To achieve this we have utilised two different types of substrate biasing, sinusoidal RF biasing and pulse-shaped biasing, with focus on the latter. Both biasing techniques result in ion bombardment of the film surface during deposition.

Both biasing techniques enable the deposition of solar-grade intrinsic a-Si:H at substrate temperatures below the 350°C required for unbiased deposition. In chapter 3 we demonstrate how RF substrate biasing leads to the growth of vacancy-dominated material up to 50°C below the temperature required for unbiased deposition. This conclusion is based on FTIR analysis where a transition form vacancy- to void-dominated material is observed. We investigated the dependence of this transition on the reactor pressure. Ion bombardment at a DC bias voltage V_{DC} of 14 V has hardly any effect on the transition, yet an increase in void fraction was observed for all temperatures and increasing pressures. Ion bombardment at $V_{DC} = 20$ V for the high pressure series resulted in an increase of the transition from 9% total hydrogen concentration unbiased to 13% total hydrogen concentration biased. This is attributed to a reduced incorporation of ionic clusters and polymers into the film.

The second type of substrate biasing utilized in this work is the pulse-shaped biasing, PSB. As shown in chapter 4, with PSB we are able to obtain accurate control over the ion energy distribution in a range of 0 - 200 eV without the formation of a strong secondary plasma typically present for RF substrate biasing. Control over the ion energy was confirmed by retarding field energy analyzer measurements for conductive substrates, and non-conductive substrates covered with a conductive surface layer which is connected to the sample holder.

For intrinsic a-Si:H deposited with PSB at a growth rate of 1 nm/s and substrate temperatures in the range of 180 - 200°C we can distinguish roughly between two regions: region I < 4.8 eV of deposited energy per Si atom (eV/Si atom) and region II > 4.8 eV/Si atom. In region I we observe an increase in material density due to a decrease in nanovoid concentration as deduced from FTIR analysis. At the transition between region I and II around 4.8 eV/Si atom the densest material with low nanovoid concentration is obtained. The increase in material density and the reduction in surface roughness in region I are attributed to an increase in surface mobility of mobile species as well as surface atom displacement. Above 4.8 eV/Si atom we see an increase in Urbach energy which is related to bulk atom displacement in subsurface layers at higher ion energies. We report unique experimental evidence which indicates that the band gap is *not* correlated to the total hydrogen concentration, c_H, as usually reported in literature, but instead to the presence of nanovoids in the film, as

determined from the c_{HSM} mode.

Intrinsic a-Si:H deposited with PSB under the same conditions as the films from chapter 4 have also been implemented in p-i-n solar cells. These cells are discussed in chapter 5 and a reproducible record initial energy conversion efficiencies of 7.4% was obtained for cells grown by ETP-CVD at such high growth rates of 1 nm/s and low substrate temperatures of 200°C. This efficiency was obtained for cells grown around deposited energies of around 1 eV/Si atom. The open-circuit voltage has a maximum of 0.82 V around 1 eV/Si atom and decreases at higher deposited energies per Si atom, which is attributed to the low band gap at higher deposited energy. The short-circuit current density reaches a maximum around 4.8 eV/Si atom and decreases at higher deposited energies, which is attributed to a reduced hole collection determined from external quantum efficiency measurements. The fill factor decreases above 1 eV/Si atom which we attribute to a lower mobility-lifetime product due to an increase in charge carrier recombination. This indicates defect formation at deposited energies above 1.7 eV/Si atom, significantly below the reported increase in Urbach energy around 4.8 eV/Si atom reported in chapter 4.

Chapter 6 discusses the development of the a-Si:H surface roughness as function of several parameters like substrate temperature, RF substrate biasing and hydrogen dilution at growth rates of 0.1 nm/s. Important for this analysis was the spectroscopic ellipsometry technique, which allows to monitor the surface roughness development in-situ during film deposition. In the first section, from depositions with and without RF substrate biasing at different substrate temperatures the presence of a hydrogen-rich layer was suggested, which is removed/densified upon externally induced ion bombardment. In the second section of chapter 6, the surface roughness development was investigated as function of hydrogen dilution. We observe a discrepancy in the surface roughness development between spectroscopic ellipsometry and AFM measurements. We interpret this as another indication of the presence of a hydrogen rich/low density overlayer. At higher hydrogen dilutions, we obtain a thicker overlayer dominated by lower hydrides. From additional PSB experiments at two different dilutions we conclude that the hydrogen rich/low density layer is densified by the induced ion bombardment and/or excess hydrogen is removed.

Samenvatting

Onze moderne levensstijl wordt gevoed door brandstoffen die door de natuur zijn opgespaard over een periode van 2 miljard jaar. In de Europese Unie is er de laatste jaren een toegenomen belangstelling voor het onderzoek aan en sinds kort ook de toepassing van duurzame energiebronnen. Stimulansen voor deze trend zijn het toegenomen besef over klimaatverandering, de feitelijke eindigheid van de fossiele energiereserves, de behoefte voor een veilige en onafhankelijke energiebron en de mogelijkheid voor het ontwikkelen van nieuwe technologie en de bijbehorende marktkansen

De eerste fotovoltaïsche cellen gebaseerd op kristallijn silicium waarmee zonlicht direct in elektrische energie omgezet kon worden stammen uit de jaren 50. Sindsdien is er een voortdurende ontwikkeling geweest van de technologie van zonnecellen. Deze type van zonnecellen hebben op dit moment nog het grootste marktaandeel. Echter andere zonneceltechnologieën staan op het punt om vanuit de onderzoeksfase de productiefase te bereiken. Een van deze nieuwe technologieën zijn zonnecellen gebaseerd op dunne lagen van gehydrogeneerd amorf silicium (a-Si:H). Zulke zonnecellen beloven een goedkoop alternatief te zijn voor kristallijn silicium zonnecellen, echter wel met een lager omzettingsrendement.

Een depositietechniek waarmee dunne lagen van a-Si:H gegroeid kunnen worden is expanderend thermisch plasma chemische damp depositie (ETP-CVD). Het belangrijkste voordeel van ETP-CVD is dat hoge aangroeisnelheden van meer dan 1 nm/s behaald kunnen worden, wat een groot tijdsvoordeel oplevert bij het deponeren van de relatief dikke intrinsieke absorptielaag van de zonnecel. Voor de depositie van a-Si:H met een hoge dichtheid die geschikt is voor gebruik in een zonnecel, is een substraattemperatuur nodig die hoger ligt dan 300°C. Zulke temperaturen zullen de voorafgaand gedeponeerde p-type

gedoteerde laag van de p-i-n zonnecel aantasten. Om de temperatuurbelasting tijdens de depositie te verlagen is ionenbombardement gebruikt dat het aangroeiende filmoppervlak voorziet van kinetische energie. Dit maakt het mogelijk om a-Si:H films met een hoge dichtheid te deponeren bij een substraattemperatuur rond de 200°C. De in hoofdstuk 4 en 5 besproken resultaten laten zien dat een belangrijke vooruitgang is geboekt. Dit wordt bevestigd door zonnecellen met initieel rendement van meer dan 7% bij een groeisnelheid van 1 nm/s en substraattemperaturen tussen 180 en 200°C voor de intrinsieke laag. Om dit te bereiken hebben we twee verschillende signaalvormen van de aangelegde biasspanning op het substraat gebruikt: een conventioneel sinusvormige biasspaning en een pulsvormige biasspanning, met de nadruk op de laatste. Beide signaalvormen resulteren in een ionenbombardement van het filmoppervlak tijdens depositie.

Beide signaalvormen maken de hoge snelheidsdepositie van intrinsiek a-Si:H met een kwaliteit die nodig is voor zonnecellen mogelijk bij een substraattemperatuur beneden de 350°C, een temperatur die nodig is voor depositie zonder biasspanning. In hoofdstuk 3 hebben we laten zien hoe een de toepassing van een radio-frequente (RF) biasspanning op het substraat leidt tot de aangroei van *vacancy*-gedomineerd materiaal bij een temperatuur die tot 50°C lager is dan de temperatuur benodigd voor een depositie zonder biasspanning. Deze conclusie is gebaseerd op de analyse van infraroodspectra die een overgang laat zien van materiaal dat gedomineerd wordt door *vacancies* naar dat gedomineerd door *voids*. We hebben onderzocht hoe deze overgang afhangt van de druk in de reactor tijdens de depositie. Ionenbombardement bij een gelijkspanningsbias V_{dc} van 14 V heeft nauwelijks effect op de overgang, terwijl een we een toename van de void-fractie hebben waargenomen voor alle temperaturen en toenemende drukken. Ionenbombardement bij V_{dc} = 20 V resulteerde voor de hoge-drukserie in een verschrijving van de overgang bei een waterstof concentratie van 9% zonder biasspanning naar 13% waterstof concentratie met biasspanning. Dit schrijven we toe aan een verminderde inbouw van ionenclusters en polymeren in de film.

De tweede signaalvorm die in dit werk gebruikt wordt voor de aangelegde spanning op het substraat is de zogenaamde *pulse-shaped biasing*: PSB. Zoals beschreven is in hoofdstuk 4, zijn wij in staat om met PSB nauwkeurige controle over de ionenenergieverdeling te verkrijgen tussen 0 en 200 eV zonder daarbij een sterk secundair plasma te vormen dat typisch aanwezig is wanneer een RF spannig op het substraat wordt aangelegd. De controle over de ionenenergie is bevestigd door metingen met een zogenaamde *retarding field analyser* op geleidende substraten en niet-geleidende substraten bedekt met een geleidende laag die verbonden is met de substraathouder.

Voor intrinsiek a-Si:H gedeponeerd met PSB bij een aangroeisnelheid van

1 nm/s en een substraattemperatuur tussen 180 en 200°C kunnen we grofweg twee energiebereiken onderscheiden: bereik I $<$ 4.8 eV gedeponeerde energie per Si atoom (eV/Si atoom) en bereik II $>$ 4.8 eV/Si atoom. In bereik I zien we een toename in materiaaldichtheid ten gevolge van een afname van de concentratie aan gaten in het materiaal met nanometer afmetingen, zoals afgeleid uit de analyse van infraroodspectra. Bij de overgang tussen bereik I en II rond 4.8 eV/Si atoom wordt het materiaal met de hoogste materiaaldichtheid en de laagste concentratie aan gaten verkregen. De toename in materiaaldichtheid en de afname van de oppervlakteruwheid in energiebereik I worden toegeschreven aan een toename van zowel de mobiliteit van deeltjes op het aangroei-oppervlak als aan de verplaatsing van atomen aan het oppervlak. Boven 4.8 eV/Si atoom zien we een toename in Urbachenergie die gerelateerd is aan de verplaatsing van atomen in de bulk van lagen onder het oppervlak bij hogere ionenenergieën. We demonstreren uniek experimenteel bewijs dat erop wijst dat de bandafstand *niet* gecorreleerd is aan de totale waterstofconcentratie c_H, zoals normaal gesproken gerapporteerd wordt in de literatuur, maar in plaats daarvan aan de aanwezigheid van nanogaten in de film, zoals bepaald is uit de c_{HSM} mode.

Intrinsiek a-Si:H gedeponeerd met dezelfde PSB depositiecondities als voor de films uit hoofdstuk 4 is ook geïmplementeerd in p-i-n zonnecellen. Deze cellen worden besproken in hoofdstuk 5 en een reproduceerbaar initieel recordconversierendement van 7.4% is bereikt voor cellen gegroeid met behulp van ETP-CVD bij zulke hoge groeisnelheden van 1 nm/s en lage substraattemperaturen van 200°C. Dit rendement is bereikt voor cellen die gegroeid zijn bij depositieenergieën rond 1 eV/Si atoom. De open-klem spanning heeft een maximum van 0.82 V rond de 1 eV/Si atoom. Deze neemt af bij een hogere depositieenergie per Si atoom, hetgeen verklaard kan worden door de lagere bandafstand die ontstaat bij een hogere depositie energie. De kortsluitstroomdichtheid haalt een maximum rond de 4.8 eV/Si atoom. Deze neemt eveneens af bij een hogere depositie energie, hetgeen verklaard kan worden door een verminderde collectie van gaten, zoals blijkt uit metingen van het externe kwantumrendement. De vulfactor neemt af boven de 1 eV/Si atoom, wat toegeschreven wordt aan een lager mobiliteits-levensduur product vanwege de toename in recombinatie van ladingsdragers. Dit wijst op de formatie van defecten bij een depositie energie boven de 1.7 eV/Si atoom. Deze waarde is significant lager dan de gerapporteerde toename van de Urbach energie van ruwweg 4.8 eV/Si atoom, zoals beschreven is in hoofdstuk 4.

Hoofdstuk 6 behandelt de ontwikkeling van de oppervlakteruwheid van a-Si:H als functie van verscheidene parameters, zoals de substraattemperatuur, de aangelegde RF spanning op het substraat en de waterstofverdunning in het plasma bij aangroeisnelheden van 0.1 nm/s. Voor deze analyse was de spec-

troscopische ellipsometrie techniek van belang, omdat het met deze techniek mogeijk is om de oppervlakteruwheid in situ te volgen tijdens de depositie van de dunne laag. In het eerste deel, dat bestaat uit deposities mét en zonder RF spanning op het substraat bij verscheidene substraattemperaturen, wordt de aanwezigheid van een waterstofrijke laag gesuggereerd, die wordt verwijderd/verdicht bij een extern bombardement van ionen. In het tweede deel van hoofdstuk 6 is de ontwikkeling van de oppervlakteruwheid onderzocht als functie van de waterstofverdunning in het plasma. Hier werd een discrepantie geobserveerd in de ontwikkeling van de oppervlakteruwheid tussen de spectroscopische ellipsometrie en AFM metingen. Dit wordt geïnterpreteerd als een extra indicatie van de aanwezigheid van een waterstofrijke bovenlaag met een lage dichtheid. Bij een hogere waterstofverdunning in het plasma wordt een dikkere bovenlaag verkregen, die wordt gedomineerd door lagere hydriden. Uit additionele PSB experimenten bij twee verschillende verdunningen concluderen wij dat de waterstofrijke laag van lage dichtheid wordt verdicht door het geïnduceerde ionenbombardement, en/of dat het excessieve waterstof wordt verwijderd.

Publications

M.A. Wank, R.A.C.M.M. van Swaaij, M.C.M. van de Sanden, M. Zeman, "Hydrogenated Amorphous Silicon p-i-n Solar Cells Deposited Under Well Controlled Ion Bombadment Using Pulse-Shaped Substrate Biasing", *Progress in Photovoltaics*, under review

M.A. Wank, P. Kudlacek, R.A.C.M.M. van Swaaij, M.C.M. van de Sanden, M. Zeman, "Hydrogenated amorphous silicon deposited under accurately controlled ion bombardment using pulse-shaped substrate biasing", *Journal of Applied Physics*, vol. **108**, p. 103304 (2010)

M.A. Wank, A. Illiberi, F. D. Tichelaar, R.A.C.M.M. van Swaaij, M.C.M. van de Sanden, M. Zeman "Influence of hydrogen dilution on surface roughness development of a-Si:H thin films grown by remote plasma deposition", *physica status solidi (c)*, vol. **7**, p. 571 (2010)

I.T. Martin, M.A. Wank, M.A. Blauw, R.A.C.M.M. van Swaaij, W.M.M. Kessels, M.C.M. van de Sanden, "The effect of low frequency pulse-shaped substrate bias on the remote plasma deposition of a-Si :H thin films", *Plasma Sources Science and Technology*, vol. **19**, p. 015012 (2010)

M.A. Wank, R.A.C.M.M. van Swaaij, M.C.M. van de Sanden, "On the surface roughness development of hydrogenated amorphous silicon deposited at low growth rates", *Applied Physics Letters*, vol. **95**, p. 021503 (2009)

M.A. Wank, R.A.C.M.M. van Swaaij, M.C.M. van de Sanden, "Ion Assisted ETP-CVD a-Si:H at Well Defined Ion Energies", *Mater. Res. Soc. Symp. Proc.*, vol.

1153 , A17-06 (2009)

M.A. Wank, R.A.C.M.M. van Swaaij, M.C.M. van de Sanden, "Surface roughness analysis of ETP-CVD a-Si:H thin films", *Proceedings of the 11th STW Annual Workshop on Semiconductor Advances for Future Electronics and Sensors*, Veldhoven, the Netherlands, pp. 516-519 (2008)

M.A. Wank, R.A.C.M.M. van Swaaij, M.C.M. van de Sanden, "Manipulating the Hydrogen-Bonding Configuration in ETP-CVD a-Si:H", *Mater. Res. Soc. Symp. Proc.*, vol. **989**, A22-04 (2007)

M.A. Wank, R.A.C.M.M. van Swaaij, M.C.M. van de Sanden, "In-situ study by spectroscopic ellipsometry of ETP-CVD a-Si:H", *Proceedings of the 10th STW Annual Workshop on Semiconductor Advances for Future Electronics and Sensors*, Veldhoven, the Netherlands, pp. 558-563 (2007)

M.A. Wank, I.T. Martin, M.A. Blauw, R.A.C.M.M. van Swaaij, M.C.M. van de Sanden, "Control of the ion-distribution and measurement of ion currents with a non-sinusoidal substrate bias", *Proceedings of the 9th STW Annual Workshop on Semiconductor Advances for Future Electronics and Sensors*, Veldhoven, the Netherlands, pp. 488-493 (2006)

Acknowledgements

First and foremost I would like to thank my two promoters, Professor Miro Zeman and Professor Richard van de Sanden for giving me the opportunity to engage in a PhD project under their guidance. I thank Richard for his very constructive feedback during our regular meetings and discussions which always gave my research new impulse in interesting directions. Furthermore I am very grateful to my co-promoter and daily supervisor René van Swaaij. He gave me guidance when it was needed and abundant freedom to satisfy my curiosity. His feedback on papers was remarkably quick and essential to structure and content of my publications.

During my 4 years as PhD student I had the opportunity to cooperate with many colleagues both at TU Delft and outside of TU Delft. I am grateful to Ina Martin for our cooperation in the first year of my PhD which helped me a lot to get started with both spectroscopic ellipsometry and pulse-shaped biasing. Also Michiel Blauw was essential to set up and improve the pulse-shaped biasing setup. I want to thank Frans Tichelaar from the Faculty of Applied Sciences for taking HR-TEM images of several samples for me. The cooperation with Pavel Kudlacek was important to finish an essential part of my experimental work with the retarding field analyzer, our two days in the lab were among my most productive and important days in the last 4 years. I also appreciated the descusions I had with Andrea Illiberi on some of my spectroscopic ellipsometry results.

Kehinde Adejumo supported me during a critical phase in my PhD and did an excellent job in tirelessly analyzing countless numbers of samples that I delivered to her desk. The influence of our technicians on the productivity of the group can not be underestimated. I owe Stefaan Heirman, Jan Chris Staalenburg, Martijn Tijssen and Kasper Zwetsloot much appreciation for the

efforts in keeping deposition and measurement equipment running, for helping with training and changes to existing equipment as well as installation of new setups, and for providing me with countless numbers of p-doped layers on ASAHI substrates that I turned into solar cells. I also want to thank the whole DIMES support stuff for keeping the cleanroom up and running and for occasional equipment training. Special thanks go to Johan van der Cingel for his efforts he put into the AFM setup and Jan Groeneweg for the occasional tennis match in my first year. I appreciated the help received from several secretaries when dealing with administrative tasks, thanks goes to Laura Bruns, Lucy Verkade, Iris de Jel, Suzy Sirks-Bong, Marysia Lagendijk-Korzeniewski and Marian Roozenburg-de Bree

During my PhD I had to change office more than I wanted to, but it gave me the opportunity to share the workspace with several great colleagues. I appreciated the friendly, communicative and yet focused atmosphere I shared in DI 01.120 with Yann Civale, Luigi Laspina and Vladimir Jovanovic, in DI 01.170 with Olindo Isabella, Joke Westra and Bas Vet, and in LB 03.390 with Mark Workum, Andrea Ingenito and Mirjam Theelen. I want to thank the rest of the PVMD group for a great time in Delf: Sergiy Dobrovolskiy, Serge Solntsev, Janez Krc, Rudi Santbergen, Tristan Temple, Arno Smets, Solomon Agbo, Pavel Babal, Marinus Fischer, Klaus Jaeger, Karol Jarolimek, Jimmy Melskens (please stick to the Rhino-Banana plan!), Guangtao Yang, Dong Zhang, Rengrong Liang, Brano Grancic, Stefan Luxembourg, Andrej Campa, Raul Jimenez Zambrano, Bart Pieters and Arjen Klaver. I especially acknowledge the help of Jimmy, Marinus, Rudi and Mark with the Dutch translation of my summary.

I want to thank people I met in my time in Delft that were not involved in my work, starting with the people from ECTM: Elina, Gianpaolo, Parastoo, Marko, Benjamin, Fabio, Daniel, Francesco, Victor, Vikas, Mauro, Alessandro, Nobu, Gregory, Gennaro, Gigi and Vladimir M. . I want to thank all the friends I made outside of the university for making these last years in Delft such a remarkable experience: Raymond, Tobias, Mounir, Karo, Tai & Francois, Chara, Gertjan, Nassira, Laurant, Berenice, Joelle, Didier, Kasia, Sadek, Neel, Marcel and all the people from the Aikido Centrum Delft.

I want to express my gratitude to my Family for supporting me when I embarked on this adventure to Delft in November 2005. I deeply thank my parents, my grandfather, Linde, my sister, Christoph and Dominik for their support. The final words of this thesis are dedicated to Aysha: I think I would have finished this thesis much faster without you in my life, but I would have been a lot more miserable. Thank you for your love and support!

About the Author

Michael Alexander Wank was born in Frankfurt/Main, Germany, on July 5th 1979. He attended the Goethe Gymnasium in Bensheim where he obtained his general qualification for university entrance (Abitur) in 1999.

He studied Material Science at the Technical University Darmstadt where he obtained his pre-diploma in June 2002. From July 2003 to January 2005 he participated in the Advanced Materials program at the Chalmers University of Technology where he graduated with a Master of Science degree in January 2005. The title of his Master thesis was "Growth and Characterisation of Doped Organic Semiconductor LED Heterostructures". From March to September 2005 he worked as student trainee at Merck AG in Darmstadt, Germany, where he investigated novel emitter materials for organic LED's.

From November 2005 to February 2010 he was PhD student in the Photovoltaic Materials and Devices Group of Prof. dr. M. Zeman at the faculty of Electrical Engineering, Mathematics and Computer Science at Delft University of Technology in the Netherlands. He carried out research on the deposition of hydrogenated amorphous silicon films with the expanding thermal plasma technique. He worked in the same group from October 2010 until January 2011 as researcher, investigating the fabrication of silicon nanocrystals from amorphous silicon-based alloy materials. Since February 2011 he works as process engineer at OSRAM Opto Semiconductors GmbH in Regensburg, Germany.